Università degli Studi di Napoli Federico II

Scuola Politecnica e delle Scienze di Base
Area Didattica di Scienze Matematiche Fisiche e Naturali

**Dipartimento di Fisica "Ettore Pancini"**

Corso di Laurea Magistrale in Fisica

# Comparative analysis of coupling schemes in superconducting transmon qubits device

**Relatori**
Prof. Francesco Tafuri
Dott. Davide Massarotti
Dott. Halima Giovanna Ahmad

**Correlatore**
Prof. Carmine Antonio Perroni

**Candidato**
Carlo Cosenza
*N*94000369

Anno Accademico 2022–2023

# Contents

# Introduction

Since Feynmann's first statement on the potential of a quantum computer in 1981 [1], significant advancements have been made towards simulating physical phenomena through manageable quantum systems [2][3]. However, the journey towards large-scale quantum computing requires reconciling the dichotomy between the non-quantum macroscopic observer and the quantum microscopic information.

Superconducting circuits have emerged as a promising platform, leveraging well-established knowledge of superconducting nanofabrication processes [4]. These macroscopic systems harness the quantum properties of superconducting matter through the Josephson effect. This enables the creation of artificial macroscopic quantum systems, or qubits, to encode and process quantum information.

Over the past two decades, research has not only built isolated superconducting qubits but has also made progress towards multi-qubit architectures [5]. In this context, the dynamic control of qubit-qubit interaction is pivotal, addressing critical issues related to scalability, such as frequency crowding and parasitic coupling between adjacent qubits [6]. Within this evolving landscape, this thesis aims to explore and analyze the physics of an innovative coupling design based on tunable interaction, a crucial component for realizing large-scale quantum architectures.

This design, first proposed by the MIT researchers [7], is now attracting noticeable interest by leading companies in the field, like *Google* [8] and *Rigetti* [9]. Indeed, the tunable coupling scheme is well suited for modularity and scalability [9]. In this work, I describe a similar prototype consisting of two qubits coupled by a third qubit, serving as a mediator of the interaction. This work plays a significant role in the European project Eurostars SFQ4QPU, which involves two small- and medium-enterprises, the digital quantum computing company *Seeqc* [10] and the quantum foundry *Quantware* [11], and the University of Naples Federico II (*UniNa*) [12] as academic partner, responsible for conducting the measurements and characterization of the devices. My contribution to this project encompassed the implementation of experiments and analysis of the coupling between two qubits, aiming to push the boundaries of our understanding of quantum interaction in superconducting devices.

Specifically, in this thesis, the comparison with a standard coupling scheme based on non-tunable high-frequency superconducting bus resonators established a benchmark, crucial for validating a novel method for data analysis. In order to extract information on the coupling strengths in superconducting multi-qubit devices characterized by different coupling schemes, we propose a comparative approach between theoretical non-perturbative energy spectra simulations and experimental data, aiming to extract fundamental design parameters of the devices and to provide a physical picture of the coupling mechanisms in a complex artificial two-level system.

In Chapter 1, we set the basics on superconducting qubits. We discuss the principles of superconductivity and the importance of the Josephson effect (Sec. 1.2.1). Here, we delve into the quantum harmonic oscillator (Sec. 1.2.2), and the transmon regime (Sec. 1.2.3), and explore the phenomena of decoherence and dephasing (Sec. 1.2.4). We also introduce the control and readout mechanisms of superconducting qubits (Sections 1.3 and 1.4).

Chapter 2 describes the experimental set-up used in this work. We begin with an overview of the dilution refrigerator and cryogenic electronics (Sections 2.1 and 2.2), followed by a description of the devices under test (Section 2.3). This chapter also outlines the methodologies for single-qubit characterization, including spectroscopy experiments and time-domain protocols (Section 2.6.2).

In Chapter 3, we introduce the two-qubit coupling schemes, emphasizing coupling mechanisms for the implementation of two-qubit gates. This chapter provides insights into a comparative study of designs of non-direct qubit-qubit coupling through fixed (Sec. 3.1) and tunable couplers (Sec. 3.2), and a discussion on the implementation of the i-SWAP gate in both configurations, highlighting advantages and disadvantages (Sec. 3.3).

In Chapter 4 we show our experimental results and we discuss their validity with respect to the theoretical expectations and results in literature. Specifically, we focus on the study of the avoided level crossings for different pairs in the two devices (Sec. 4.4.1). Finally, we report our initial results on the SWAP experiment conducted on the prototype device with the tunable coupling scheme (Sec. 4.4.4).

# –1–
# Introduction to superconducting qubits

Contents: **1.1 Qubits: An Overview. 1.2 Introduction to superconducting circuits.** 1.2.1 Josephson effect – 1.2.2 Quantum harmonic oscillator – 1.2.3 Transmon regime for superconducting qubits – 1.2.4 Decoherence and dephasing. **1.3 Superconducting qubit control.** 1.3.1 Capacitive coupling for X,Y operation – 1.3.2 Flux-tunable transmon: physical Z control. **1.4 Qubit readout: the Jaynes-Cummings model.** 1.4.1 Quantum non-demolition readout.

## 1.1 Qubits: An Overview

In this chapter, we want to introduce the key elements to understand the implementation of superconducting circuits into the frame of quantum computing.

Traditional computing systems operate on classical bits, which encode information as either a zero or a one. In a quantum computer, the laws of quantum physics allow phenomena like superposition and entanglement [13]. The fundamental unit for a quantum computer is a two-level quantum system with a ground $|0\rangle$ and an excited state $|1\rangle$. We refer to such a system as a quantum bit or *qubit*.

The superposition of $|0\rangle$ and $|1\rangle$ states can be represented as points on the surface of the Bloch sphere, as depicted in Figure 1.1b [14]. As a consequence, in quantum computing is possible to encode any information in a quantum state vector:

$$|\Psi\rangle = \alpha |0\rangle + \beta |1\rangle = \cos\frac{\theta}{2} |0\rangle + e^{i\phi} \sin\frac{\theta}{2} |1\rangle, \tag{1.1}$$

where $|\alpha|^2 + |\beta|^2 = 1$, due to the unitarity of the Bloch sphere. To map an arbitrary superposition of $|0\rangle$ and $|1\rangle$ to a point on the sphere, we use the parametrization in terms of the *polar angle* $\theta$ and the *azimuthal angle* $\phi$, as shown in Eq. 1.1.

A two-level quantum system can be realized through various approaches, such as using the two spin states of a 1/2 spin particle, or exploiting the vertical and horizontal

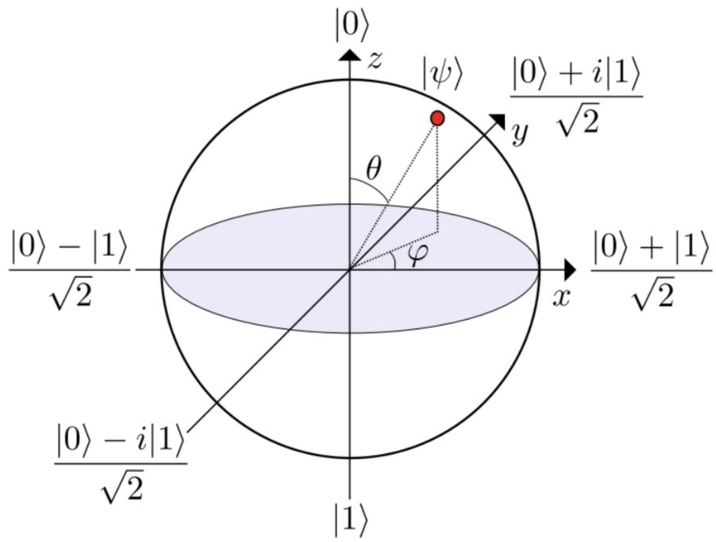


Figure 1.1: Visualization on the Bloch sphere of a qubit state.

polarization states of a single photon [15]. In this context, *Di Vincenzo* has outlined a set of criteria for constructing a system capable of executing quantum computational processes [16]:

1. *A scalable physical system with well-characterized qubits.* It is essential for the system to clearly manifest the quantum properties of the two-level system. Additionally, it should be accurately known the dynamics of interactions with other qubits or external fields employed for control purposes.

2. *The ability to initialize the state of the qubits to a simple fiducial state.*

3. *Long relevant decoherence times.* As we will see later, decoherence times characterize the dynamics of a qubit in contact with its environment.

4. *A "universal" set of quantum gates.*

5. *A qubit-specific measurement capability.* The result of a computation must be read out, and this requires the ability to measure the state of specific qubits.

Superconducting circuits are currently one of the leading approaches for realizing quantum logic elements and quantum coherent interactions with sufficiently high controllability and low noise. Therefore, they are viable candidates for implementing medium- and large-scale quantum computation [17].

In particular, they have shown great versatility in the **design** possibilities, which means a control on different parameters, such as the qubit energy level and the coupling force. As we will see further, this can be achieved by adjusting the parameters of superconducting circuits, which embed unique key structures able to provide fundamental

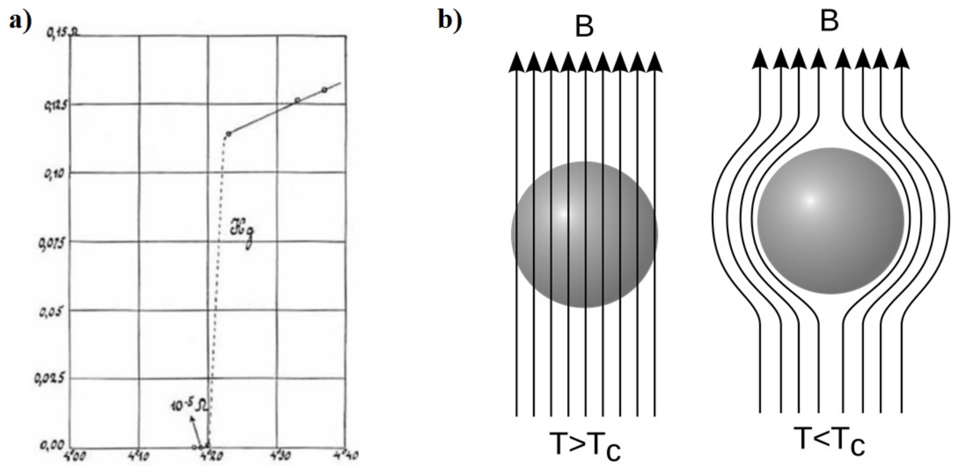


Figure 1.2: In **a)**, plot of the resistance (measured in *Ohms*) of mercury as a function of temperature (expressed in *Kelvin*). Here, the superconducting transition Occurs at $T_C = 4.2K$. Figure from [21]. In **b)**, pictorical representation of the Meissner effect. Within a superconducting material, as it is cooled below its critical temperature $T_C$, magnetic field lines are actively expelled.

non-linearity in the system, namely the Josephson junctions. As a result, the Hamiltonian of superconducting qubits can be precisely engineered.

The fabrication of superconducting qubits is based on the existing microfabrication processes. High-quality devices can be prepared by leveraging advanced chip-making technologies, which is advantageous for both production and **scalability**. The operation and measurement of superconducting qubits are compatible with microwave **control** and operability. Thus, commercial microwave also equipment can be used in superconducting quantum computing experiments. Additionally, the architecture of superconducting qubit circuits facilitates the **coupling** of multiple qubits [18].

In this thesis, we will focus on qubits based on superconducting *Transmon* circuits, a Charge qubit [19] characterized by a large shunt capacitance that makes it insensitive to charging noise. This design has demonstrated its applicability in quantum computing, a claim substantiated in 2019 by the *Google AI Quantum group*'s work on the *Sycamore* processor [8] and the recent advancements by the *IBM Quantum group* with the IBM Eagle processor [20].

## 1.2 Introduction to superconducting circuits

We begin our discussion with an overview of superconducting circuits, providing some insights into the phenomenon of superconductivity. A material is classified as superconducting when it exhibits two simultaneous behaviors below a specific temperature: ***perfect conductivity*** and ***perfect diamagnetism***.

In 1908 *H. Kammerlingh Onnes* succeeded in liquefying helium, being able to cool down different materials at around 4.2K. Building on this achievement, in 1911, he experimentally observed the first evidence of superconductivity [21]. As shown in Fig. 1.2, at temperatures below a critical value denoted as $T_C$, a mercury sample displayed zero resistance [22].

The phenomenon of *perfect diamagnetism*, which is the second fundamental characteristic of superconductivity, was unveiled by Meissner and Ochsenfeld in 1933 [23]. Their observation revealed that magnetic field lines within a normal material were expelled from the sample once it was cooled below $T_C$, and a critical magnetic field $H_C$. This observation provided conclusive evidence that superconductivity is a distinct thermodynamic state [24].

In this thesis, the main focus is on quantum superconducting circuits, which mainly use Niobium (Nb, $T_C = 9.3\ K$) and Aluminum (Al, $T_C = 1.2\ K$), two *low-temperature* superconductors that offer a good balance of superconducting properties (such as critical temperature and superconducting gap), fabrication reliability, and cost [25][26].

The foundational framework of microscopic superconductivity theory was first formulated in 1957 by Bardeen, Cooper, and Schrieffer (BCS theory) [27] and well applies to all so-called traditional *low critical temperature* superconductors, as in the case of *Nb* and *Al* [28]. The superconducting state is a *macroscopic quantum state* [29], characterized by the unique property of an electric current density with a charge $e^*$, twice that of the elementary electronic charge $e$. This behavior emerges due to a weak residual attraction between pairs of electrons—known as *Cooper pairs*—resulting from their interaction with lattice oscillations [30].

Using the language of second quantization we define the *creation operator* $a^+_{\uparrow,k}$ which creates an electron of momentum $\mathbf{k}$ and spin up, as well the annihilation operator $a_{\uparrow,k}$ which destroys the corresponding state [24]. Under the assumption of a *pairing Hamiltonian* (refer to, for instance, *Tinkham, 1996, Chapter 3*) [24], we introduce the ground state of a superconductor as:

$$|BCS\rangle = \prod_k \left(|u_k| + |v_k|\, e^{i\phi} a^+_{\uparrow,k} a^+_{\downarrow,-k}\right) |0\rangle\ . \tag{1.2}$$

Here, $|0\rangle$ denotes the vacuum state. The coefficients $u_k$ and $v_k$, are the *coherence factors* [30] and satisfy the normalization condition $|u_k|^2 + |v_k|^2 = 1$. From Eq. 1.2, we can see that $|u_k|^2$ and $|v_k|^2$ are respectively related to the probability that the pair $(\mathbf{k}\uparrow, -\mathbf{k}\downarrow)$ is occupied, and unoccupied.

Notably, the phase $\phi$ corresponds to the phase of a *macroscopic condensate wave function* for the Cooper pair, denoted as $\Psi_s(\mathbf{r})$ [29] [31]. Indeed, we can introduce the *order parameter* of the superconductor [30], $\Delta(\mathbf{r})$, that describe the quantum coherent behavior of the electrons in the system:

$$\Delta(\mathbf{r}) \propto \Psi_s(\mathbf{r}) = \sqrt{n_s(\mathbf{r})/2}\, e^{i\phi(\mathbf{r})}. \tag{1.3}$$

It is important to note that this parameter is normalized to the density of Cooper pairs (half of the electron density within the condensate, $n_s$ [30]).

The behavior of the macroscopic wave function can be observed within a finite length. For example, at an interface between a superconductor and a normal metal where

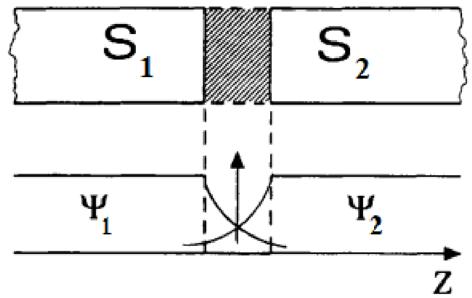


Figure 1.3: Schematic of a Josephson Junction and behavior of the macroscopic condensate wave function $\Psi_{1,2}(\mathbf{r})$ of the two superconductors. Figure adapted from [29].

superconductivity is suppressed, the order parameter regains its bulk value within a characteristic scale called *coherence length* $\xi_0 = \hbar v_F/\pi|\Delta|$, where $v_F$ is the Fermi velocity [32]. Typically this length is of the order 10-100 nm [29].

### 1.2.1 Josephson effect

Consider two superconductors $S_1$ and $S_2$ separated by a non-superconducting material such as a normal metal or an insulator, depicted schematically in Fig.1.3. If this barrier is an insulator and does not exceed the coherence length, typically 1-2 nm, we observe an overlap of the macroscopic wave functions of the two superconductors. In 1962, B. Josephson predicted a current flow inside the barrier [33], with a consequent flow of Cooper pairs in the absence of a potential drop, which reads as:

$$I = I_C \sin\phi, \tag{1.4}$$

where $\phi = \phi_1 - \phi_2$ is the difference in the macroscopic phases of the two superconductors and $I_C$ is the maximum current allowed for the Cooper pairs flow. The Eq. 1.4 describes the *dc Josephson effect*, which is characterized by a coherent and non-dissipative electric current flowing through the barrier. In the presence of a voltage $V$, Josephson predicted that the phase difference would evolve according to:

$$\frac{d\phi}{dt} = \frac{2\pi V}{\Phi_0}. \tag{1.5}$$

Here $\Phi_0 = \frac{hc}{2e}$ represents the flux quantum [29]. Eq. 1.4 together with Eq. 1.5 are the constitutive relations of the *Josephson effect* [29]. Using the two *Josephson equations* together with the general definition of inductance, $V = L\dot{I}/c^2$, we see that the Josephson junction, when operated below the critical current for typical superconductors in quantum circuits [34], behaves like a *nonlinear inductance* $L_J$:

$$L_J(\phi) = \frac{\hbar c^2}{2eI_c\cos\phi}. \tag{1.6}$$

## 1.2.2 Quantum harmonic oscillator

An important property of the Josephson junction is its nonlinear contribution to the system's equivalent inductance. To explore this feature, we consider a linear element in the form of a simple lumped-element circuit, known as the *quantum LC oscillator* [35]. An LC oscillator is characterized by a capacitance (C) and an inductance (L), as shown in Figure 1.4a. For this circuit, the stored energy can be described by the following expression [36]:

$$\int_{-\infty}^{t} I(t')V(t')dt'. \tag{1.7}$$

We define at this point as degrees of freedom of the system the flux and the charge, respectively [36]:

$$\Phi(t) = \int_{-\infty}^{t} V(t')dt', \tag{1.8}$$

$$Q(t) = \int_{-\infty}^{t} I(t')dt', \tag{1.9}$$

where the circuit is supposed to be at rest at time $t = -\infty$ for zero voltages and currents.

From Eq. 1.7, we can define the total energy of the oscillator as the sum of its charging and inductive energy [34][35][14]:

$$H_{LC} = \frac{Q^2}{2C} + \frac{\Phi^2}{2L}. \tag{1.10}$$

Here, we recognize the analogy to a *mechanical harmonic oscillator*, where the capacitance plays the role of the mass, and the resonant frequency is given by $\omega_r = 1/\sqrt{LC}$. However, this Hamiltonian is classical, and to proceed with a quantum-mechanical description of the system, we need to consider the charge and flux variables as non-commuting observables satisfying the commutation relation [30][14][37]:

$$\left[\hat{\Phi}, \hat{Q}\right] = i\hbar. \tag{1.11}$$

Following the analogy with the harmonic oscillator [34], we can now introduce the standard annihilation $\hat{a}$ and creation $\hat{a}^+$ operators:

$$\hat{\Phi} = \Phi_{zpf}\left(\hat{a}^+ + \hat{a}\right), \quad \hat{Q} = iQ_{zpf}\left(\hat{a}^+ - \hat{a}\right). \tag{1.12}$$

Here $Q_{zpf} = \sqrt{\hbar\omega_r C/2}$ and $\Phi_{zpf} = \sqrt{\hbar/2\omega_r C}$ represent the magnitudes of the *zero-point fluctuations* of charge and flux, respectively. Thus, we can proceed to the quantization of the *LC oscillator* [35][34]:

$$H_{LC} = \left(\hat{a}^+\hat{a} + \frac{1}{2}\right), \tag{1.13}$$

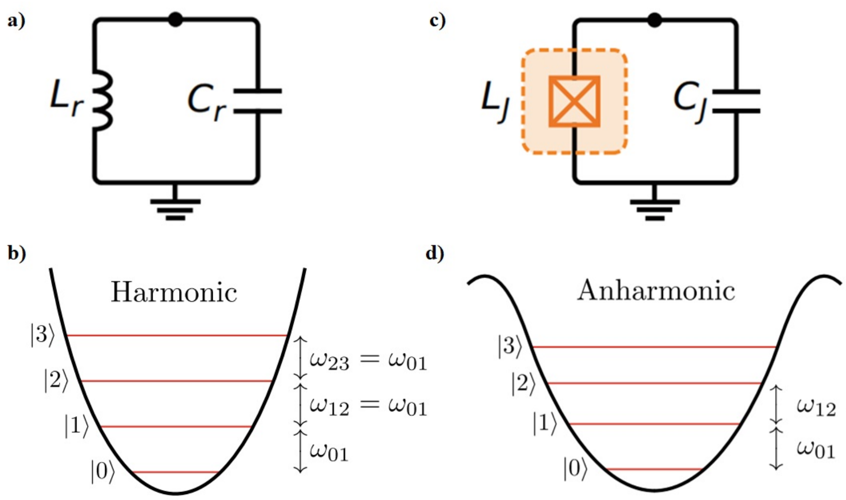


Figure 1.4: a) Lumped-element representation of a parallel LC-oscillator. In b), the quadratic potential (black curve) of a harmonic system with the equidistant energy level separation. In c) schematic of the Josephson qubit circuit with the non-linear inductance $L_J$ highlighted in the orange box, in parallel with the self-capacitance $C_J$. In d), we can observe the reshaping into the cosine potential characteristic of a Josephson junction, resulting in non-equidistant energy level spacing. Figure adapted from [13].

where the operator $\hat{a}^+$ is responsible for creating a photon of frequency $\omega_r/2\pi$ in the circuit, as well the destruction by the annihilation operator $\hat{a}$.

### 1.2.3 Transmon regime for superconducting qubits

A degree of non-linearity is essential to codify and manipulate quantum information [38]. Fortunately, superconductivity allows non-linearity to be introduced into quantum electrical circuits without losses [34]. Here we take advantage of the *Josephson junction* (JJ), as seen in Eq. 1.6.

Replacing the geometric inductance $L$ by a JJ, see Fig. 1.4b, we obtain an anharmonic behavior, which provides a non-equidistant separation of energy levels, see Fig. 1.4d, as occurring in an *artificial atom* [39]. This allows us to identify a computational basis associated with the first two energy levels, separated by $\hbar\omega_{01}$. Using Eq. 1.7 together with the Josephson equations 1.4 and 1.5, we get the energy energy stored in the JJ:

$$I_c \int \sin\hat{\phi}\, d\phi = -E_J \cos\hat{\phi}, \tag{1.14}$$

where $E_J = I_c\Phi_0/2\pi$ is the Josephson energy.

Consider biasing the circuit in Fig. 1.5a, also known by the name of *Cooper Pair Box (CPB)*, using an external voltage source $V_g$. As a result, the quantized Hamiltonian of the capacitively shunted Josephson junction takes the form [14]:

$$H = \frac{(\hat{Q} - Q_g)^2}{2C} - E_J \cos\hat{\phi} = 4E_C(\hat{n} - n_g)^2 - E_J \cos\hat{\phi}, \tag{1.15}$$

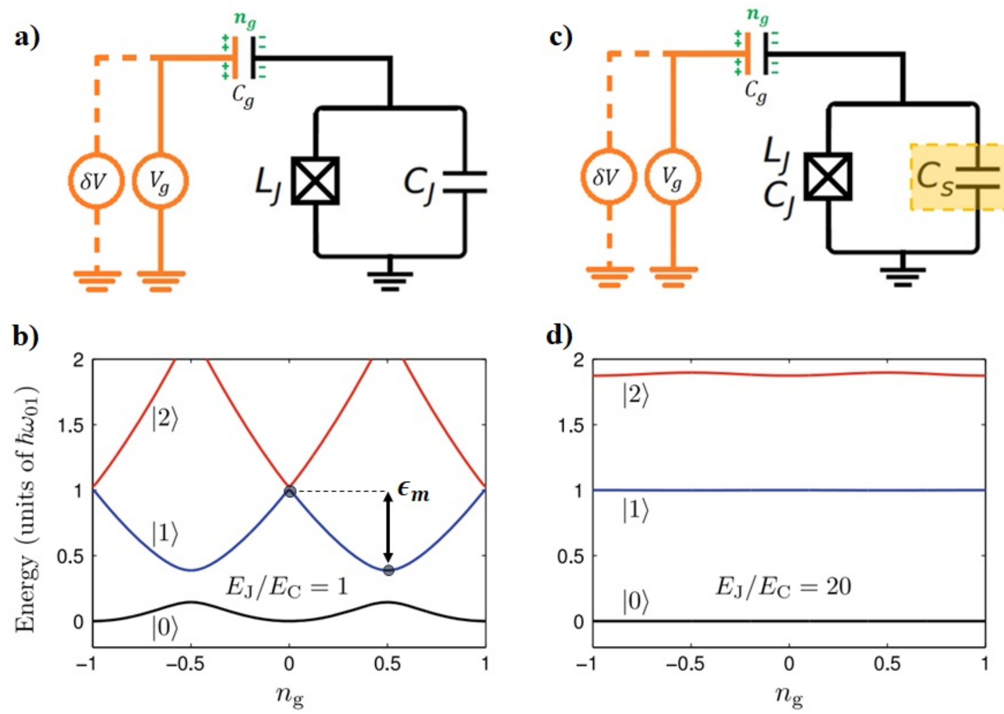


Figure 1.5: **a)** Schematic of *charge qubit* or *Cooper pair box* (**CPB**). The Josephson junction is coupled to an external voltage source $V_g$ through $C_g$. The possible presence of fluctuations and, consequently, charge variations are represented by $\delta V$. The offset charge $n_g$ is highlighted in green on the coupling capacitance $C_g$. **b)** The eigenenergies from the numerical diagonalization of Eq. 1.15 are plotted as a function of the offset charge for $E_J/E_C = 1$. The charge energy $E_C = e^2/2C$ is expressed in terms of the total capacitance $C = C_g + C_J + C_S$, where we take into account the junction capacitance ($C_J$), gate capacitance ($C_g$), and shunt capacitance ($C_S$). The latter is highlighted in **c)**, where the nonlinear inductance $L_J$ is shunted by a capacitance $C_S$, through which it is possible to increase the ratio $E_J/E_C$. For simplicity, the self-capacitance of the junction $C_J$ has been integrated into the notation of the JJ. As shown in **d)**, at high $E_J/E_C$ ratios the dependence of the *charge dispersion* $\epsilon_m$ by charge fluctuations decreases drastically, see Eq. 1.16. Figures adapted from [40][13].

where $\hat{n} = \hat{Q}/2e$ is the operator number of *Cooper pairs*. Due to the external gate voltage, the charge energy is affected by an offset charge $n_g = Q_g/2e$. This model allows us to describe the circuit's coupling with the environment, which can be imagined as a battery with a fluctuating voltage, represented by $\delta V$, due to the inevitable presence of spurious and unwanted charges in the circuit environment [34].

The Eq.1.15 can be solved exactly in the phase basis to obtain the eigenenergies $E_m$ [34][40]. In Fig. 1.5b-d, the eigenenergies are plotted as a function of $n_g$, emphasizing the dependence of the spectrum of Eq. 1.15 on the ratio $E_J/E_C$. For $E_J/E_C \sim 1$, the spectrum strongly depends on the offset charge. This implies that even when biasing the circuit at the *sweet spots*, i.e. where $\frac{dH}{dn_g} = 0$ (see Fig. 1.5b), the circuit operations can be limited by higher-order effects of the $1/f$ charge noise [34][40]. To overcome this limitation, the ratio $E_J/E_C$ is increased significantly, leading to the *transmon regime* [40]. The crucial modification distinguishing the transmon from the CPB is a shunting connection of the

Josephson junction via a large capacitance $C_S$, accompanied by a similar increase in the gate capacitance $C_g$ (Fig. 1.5c) [14]. The sensitivity of the system to charge noise is quantified by the peak-to-peak value for the *charge dispersion* of the $m_{th}$ energy level [40], as shown in Fig. 1.5b:

$$\epsilon_m = E_m(n_g = \frac{1}{2}) - E_m(n_g = 0). \tag{1.16}$$

In Fig. 1.6a is depicted the charge dispersion as a function of $E_J/E_C$. Studying the spectrum of Eq. 1.15 in the transmon regime, where $E_J/E_C \sim 10 - 100$, we observe:

$$\epsilon_m \simeq e^{-\sqrt{8E_J/E_C}}. \tag{1.17}$$

This exponential dependence ensures that the *transmon qubit* is well-protected against low-frequency charging noise [34][40]. However, as shown in Fig. 1.5d, the anharmonicity of the energy levels diminishes in the transmon regime. We define the *absolute* and *relative* anharmonicity as:

$$\alpha = E_{12} - E_{01}, \quad \alpha_r = \frac{\alpha}{E_{01}}. \tag{1.18}$$

Investigating the anharmonicity evaluated at the charge degeneracy point $n_g = 1/2$, we obtain the following asymptotic expressions [40]:

$$\alpha \simeq -E_C, \quad \alpha_r \simeq -\frac{1}{\sqrt{8E_J/E_C}}. \tag{1.19}$$

This result ensures that while the charge dispersion diminishes exponentially with increasing $E_J/E_C$, the reduction in anharmonicity exhibits a much weaker dependence on this ratio. This characteristic allows to engineer an effective two-level system within the transmon regime, typically at $E_J/E_C = 10 - 100$ (refer to Fig. 1.6b), leading to a significant enhancement in relaxation and dephasing times [40][41].

In Eq. 1.15 the operator $\hat{n}$ together with the *gauge-invariant phase* introduced in 1.2 form a canonical conjugate pair, obeying the commutation relation $[e^{i\hat{\phi}}, n] = e^{i\hat{\phi}}$ [30][42]. The variance of the charge degree of freedom is large when $E_J/E_C \gg 1$, and the variance of its conjugate variable $\hat{\phi}$ is correspondingly small [34], so the commutation relation above, not taking in account the fact that $\hat{\phi}$ is periodic (see Ref. e.g. [30][42]), reads as:

$$\left[\hat{\phi}, \hat{n}\right] = i. \tag{1.20}$$

This means that in the *transmon regime*, we can neglect the offset charge, since now the system is insensitive to this parameter [34], and expand the cosine in Eq. 1.15 to the $4_{th}$ order:

$$H = 4E_C\hat{n}^2 - E_J \cos\hat{\phi} \simeq 4E_C\hat{n}^2 + \frac{1}{2}E_J\phi^2 - \frac{1}{4!}E_J\phi^4. \tag{1.21}$$

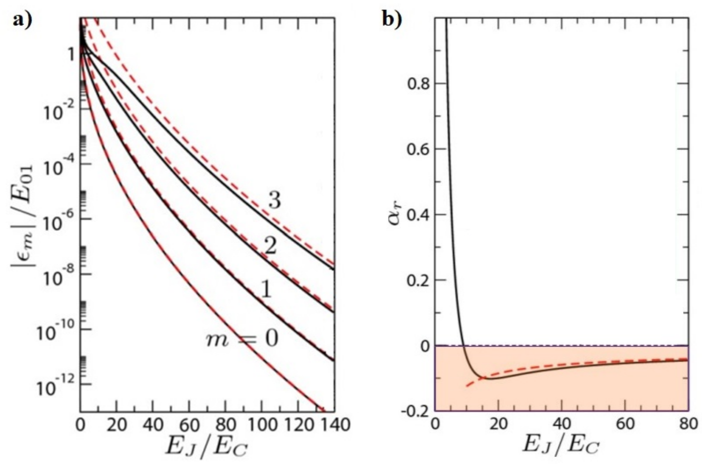


Figure 1.6: Figure **a)** shows the plot of charge dispersion $|\epsilon_m|$ normalized to the $E_{01}$ transition as a function of the ratio $E_J/E_C$ for the lowest four levels. The solid line represents the exact solution obtained from Eq. 1.15, while the dashed curve depicts the relative asymptotic solution given by Eq. 1.17. **b)** displays the relative anharmonicity obtained at the degeneracy point as a function of the ratio $E_J/E_C$. The solid curves show the exact results obtained from Eq. 1.15, while the dashed curves represent the asymptotic behavior as given by Eq. 1.19. In orange, the region of weak negative anharmonicity is highlighted, where the transmon circuit is operated. These figures have been adapted from Ref. [40].

In analogy with Eq. 1.12 we can introduce creation and annihilation operators $\hat{b}$ and $\hat{b}^+$ for the de-excitations and excitations of the system, respectively [34]:

$$\hat{\phi} = \left(\frac{2E_C}{E_J}\right)^{1/4}\left(\hat{b}^+ + \hat{b}\right), \quad \hat{n} = \frac{i}{2}\left(\frac{E_J}{2E_C}\right)^{1/4}\left(\hat{b}^+ - \hat{b}\right). \tag{1.22}$$

Substituting these into Eq. 1.15, we obtain:

$$H = \sqrt{8E_JE_C}\hat{b}^+\hat{b} - \frac{E_C}{12}\left(\hat{b}^+ + \hat{b}\right)^4 \simeq \hbar\omega_q\hat{b}^+\hat{b} - \frac{E_C}{2}\hat{b}^+\hat{b}^+\hat{b}\hat{b} \tag{1.23}$$

Here

$$\hbar\omega_q = \sqrt{8E_JE_C} - E_C \tag{1.24}$$

represents the transition frequency between the ground and the first excited state, as shown in Fig. 1.7a. In Eq. 1.23 is employed the *Rotating Wave Approximation* (RWA). This approximation neglects interactions that do not preserve the photon number, and thus the not-conserving energy terms [30]. This *RWA* remains valid within the transmon regime, where $\hbar\omega_q \gg E_C/4$ [34]. From this, we can observe that the behavior of the transmon circuit is essentially that of a *weakly anharmonic oscillator* (AHO) [14]. For quantum information processing, even in the presence of this weak nonlinearity, it is then possible to consider only the ground and first excited states preventing undesired transitions to other states [34]. In this scenario, the transmon operates as a two-level system, or a *qubit* [14]. Thus, introducing the Pauli-z operator $\hat{\sigma}_z$, we can simplify the Hamiltonian above to:

$$H = \frac{\hbar\omega_q}{2}\hat{\sigma}_z. \tag{1.25}$$

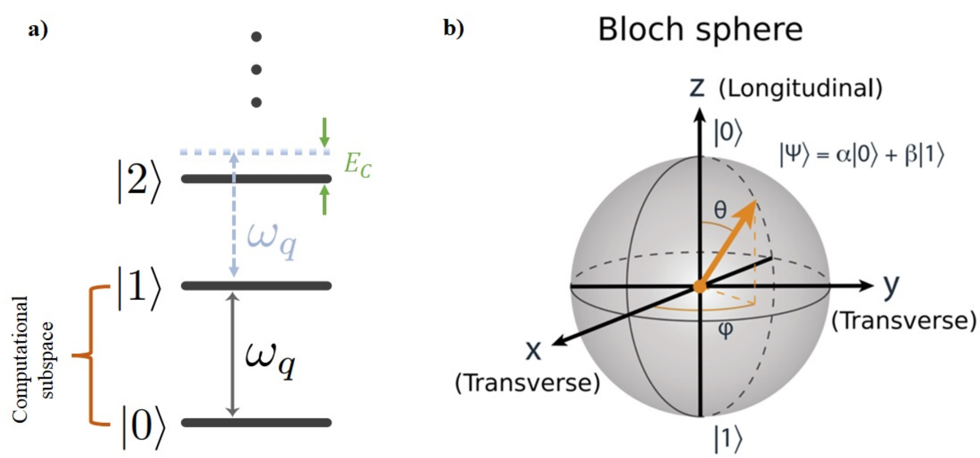


Figure 1.7: **a)** Two-level system configuration, where the computational basis and the weak anharmonicity of the system are highlighted. **b)** The Bloch sphere offers a visualization of the quantum state $|\Psi\rangle = \alpha\,|0\rangle + \beta\,|1\rangle$. In this representation, the qubit's quantization axis – the *z axis* – aligns longitudinally within the qubit frame, corresponding to the $\sigma_z$ term in the qubit Hamiltonian 1.25. The *x-y plane* resides transversely within the qubit frame [14].

In terms of the eigenvector of the *Pauli matrix* $\sigma_z$, we can define the ground state $|0\rangle$ and an excited state $|1\rangle$ of the two-level quantum system [43], see Fig. 1.7a:

$$|0\rangle = \begin{pmatrix} 1 \\ 0 \end{pmatrix}, \quad |1\rangle = \begin{pmatrix} 0 \\ 1 \end{pmatrix}. \tag{1.26}$$

### 1.2.4 Decoherence and dephasing

As discussed in the previous section, the transmon circuit behaves as a two-level system. A two-level quantum system is described by Eq. 1.1, where the ground and excited states of a qubit, are metaphorically referred to as the *north pole* $|0\rangle$ and *south pole* $|1\rangle$, respectively [30][14]. The *qubit quantization axis* is described by the *longitudinal axis* (z-axis), connecting the north and south poles. Meanwhile, the *x-y* plane constitutes the *transverse plane* [14], as shown in Figure 1.7b. In this spherical coordinate system, the qubit frequency can be visualized on the Bloch sphere as a precession around the z-axis of the unit *Bloch vector* $\vec{a} = (\sin\theta\cos\phi, \sin\theta\sin\phi, \cos\theta)$. We represent the Bloch sphere in a reference frame where the x and y-axes also rotate around the z-axis at the qubit frequency. As we will see in Sec. 1.3.1, this is called *rotating frame* [14]. In the rotating frame picture, the Bloch vector is stationary on the Bloch sphere. Being $|\Psi\rangle$ a pure state, we can introduce the density matrix:

$$\rho = |\Psi\rangle\langle\Psi| = \frac{1}{2}(I + \vec{a}\cdot\vec{\sigma}) = \begin{pmatrix} \cos^2\frac{\theta}{2} & e^{-i\phi}\cos\frac{\theta}{2}\sin\frac{\theta}{2} \\ e^{i\phi}\cos\frac{\theta}{2}\sin\frac{\theta}{2} & \sin^2\frac{\theta}{2} \end{pmatrix} = \begin{pmatrix} |\alpha|^2 & \alpha\beta^* \\ \alpha^*\beta & |\beta|^2 \end{pmatrix}. \tag{1.27}$$

More generally, the surface of the unit sphere represents pure states, and its interior mixed states [14].

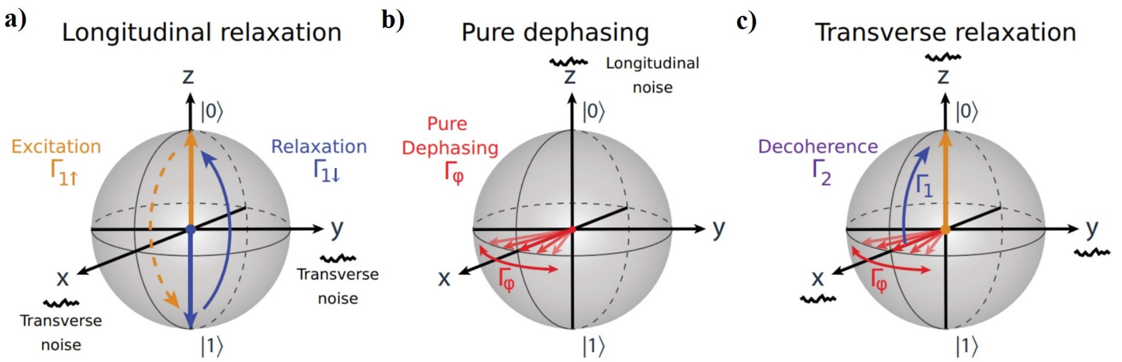


Figure 1.8: **a)** Longitudinal relaxation processes due to transverse noise that couples to the qubit in the x-y plane and drives transitions. In blue, the emission process of energy to the environment is highlighted. In **b)** the pure dephasing due to the longitudinal noise along the $z$-axis causes fluctuations of the qubit frequency. **c)** The effect of energy relaxation and pure dephasing due to transverse relaxation with a loss-rate $\Gamma_2$. Figures adapted from [14].

We can introduce at this point the problem of noise sources weakly coupled to the qubits. The idealized systems described above, in fact, when realized in any physical implementation, will inevitably be coupled to external degrees of freedom, either intentionally via external lines to address the circuits, or unintentionally due to couplings to parasitic systems or thermal baths. These additional degrees of freedom lead to loss of the quantum information stored in the qubit [44].

In the hypothesis that these noise sources have correlation times shorter than the system dynamics, such as white noise [14][45], and assuming at $t = 0$ the initial state is described by Eq. 1.1, the impact of noise on the qubit can be modeled with the Bloch-Redfield density matrix $\rho_{BR}$ [14][45]:

$$\rho_{BR} = \begin{pmatrix} 1 + (|\alpha|^2 - 1)e^{-\Gamma_1 t} & \alpha\beta^* e^{i\delta\omega t} e^{-\Gamma_2 t} \\ \alpha^* \beta e^{-i\delta\omega t} e^{-\Gamma_2 t} & |\beta|^2 e^{-\Gamma_1 t} \end{pmatrix}, \tag{1.28}$$

where the phase $e^{i\delta\omega}$, with $\delta\omega = \omega_q - \omega_d$, accounts for the possibility that the frame is driven to rotate with a frequency $\omega_d$ different from $\omega_q$.

In the Bloch-Redfield picture, the impact of noise on the qubit accounts for three main processes [14].

**Longitudinal relaxation** accounts for depolarization along the qubit quantization axis of the qubit. As shown in Fig. 1.8a, it is caused by transverse noise, via the x- or y-axis, due to energy exchange with the environment. A qubit in state $|1\rangle$ relaxes to $|0\rangle$ with a relaxation rate $\Gamma_{1\downarrow}$. Similarly, in the exciting process the qubit in the state $|0\rangle$ absorbs energy from the environment, exciting it to $|1\rangle$, with a rate $\Gamma_{1\uparrow}$. The latter process in typical operative condition, $\hbar\omega_q \ll k_B T$, is suppressed [14], and only the down-rate contributes significantly, so $\Gamma_1 = \Gamma_{1\downarrow} + \Gamma_{1\uparrow} \approx \Gamma_{1\downarrow}$. This process is described by the longitudinal decay function $e^{-\Gamma_1 t}$, with a decay time $T_1$ and a decay rate:

$$\Gamma_1 \equiv \frac{1}{T_1}. \tag{1.29}$$

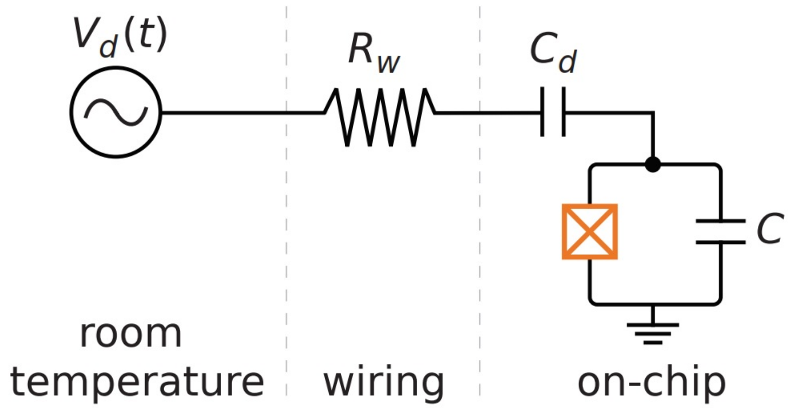


Figure 1.9: Circuit diagram illustrating the capacitive coupling between a microwave drive line characterized by a time-dependent voltage $V_d(t)$ and a generic transmon-like superconducting qubit [14].

**Pure dephasing** is an elastic process that occurs in the $x$-$y$ plane, see Fig. 1.8b, characterized by the rate $\Gamma_\phi$. This depolarization is caused by longitudinal noise that couples to the qubit via the $z$-axis. Such longitudinal noise causes the qubit frequency $\omega_q$ to fluctuate, such that it is no longer equal to the rotating frame frequency $\omega_d$.

**Transverse relaxation** describes the loss of coherence of a superposition state. This process is characterized by the rate:

$$\Gamma_2 \equiv \frac{1}{\Gamma_1} + \Gamma_\phi. \tag{1.30}$$

As shown in Fig. 1.8c, it is caused in part by longitudinal noise, which fluctuates the qubit frequency and leads to pure dephasing $\Gamma_\phi$, and by transverse noise, which leads to energy relaxation of the excited state component of the superposition state at a rate $\Gamma_1$.

## 1.3 Superconducting qubit control

In this section, we discuss methods for controlling a superconducting transmon circuit. Typically, a transmon qubit—such as those investigated in this thesis and shown in Sec. 2.3—is engineered to have capacitive couplings with both a resonator and a drive line. Additionally, it may feature inductive coupling with a local magnetic field, as is the case of the split-transmon, which will be introduced in Sec. 1.3.2.

### 1.3.1 Capacitive coupling for X,Y operation

In this section, we discuss how we can control the state of a superconducting transmon qubit. This is typically achieved by capacitively coupling a superconducting transmon qubit to a microwave source as shown in Fig. 1.9. We start considering a time-dependent driving voltage, denoted as $V_d(t)$, coupled through a capacitor $C_d$. The effect of the microwave control is to couple the drive signal to the momentum $Q$ of the circuit in Fig. 1.9 [14][46]. Taking advantage of Eq. 1.12 and Eq. 1.13 in Sec. 1.2.2, we obtain:

$$H = H_{transmon} - i\frac{C_d}{C_\Sigma}V_d(t)Q_{zpf}(\hat{a} - \hat{a}^+), \tag{1.31}$$

where $C_\Sigma = C + C_d$. In the two-level approximation, see the discussion of Sec. 1.2.3, we make the replacement $(\hat{a} - \hat{a}^+) \rightarrow i\sigma_y$, and obtain the following Hamiltonian:

$$H = \frac{\hbar\omega_q}{2}\hat{\sigma}_z + \Omega V_d(t)\hat{\sigma}_y, \tag{1.32}$$

where $\Omega = (C_d/C_\Sigma)Q_{zpf}$. To explain the role of the drive, it is advantageous to move into a frame rotating with the qubit at frequency $\omega_q$, denoted *rotating frame* [14], so the form of the drive interaction reads as:

$$\tilde{H}_d = \Omega V_d(t)\left(\cos(\omega_q t)\hat{\sigma}_y - \sin(\omega_q t)\hat{\sigma}_x\right). \tag{1.33}$$

We can assume that the time-dependent part of the voltage $V_d(t) = V_0 v(t)$, is proportional to:

$$v(t) = s(t)\sin(\omega_d t + \phi) = s(t)\big(\cos(\phi)\sin(\omega_d t) + \sin(\phi)\cos(\omega_d t)\big), \tag{1.34}$$

where $s(t)$ is a dimensionless envelope function, and the amplitude of the drive is set by $V_0 s(t)$ [14]. We adopt at this point the following notations:

$$\begin{aligned} I &= \cos(\phi) \quad \textit{In-phase component} \\ Q &= \sin(\phi) \quad \textit{Out-of-phase component}, \end{aligned} \tag{1.35}$$

so the Eq. 1.33 reduces to:

$$\tilde{H}_d = \Omega V_0 s(t)\left(I\sin(\omega_q t) - Q\cos(\omega_q t)\right)\left(\cos(\omega_q t)\hat{\sigma}_y - \sin(\omega_q t)\hat{\sigma}_x\right). \tag{1.36}$$

In the condition $|\omega_q - \omega_d| \ll |\omega_q + \omega_d|$, the terms oscillating with frequency $\omega_q + \omega_d$ average out to zero, and we can perform the *Rotating wave approximation* (RWA) as seen in the Sec. 1.2.3 [14][30]:

$$\tilde{H}_d = \frac{1}{2}\Omega V_0 s(t)\Big[\big(-I\cos(\delta\omega t) + Q\sin(\delta\omega t)\big)\hat{\sigma}_x + \big(I\sin(\delta\omega t) - Q\cos(\delta\omega t)\big)\hat{\sigma}_y\Big], \tag{1.37}$$

where $\delta\omega = \omega_q - \omega_d$. Finally reintroducing the notation of Eq. 1.34, the driving Hamiltonian in the rotating frame using the RWA can be written as:

$$\tilde{H}_d = -\Omega V_0 s(t)\begin{pmatrix} 0 & e^{i(\delta\omega t + \phi)} \\ e^{-i(\delta\omega t+\phi)} & 0 \end{pmatrix}. \tag{1.38}$$

This formulation helps us to demonstrate that through the selection of the drive's phase, direct rotations of the Bloch vector around any axis within the x-y plane become feasible.

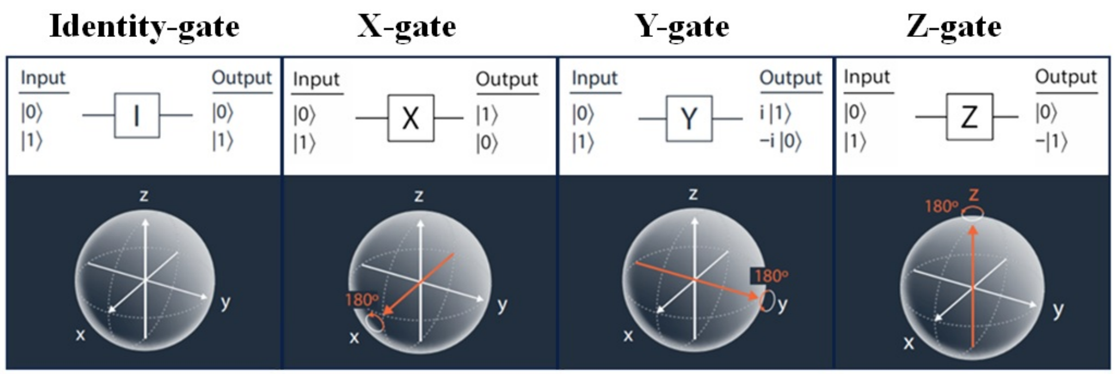


Figure 1.10: The four principal quantum single-qubit gates. For each gate, their input/output effects, corresponding circuit notations, and their relative representations on the Bloch sphere. Figure adapted from [14].

Indeed, suppose to apply a drive pulse at the qubit frequency, $\delta\omega = \omega_q - \omega_d = 0$, the drive Hamiltonian in 1.37 reads as:

$$\tilde{H}_d = -\frac{1}{2}\Omega V_0 s(t)(I\hat{\sigma}_x + Q\hat{\sigma}_y). \tag{1.39}$$

Here we see that for a drive with $\phi = 0 \;\; (Q = 0)$ we maintain only the *in-phase* component, which corresponds to rotations around the *x-axis*, while an *out-of-phase* pulse with $\phi = \pi/2 \quad (I = 0)$ corresponds to rotations around the y-axis. In practical scenarios, the execution of these rotations can achieve a remarkable level of fidelity through meticulous calibration and precise shaping of the pulses [47].

Within this framework, we now introduce *single-qubit gates*, which enable controlled manipulation of the quantum state of a qubit and serve as the building blocks for more complex quantum algorithms [14].

Single-qubit quantum operations are defined within the qubit computational basis introduced in Section 1.1, as shown in Equation 1.26. Focusing on the main four single-qubit gates depicted in Figure 1.10, we have [14]:

$$\mathbf{I} = \begin{pmatrix} 1 & 0 \\ 0 & 1 \end{pmatrix} \quad \mathbf{X} = \begin{pmatrix} 0 & 1 \\ 1 & 0 \end{pmatrix} \quad \mathbf{Y} = \begin{pmatrix} 0 & -i \\ i & 0 \end{pmatrix} \quad \mathbf{Z} = \begin{pmatrix} 1 & 0 \\ 0 & -1 \end{pmatrix}. \tag{1.40}$$

Here, the gate **I** corresponds to the identity, essentially maintaining the initial state of the qubit. The **X**-gate induces a rotation of $\pi$ around the x-axis. Similarly, the **Y**-gate and **Z**-gate enact $\pi$ rotations around the y-axis and z-axis, respectively. While microwave pulses of arbitrary amplitude and phase, on resonance with the qubit, produce rotations in the $x$ - $y$ plane, rotations around the remaining axis (z-axis), i.e., **Z**-gates, correspond to a change in the relative phase between the $|0\rangle$ and $|1\rangle$ states. A **Z**-gate can be implemented by either a composition of **X** and **Y** gates, known as a *virtual* ***Z****-gate* [48] or by detuning the frequency of the qubit with respect to the drive field for some finite amount of time, *physical Z control* [49]. One way to achieve this goal is to use *flux-tunable transmon* qubits, also named *split-transmon* [14].

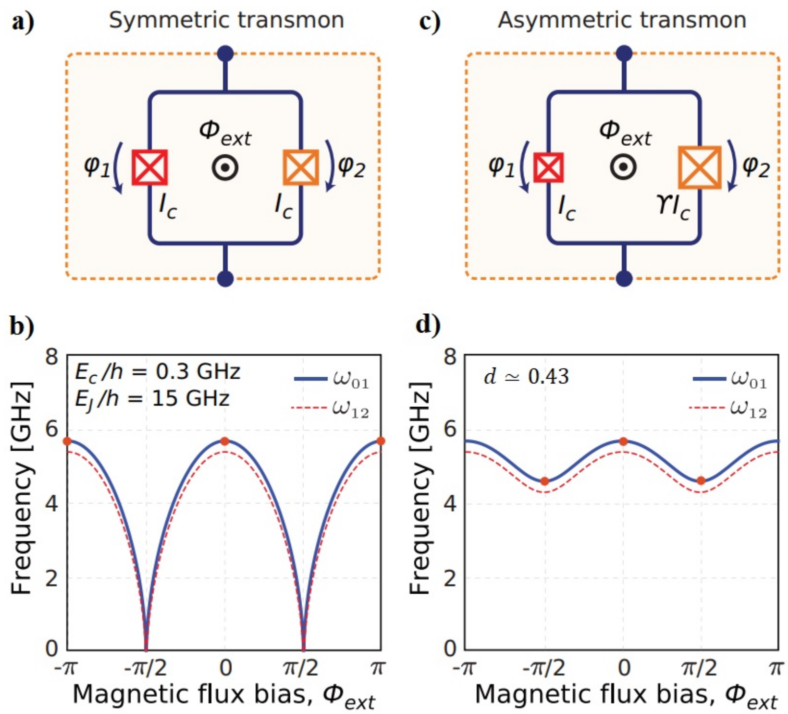


Figure 1.11: **a)-b)** Symmetric SQUID configuration, and corresponding qubit transition frequencies for the two lowest energy states as a function of applied magnetic flux in units of $\Phi_0$. **c)-d)** Asymmetric configuration with $\gamma = E_{J2}/E_{J1} = 2.5$. Here it is evident that an asymmetric fabrication returns a smaller range of tunability of the flux frequency. Figures adapted from [14].

### 1.3.2 Flux-tunable transmon: physical Z control

The necessity for achieving high-fidelity gate operations stimulated the use of qubits with tunable frequencies [14]. One approach is to introduce an additional degree of freedom in the circuit. This involves replacing the single Josephson junction (refer to Fig. 1.4b) with two parallel junctions, which form a *DC-Superconducting QUantum Interference Device* (dc-SQUID) (see Fig. 1.11a) [34]. As a result of the interference between the two arms of the SQUID, the effective critical current of the two parallel junctions can be tuned by applying an external magnetic flux $\Phi_{ext}$ through the loop (as shown in Fig. 1.11) [14]. Consequently, the Josephson energy of the circuit depends on the external flux applied $\Phi_{ext}$, and in terms of the individual Josephson energies of the two junctions, reads as:

$$E_J\left(\Phi_{ext}\right) = E_{J,\Sigma} \cos\left(\frac{\pi\Phi_{ext}}{\Phi_0}\right)\sqrt{1 + d^2\tan^2\left(\frac{\pi\Phi_{ext}}{\Phi_0}\right)}, \tag{1.41}$$

with $E_{J,\Sigma} = E_{J,2} + E_{J,1}$ and $d = \left(E_{J,1} - E_{J,2}\right)/\left(E_{J,1} + E_{J,2}\right)$ the junction asymmetry. According to Eq. 1.24, replacing the single junction with a SQUID loop yields to the flux-tunable transmon frequency, see Fig. 1.11b:

$$\omega_q\left(\Phi_{ext}\right) = \sqrt{8E_C|E_J\left(\Phi_{ext}\right)|} - E_C. \tag{1.42}$$

## 1.4 Qubit readout: the Jaynes-Cummings model

An essential circuital component of the transmon design is a *microwave resonator*, capacitively coupled to the qubit. Within the domain of the *circuit quantum electrodynamics* (cQED) device, superconducting resonators are elements that work as harmonic oscillators (red circuit in Fig. 1.12a), where the electromagnetic field is confined either in a planar two-dimensional structure, or in a 3D cavity [34]. In the first proposal of the transmon by Koch et al. (Ref. [40]), such resonator is a $\lambda/2$ *coplanar waveguide resonator* (Figure 1.12b). This configuration allows for an interaction between a two-level atom and one mode of the electromagnetic field, a scenario often approximated as the *single mode approximation* [34] [50]. From Eq. 1.13 and 1.25, the Hamiltonian of the circuit is [30][50]:

$$H = \left[\frac{\hbar\omega_q}{2}\hat{\sigma}_z\right]_{qubit} + \left[\frac{\hbar\omega_r}{2}\hat{a}^+\hat{a}\right]_{cavity} + \hbar g(\hat{a} + \hat{a}^+)(\hat{\sigma}_- + \hat{\sigma}_+). \tag{1.43}$$

In the interaction terms of the Hamiltonian, two energy-conserving processes can be identified: $\hat{a}\hat{\sigma}+$, where a photon is emitted and the atom transitions from state $|0\rangle$ to state $|1\rangle$, and $\hat{a}^+\hat{\sigma}_-$, indicating the adsorption of a photon and de-excitation of the atom. On the other hand, the processes $\hat{a}\hat{\sigma}_-$ and $\hat{a}^+\hat{\sigma}_+$ do not conserve energy. When the field mode is nearly resonant with the qubit, such that $|\omega_q - \omega_r| \ll \omega,\ g$, the *RWA* can be invoked. This allows to disregard the $\hat{a}\hat{\sigma}_-$ and $\hat{a}^+\hat{\sigma}_+$ terms [30]:

$$H = \frac{\hbar\omega_q}{2}\hat{\sigma}_z + \frac{\hbar\omega_r}{2}\hat{a}^+\hat{a} + \hbar g(\hat{a}\hat{\sigma}^+ + \hat{a}^+\hat{\sigma}_-). \tag{1.44}$$

The equation above is known as the *Jaynes-Cummings Hamiltonian*, describing the coherent exchange of a single quantum between light and matter.

The Jaynes-Cummings Hamiltonian is an exactly solvable model that accurately describes scenarios in which an atom, either natural or artificial, can be treated as a two-level system interacting with a single mode of the electromagnetic field [34]. In the absence of the coupling constant $g$, the eigenstates of the unperturbed Hamiltonian, often referred to as *bare* states [34], are denoted as $|\sigma, n\rangle = |\sigma\rangle_{qubit} \otimes |n\rangle_{field}$. Here, $\sigma = \{|0\rangle, |1\rangle\}$ represents the first two levels of the transmon, and $|n\rangle$ (where $n = 0, 1, \ldots$) corresponds to the Fock states of the resonator field.

From Equation 1.44, we observe that only transitions between the states $|0, n+1\rangle$ and $|1, n\rangle$ are permitted. Thus, the Hamiltonian 1.44 can be diagonalized within the subspace $|0, n+1\rangle, |1, n\rangle$ with eigenvalues [30][34][37]:

$$\begin{aligned} E_{\overline{|0,n+1\rangle}} =& \hbar\omega_r\left(n + \frac{1}{2}\right) - \frac{\hbar}{2}\sqrt{\Delta^2 + \Omega_{R,n}}, \\ E_{\overline{|1,n\rangle}} =& \hbar\omega_r\left(n + \frac{1}{2}\right) + \frac{\hbar}{2}\sqrt{\Delta^2 + \Omega_{R,n}}, \end{aligned} \tag{1.45}$$

and the corresponding eigenstates:

$$\begin{aligned} |\overline{0, n+1}\rangle &= \cos(\theta_n/2)\,|0, n+1\rangle - \sin(\theta_n/2)\,|1, n\rangle, \\ |\overline{1, n}\rangle &= \cos(\theta_n/2)\,|0, n+1\rangle + \sin(\theta_n/2)\,|1, n\rangle, \end{aligned} \tag{1.46}$$

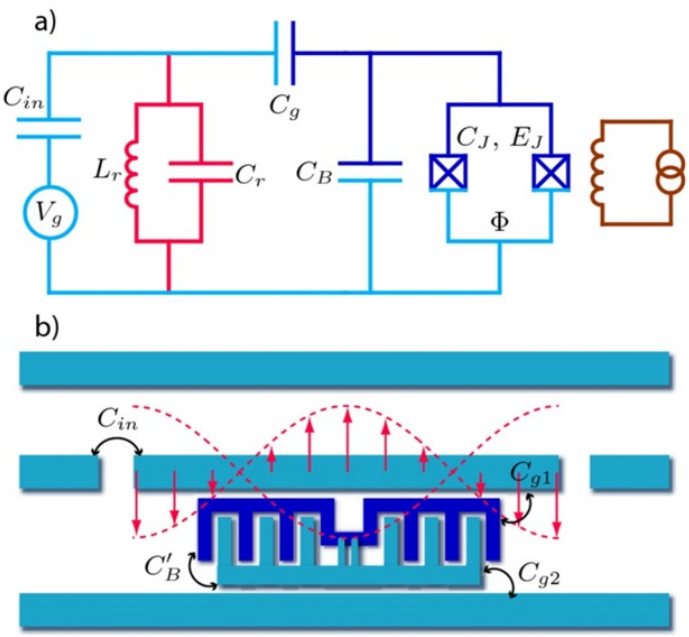


Figure 1.12: **a)** Effective circuit diagram of the flux-tunable transmon qubit (dark blue), resonator (red), flux-biasing circuit (brown), and the voltage biasing circuit (cyan). **b)** Simplified schematic of the device design showing large interdigitated capacitors designed to achieve the transmon regime $E_J/E_C \gg 1$. In this scheme, the transmon is coupled to the second harmonic, $l = 2$, of the cavity [47]. Figures adapted from [40].

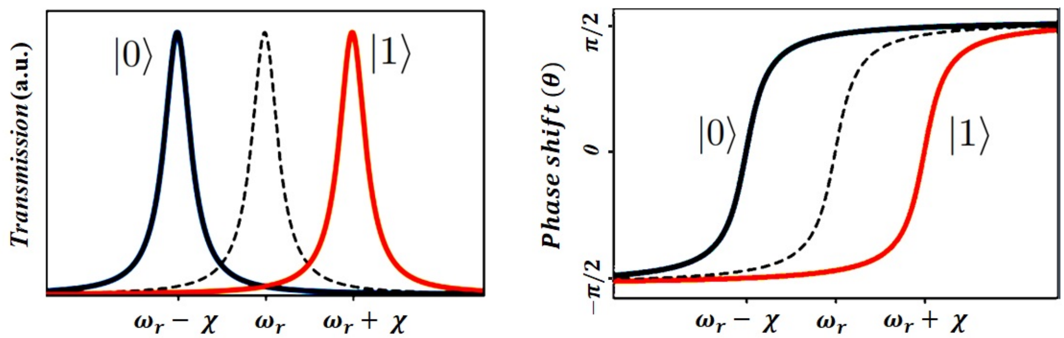


Figure 1.13: Transmission spectrum of the cavity (left), and corresponding phase shifts (right) depending on the state of the qubit (red for the excited state, black for the ground state).

with the angle $\theta_n = \arctan(\Omega_{R,n}/\Delta)$. The eigenstates of Eq. 1.46 are called *dressed states*, and are the solutions of the Jaynes–Cummings model to the problem of a qubit interacting with the field mode. In the presence of the coupling, the two-level system can no longer stay in a given state $|0\rangle$ and $|1\rangle$ since the states are now the linear combinations of the dressed states. Consequently, the probability of finding, for instance, the qubit in its ground state will oscillate with a frequency $\sqrt{\Delta^2 + \Omega_{R,n}}$, referred to as the *generalized Rabi frequency*. Here $\Omega_{R,n} = \Omega_0\sqrt{n+1}$ is $n$-photon *Rabi frequency* on resonance, i.e. when the qubit-resonator detuning $\Delta = \omega_q - \omega_r = 0$. We see that even the vacuum field ($n = 0$) can couple the two states, leading to the *vacuum Rabi frequency* $\Omega_0$ [37].

### 1.4.1 Quantum non-demolition readout

In case of detuning $\Delta = 0$ we have the maximal entanglement between qubit-resonator states implying that the qubit is, by itself, never in a well-defined state [34]. For *quantum non-demolition* (QND) readout, where the quantum measurement outcome doesn't affect the system during reading, working in the *dispersive regime* is more practical [14]. In this regime, the interaction between the field mode and the qubit does not lead to Rabi oscillations but to a mutual frequency shift of the qubit and the resonator [30]. To achieve this outcome, a canonical transformation of the field-qubit Hamiltonian 1.25 is performed, referred to as the *Schrieffer and Wolff transformation* (SWT) [30]. Assuming the system to operate far enough from resonance, with $\omega_q, \omega_r \gg |\omega_r - \omega_q| \gg g$, and using second-order perturbation theory in terms of $g/\Delta$, we have [30][34][40]:

$$H_{disp} = \frac{\hbar\omega_q'}{2}\hat{\sigma}_z + \hbar(\omega_r' + \chi\hat{\sigma}_z)\hat{a}^+\hat{a}. \tag{1.47}$$

Here, $\chi$ is the qubit state-dependent frequency shift, commonly known as a *dispersive shift*. As shown in Fig. 1.13 the mode frequency is shifted by $\mp g^2/\Delta$ depending on the state of the qubit, see Fig. 1.13:

$$\chi = \frac{g^2}{\Delta}, \quad \omega_r' \simeq \omega_r, \quad \omega_q' = \omega_q + \frac{g^2}{\Delta}. \tag{1.48}$$

The qubit frequency acquires a *Lamb shift*, induced by the vacuum fluctuations in the resonator [14]. Notably, the expression above remains valid when considering only the ground and first excited states. However, when accounting for the second excited state, a dependence on the anharmonicity emerges [34]:

$$\chi = \frac{g^2}{\Delta}\left(\frac{1}{1-\frac{\Delta}{E_c/\hbar}}\right) \quad \omega_r' = \omega_r + \frac{1}{1-\frac{\Delta}{E_c/\hbar}}. \tag{1.49}$$

Finally, we note that the second-order perturbative results of Eq. 1.47, provide a good approximation when the number of photons in the oscillator is significantly smaller than the *critical photon number* $n_c \equiv \Delta^2/(4g^2)$ [40].

# –2–
# Experimental protocols and setup



## 2.1 Dilution refrigerator

As mentioned at the beginning of chapter 1, advancements in cooling technology are pivotal for progress in superconductivity. In particular, the study of superconducting qubits can not be separated from the use of modern *dilution refrigerators* that allow to reach temperatures below $10mK$ [51].

This operating temperature holds crucial significance, as it stands precisely for an order of magnitude lower than the thermal equivalent of the energy gap between the ground and excited states in conventional superconducting qubits (Sec. 1.1). The typical frequency of a qubit is, in fact, of the order $f_{01} \approx 4 - 6$ GHz, and in terms of the *Boltzman constant* $k_B$ corresponds to a temperature around $100 - 200mK$.

In Fig. 2.2c we show the dilution refrigerator employed in this work, the *Triton 400* of the *Oxford Intrument*. It is a dilution fridge called *dry*, which differs from those of the *wet* type because of the absence of an external $^4He$ bath. The dilution refrigerator is based on the thermodynamic properties of the mixture of two Helium isotopes, $^3He$ and $^4He$. The mixture is first cooled down to the *pre-cool* temperature (of the order of 10 K) by the use of a compressor, namely the *Pulse Tube Refrigerator* (PTR), connected to the *Precool unit* (PU) (Fig. 2.2c). Using a series of heat exchangers and pressure impedance in the lines, we can reach temperatures of the order of 2 K by exploiting the Joule-Thomson effect [52]. As shown in Figure 2.1a, when the mixture is cooled below approximately 800 mK, it spontaneously undergoes a phase separation.

Once condensation of the mixture in the *Mixing Chamber* (MC) is obtained and the critical phase separation temperature is reached, the mixture in the MC will separate

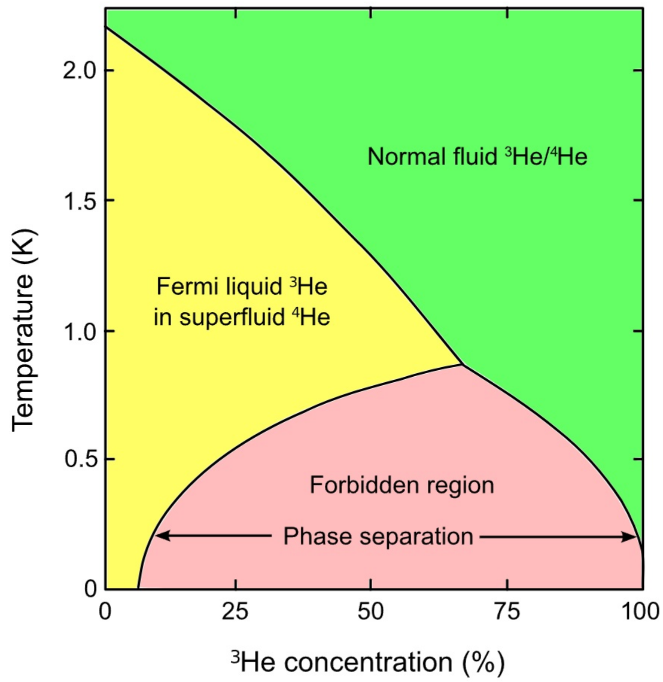


Figure 2.1: Phase diagram of the $^3He -^4 He$ mixture in terms of the temperature and $^3He$ concentration. Below the threshold of 0.8 K, we observe a phase separation of the mixture into a dilute and a concentrated phase of $^3He$, the endothermic process required to reach temperatures below 10 mK.

into two phases: a lighter $^3He$-rich phase positioned above and a denser $^4He$-rich phase below. By exploiting the endothermic nature of the evaporation process of $^3He$ from the mixture, it is possible to reach the base temperature in the MC at 10mK. In Figure 2.2b, the Dilution unit is shown, where this process is repeated cyclically so that the $^3He$ concentration is continuously restored (see Figure 2.2a) and the base temperature remains stable. Moreover, the mixture during the closed cycle passes through a trap containing activated charcoals cooled with liquid nitrogen. This sponge-like material has the function of absorbing any contaminants in the mixture.

As shown in Figure 2.2c, the cryostat consists of five plates which are characterized by different operating temperatures. The sample is thermally anchored on the bottom of the MC plate. Before starting the cooling procedure, the system is isolated with several shields. The sample is closed within a first stage *ECCOSORB*-plated tin screen, and then in a copper-plated *Cryoperm* screen to protect it from external magnetic fields and radiations, both of them thermally anchored to the MC. Additional radiative screening is placed at the Still plate, the 4K plate, and the 70K plate, while an Outer Vacuum Chamber (OVC) is placed at the RT plate, which provides the vacuum insulation in which *dry-cryostats* operate.

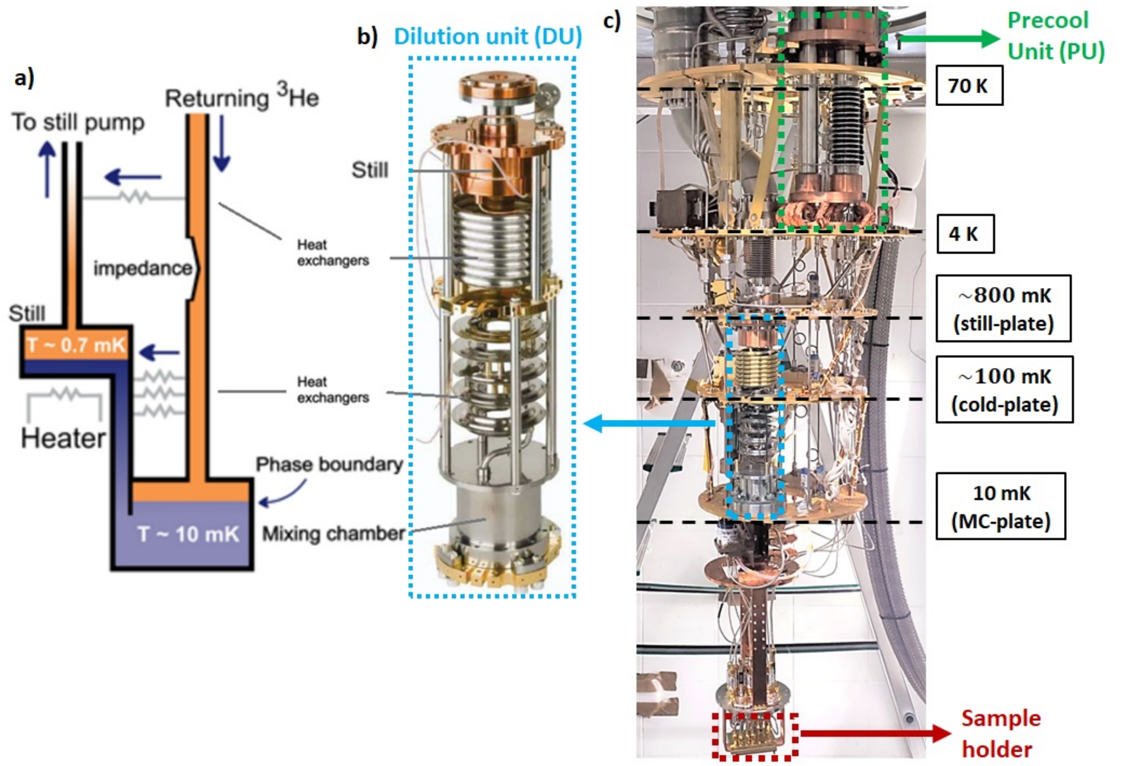


Figure 2.2: **a)** Schematics for the $^3He - ^4He$ mixture circle in the *Dilution unit* (DU). In **b)** an example of DU is presented, with the mixing chamber located at the bottom and the still chamber at the top. The heat exchangers are highlighted in the center. **c)** The *Triton 400* of the *Oxford Intrument* employed in this work. The cryostat is shown without the screens that ensure the vacuum and the isolation of the sample from radiation and external electromagnetic fields. The five plates, each denoting a specific temperature, are highlighted. Figure **a)** and **b)** adapted from [51]

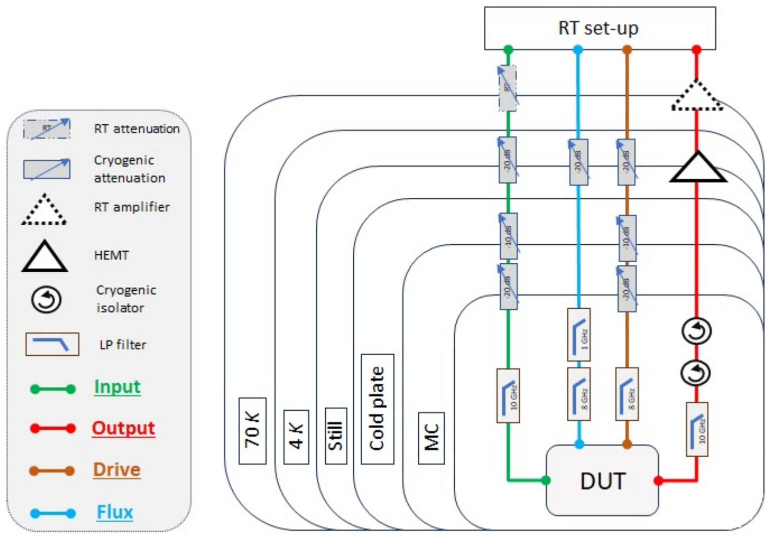


Figure 2.3: Schematic for the cryogenic lines. The input lines for the readout (green), drive (brown), and flux (blue) pass through several stages of cryogenic attenuation thermally anchored on the plates of the cryostat: the 4 K plate, the Cold plate, and the Mixing chamber (MC). An additional level of attenuation is applied at RT. In the output (red) from the sample, there are two circulators and two stages of amplification. At the 4K plate, a *High Electron Mobility Transistor* (HEMT) amplifier from *Low Noise Factory*, which can provide 40 dB of amplification within the 4-8 GHz band. At room temperature (RT), three RT amplifiers that individually provide a gain of 16 dB. Both input and output lines are connected to the input/output ports on the *Device Under Test (DUT)* through *low-pass filters*.

## 2.2 Cryogenic Electronics

The frequency band within which we interface with superconducting circuits falls within the GHz range, typically ranging from 2 to 8 GHz. To carry these microwave signals, the cryostat is equipped with dedicated coaxial cables called *RF lines*. These RF lines are divided into: a pair of 6 input RF-lines, made of stainless steel, and 2 *output* lines, made of Cu-Ni from room temperature (RT) to the 4 K plate and a superconducting alloy of Nb-Ti from 4 K to the mixing chamber (MC) plate.

In the measurements made, one of the input lines is used to convey the readout signal. The signal passes through several stages of cryogenic attenuation thermally anchored on the plates of the cryostat as shown in Fig. 2.3: the 4 K plate, the Cold plate, and the Mixing chamber (MC), up to a cryogenic attenuation level of 50 dB. As shown in Fig. 2.2, the sample is thermally anchored to the MC by a copper Cold finger. Both input and output lines are connected to the input/output ports on the sample holder through cryogenic cables and *low-pass filters*. These filters are designed as RF filters with a functional frequency range up to 8 GHz, except for the input and output of the *feedline*, where their operational range extends up to 10 GHz. In the output from the sample, there are two circulators that act as isolators. An isolator is a device that isolates an electromagnetic device from spurious reflections and transmission of an electromagnetic wave, effectively mitigating backaction phenomena [53].

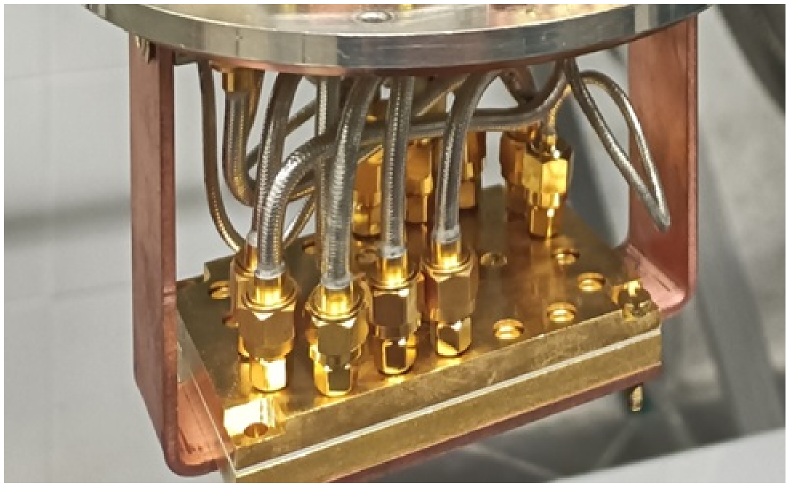

Figure 2.4: Sample holder anchored to the mixing chamber through the Copper extension and microwave lines connected to the external electronics.

The attenuated signal after interacting with the sample is amplified through two stages. The first cryogenic stage consists of a *High Electron Mobility Transistor* (HEMT) amplifier from *Low Noise Factory*, which can provide 40 dB of amplification within the 4-8 GHz band. This amplification stage is thermally anchored to the 4 K plate because the HEMT is an active amplification element that produces thermal noise on the same order of magnitude as the 4 K plate temperature. At room temperature (RT), the final stage of amplification consists of three RT amplifiers that individually provide a gain of 16 dB. In the cryostat, components such as amplifiers, attenuators, and isolators are thermally anchored to the plates to enhance efficiency and accelerate the process of thermalization during the *cool-down* process.

## 2.3 Devices under test

In this work, we studied two sample chips by QuantWare, a foundry of superconducting quantum processors located in the Delft area, in the Netherlands [11]: a *5 qubits* chip and a two-qubit chip, from now on named as *Soprano* and *Soprano_TunC* (an acronym for Tunable Coupler). The schematics of the devices are reported in Fig. 2.5a and 2.5b, respectively. Despite sharing similarities, they possess different design characteristics. Both chips are based on transmon qubits, characterized by Josephson junctions composed of aluminum electrodes and aluminum oxide barriers ($AlO_x$), with a grounding of niobium-titanium nitride (NbTiN). A detail of the transmon qubit and the Josephson junctions is reported in 2.5 c) and d), respectively. The *Soprano* device consists of 6 floating transmon qubits: 5 computational coupled qubits and 1 isolated qubit. The five computational qubits are split-transmon labeled Q0 to Q4. Q0 and Q1 have the lowest frequencies, while Q3 and Q4 have the highest frequencies. This chip design is a standard proposal for a 5-qubit multi-qubit processor [54]. In this design, Q2 is coupled to the other 4 computational

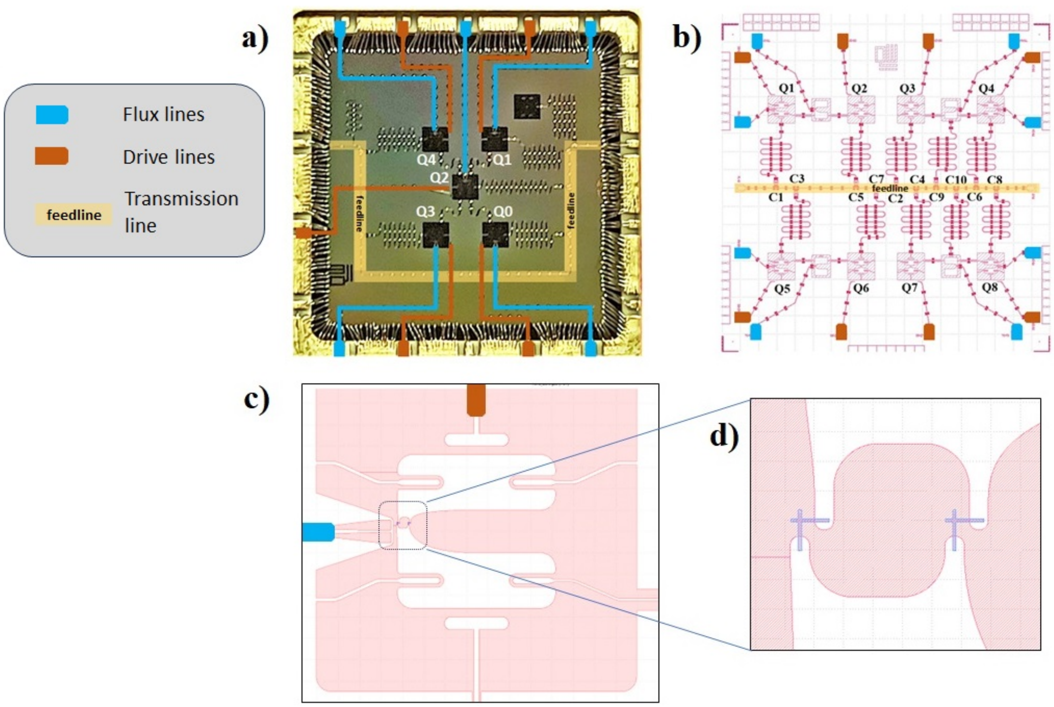


Figure 2.5: Two superconducting chips embedded in a *printed circuit board* (PCB) via wire bonds. The PCB provides the structures for grounding and microwave interconnects. In **a)** is shown the *Quantware 5-qubit chip Soprano*, with the drive and flux lines in brown and blue, respectively. The chip features a single multiplexing feedline that capacitively couples with the readout resonators associated with the 5 computational qubits, as well as the sixth isolated qubit. In this configuration, qubit 2 is designed to be capacitively coupled to the other 4 qubits through the high-frequency bus resonators. **b)** Design of the *Soprano_Tunc* chip from the collaboration between *Quantware*, *UniNA* and *Seeqc* in the frame of the *SFQ4QPU* project, which features 4 pairs of qubits coupled via tunable couplers. For each qubit transmon, there are 10 cavities for QND readout, numbered according to their frequency. *C0* is the lowest-frequency cavity and *C10* is the highest-frequency cavity. In **c)**, the layout for the split transmon is displayed, a design shared by both configurations. The capacitive coupling lines for the drive (brown) are highlighted along with the line for flux control (blue) inductively coupled with the DC-SQUID ring shown in **d)**.

qubits via high-frequency bus resonators.

The *Soprano_Tunc* is a prototype device, that includes 4 pairs of transmon qubits for diagnostic and research purposes in the frame of a collaboration between *Quantware*, the *University of Napoli "Federico II"* and the Digital Quantum Computing company *Seeqc* (*SFQ4QPU - Eurostars project*). Each pair consists of a fixed transmon and a split transmon. The coupling between the two transmons in each pair is mediated by a third qubit, which is a DC-SQUID. This design allows for tunable coupling between the two transmons. The junctions in the DC-SQUID of the split-transmon of both the chips are designed to be symmetrical, which allows for wide variation in qubit frequencies, as detailed in the Sec 1.3.2.

The designs of both chips involve computational qubits coupled with readout resonators to operate within the dispersive regime as discussed in Sec. 1.4.1. Notably, the *Soprano_Tunc* design incorporates four coupler pairs: two of them, TC34 and TC78, are equipped with a readout resonator. While providing the couplers of readout resonators isn't required for computational tasks, it is useful for study and characterization purposes.

Both the devices use a single feedline to allow for *multiplexing* measurements, in which multiple qubit states can be read at the same time by exploiting the different frequencies of the readout resonators [55]. The feedline, like the other input lines, is coupled to the 50 Ω RF electronics via pads mounted on the sample holder, which in turn couples the RF lines to the RT electronics, as discussed in the previous section (see Fig. 2.4).

The devices under test employed in this study are based on *Coplanar Waveguide* (CPW) RF lines that use *transverse electromagnetic modes* (TEM) of microwave radiations. CPWs can be engineered in such a way that we can maximize the magnetic or electric field of the TEM signal. This is useful because in some cases we need to maximize the microwave electric field (for qubit drive or readout), and in other cases, we need to maximize magnetic fields (for flux biasing of the DC SQUID) [56]. In Fig. 2.5, both chips are depicted along with their respective drive and flux lines.

Fig.2.5 displays the layout of the devices, which includes the drive line capacitively coupled to the qubit through *elbow* couplings [64], intentionally designed to maximize the electric field of the TEM modes needed for qubit drive on the Bloch sphere, as seen in Sec. 1.1. Resonators are also capacitively coupled to the qubit and feedline via interdigited capacitive coupling. Finally, flux lines are inductively coupled to the DC-SQUID to allow for control through the applied magnetic field and frequency tunability, as discussed in Sec. 1.3.2. Notably, in the *Soprano_Tunc* design, the transmon-couplers are also connected with flux lines that allow tunability.

## 2.4 Continuous wave measurement setup

Spectroscopy measurements are fundamental for the study and characterization of superconducting circuits. Employing a two-port *Vector Network Analyzer* (VNA), see Fig. 2.6a, it becomes possible to generate signals within a specific frequency range while simultaneously measuring both the amplitude and phase of the reflected and transmitted

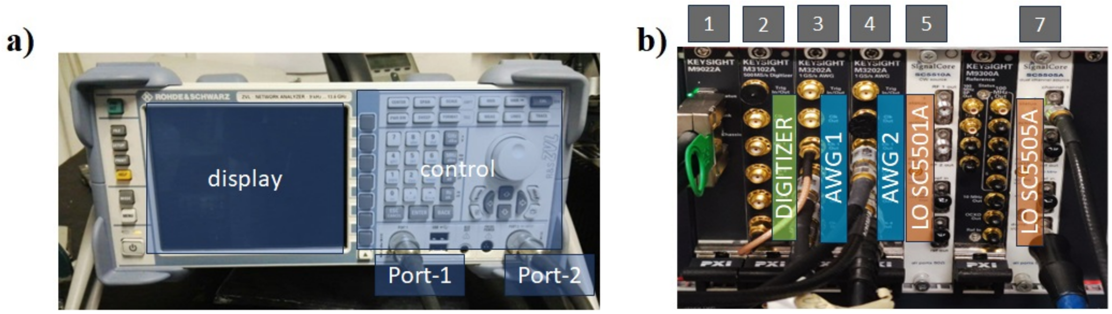


Figure 2.6: In **a)** front view of the *Rohde&Schwarz Vector Network Analyzer ZVL13*. This device is a two-port VNA, which is able to generate and measure from 9 KHz up to 13.6 GHz with a resolution of 1 Hz, and a signal attenuation range of up to 30 dB [57]. **b)** Keysight rack with instruments used for characterization of qubits in time-domain, equipped with: two *Arbitrary Waveform Generator* (AWG), from Keysight [58] (blue), able to generate waveforms in the band up to 400 MHz, and DC bias, for flux tuning. The system is also equipped with two *Local Oscillators* (LO) by Signal Core, with different generation bandwidths: up to 6 GHz [59] (slot 7) and up to 20 GHz [60] (slot 5). The digitizer from Keysight (slot 2) is used in time-domain measurements and is characterized by a sampling rate of 500 MSample/s [61]. The rack is connected to the measuring computer via slot 1. The proprietary software *Labber* [62] is employed for time-domain measurements. Spectroscopy measurements are commonly performed via the *Python* environment *QCoDeS* interface [63].

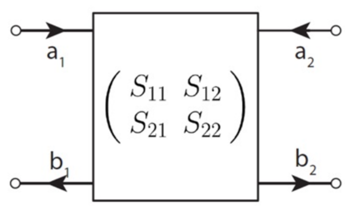


Figure 2.7: Schematic equivalent for a two-port network characterized by the four scattering parameters. Figure adapted from [65].

signals.

Given a high-frequency signal, such as the microwave range with which we work, it is more accurate to express the measurement in terms of power and energy variables. Thus, the relationship between the incident ($a_1, a_2$) and reflected ($b_1, b_2$) waves, see Fig. 2.7, is described by the following scattering matrix in terms of the scattering parameters S:

$$\begin{pmatrix} b_1 \\ b_2 \end{pmatrix} = \begin{pmatrix} S_{11} & S_{12} \\ S_21 & S_{22} \end{pmatrix} \begin{pmatrix} a_1 \\ a_2 \end{pmatrix}, \tag{2.1}$$

where $S_{11}$ and $S_{22}$ are defined as reflection coefficients at ports 1 and 2, respectively, while $S_{21}$ and $S_{12}$ correspond to the transmission from port 1 to port 2 and vice versa. The conditions $S_{21} = S_{12}$ identify a network with two ports that is *reciprocal*, and if the input and output impedance are the same, we speak of a two-port network that is *symmetric* $S_{11} = S_{22}$ [65].

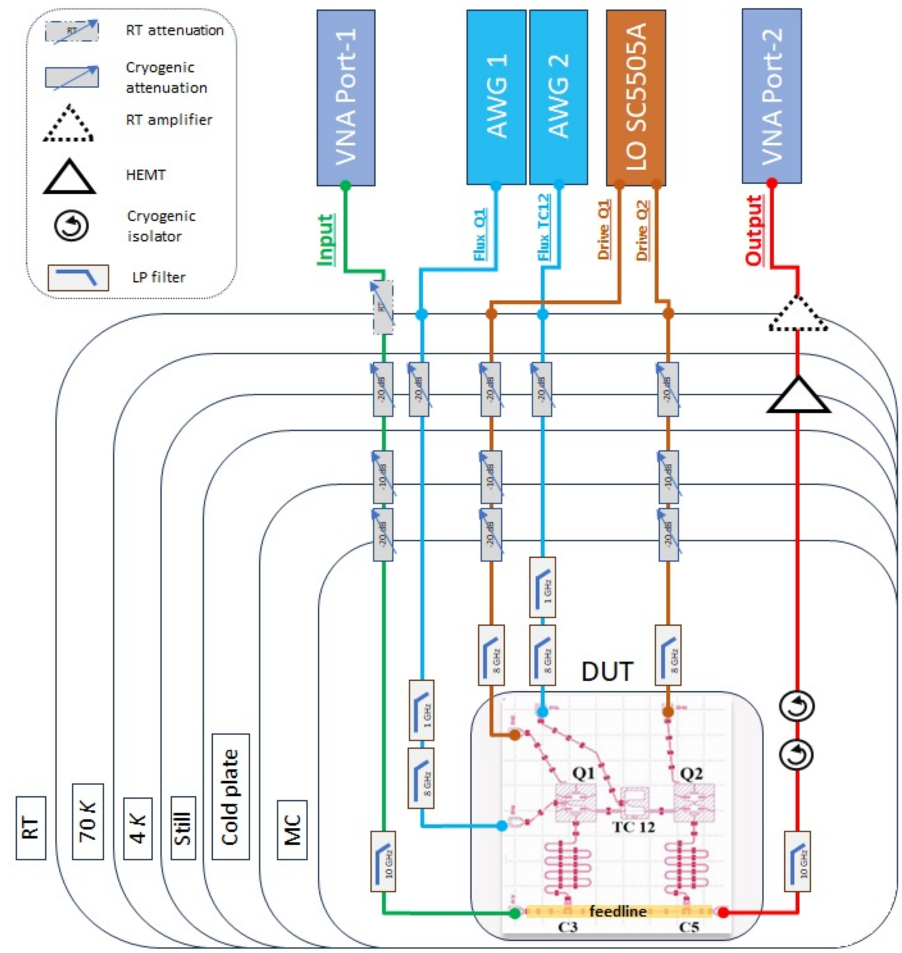


Figure 2.8: Schematic for the experimental set-up for spectroscopic measurements. In a resonator spectroscopy measurement, only the VNA signal-source (port-1) is employed. In the qubit spectroscopy, we use also an AWG (slot 3 and 4, see Fig. 2.6b) as a DC source for flux bias and the LO (slot 7) as drive signal source (Sec. 1.3.1). The Device Under Test (DUT), anchored at the MC, shows the detail of the pair Q1 and Q2 of the *Soprano_Tunc*, as an example. We stress though that the measurement setup is totally analogous to the Soprano chip.

The VNA provides fast and reliable information about the samples allowing the study of the components both in transmission and reflection. In a typical setup for the **resonator spectroscopy** measurement, a transmission experiment is performed, where an RF signal is sent through port 1 to the input line of the sample feedline. In this kind of measurement, the input signal is a continuous excitation of the resonator, commonly referred to as *continuous wave measurement*. The output signal is then recorded by port-2 as a complex EM signal, and the VNA can measure both the real and the imaginary parts in the form of a magnitude (in dBm) and a phase [66]. From them, we can extract the readout resonator characteristics such as resonance frequency, dispersive shift, and quality factors. Similarly, **qubit spectroscopy** can be performed by using continuous wave readout signals in a frequency range of a few kHz around the readout frequency in the dispersive regime. A typical spectroscopy setup is shown in Fig. 2.8. In a qubit spectroscopy, a continuous wave signal is added on the dedicated drive line, by employing a Local Oscillator (LO) see Fig. 2.6b. This setup allows us to obtain the transition frequencies of the qubit (such as $|0\rangle \rightarrow |1\rangle$, $|0\rangle \rightarrow |2\rangle$), ..). Additionally, the use of a waveform generator (AWG), also allows to bias the dedicated flux line to perform measurements of the frequency tunability. Continuous wave measurements are finally acquired through the *QCodes* Python environment [67], which allows to connect with each instrument, develop experiment routines, store the data and show the outcome of the experiments.

## 2.5 Time-domain measurements

For the study of computational operations, it is necessary to move in time-domain, i.e., from continuous-wave (CW) signals to pulsed tones. Fig. 2.9 shows an experimental scheme for time-domain characterization, which includes: Arbitrary Waveform Generators (*AWGs*), *LOs*, *IQ* and three-ports mixers, and an analog to digital converter, namely the *Digitizer*. The AWG can generate pulsed waves but is limited in the frequency band up to 400 MHz [58]. For higher frequencies, alternatives include employing AWGs operating in the GHz range. However, their use is restrained by the associated costs and the noise they generate in this frequency regime. An alternative approach involves the *UP conversion* process, which combines the shape generated by the AWG with a pure tone at high frequency (GHz), called carrier wave, generated by an LO. In this setup is employed an *IQ mixer* which behaves like a multiplier of signals in the time domain [68]. As shown in Figure 2.9, the carrier tone from the LO is combined with the *in-phase* (I) and *quadrature-phase* (Q) components of the *intermediate frequency* (IF) signal $\omega_{AWG-IF}$. The mixing between the AWG and the LO produces two separate RF frequencies:

$$\omega_{RF} = \omega_{AWG-IF} \pm \omega_{LO}, \tag{2.2}$$

where one of the two sidebands can be suppressed with an appropriate calibration using single sideband modulation [68]. As shown in Fig. 2.9, in this setup the up-conversion is carried out both for the drive signal, with frequency $\omega_D$, on the dedicated drive line (brown), and for the readout signal, with frequency $\omega_{RO}$, on the input feedline port (green).

What changes is the choice of the proper LO, see Fig. 2.6b. For the RO it is necessary to operate within the 6-8 GHz band range, therefore we use an RF generator with a maximum output frequency of 20 GHz. For the drive, we are limited to a frequency range from 4 to 6 GHz, hence we use a LO with a maximum output frequency of 6 GHz.

Finally, the acquisition of the output signal by the *digitizer*, see Fig. 2.6b, requires demodulation and *down*-conversion. Using a 3-port mixer, the output signal and the same LO of the input signal are combined and down-converted to the following frequency:

$$\omega_{IF} = |\omega_{out} \mp \omega_{LO-RO}|. \tag{2.3}$$

This down-converted signal is then acquired by the digitizer for a time $t_{acq} = \frac{N_m}{\nu_s}$, where $N_m$ is the number of samples and $\nu_s$ is the digitizer sampling rate, i.e. 500 $MSample/s$. The choice of the acquisition time requires a balance between the need for a sufficient number of samples during the RO pulse and the requirement to remain within the duration of the RO pulse signal. This is to avoid bad triggering and asynchronous acquisitions while acquiring enough data points [66]. After the acquisition of time-domain signals, a Fast Fourier Transform (FFT) is applied by the digitizer's demodulator. The Labber environment incorporates a specialized software component known as the *Multi-qubit Pulse Generator* [62], which enables the extraction of the magnitude and phase (or real and imaginary components) of the RO signal. The results of these measurements are ultimately stored and graphically accessed through dedicated software within the Labber framework [62].

## 2.6 Protocols for single-qubit characterization

Before employing a circuit quantum electrodynamics (cQED) device as a quantum processor, is essential to characterize the system through specific measurement protocols. For clarity, Fig. 2.10 shows a dependency scheme, highlighting the main parameters and their interrelationships during the characterization experiments. In this section, we will specifically focus on the aspects of *spectroscopy* and *qubit coherence*. We initiate our discussion by outlining the procedure for a flux-tunable transmon coupled to a readout resonator.

### 2.6.1 Spectroscopy experiments

The first step in characterizing a device is usually a spectroscopy experiment. Spectroscopy refers to the measurement of intensity as a function of frequency and it is used to determine resonance frequencies of resonators and qubits.

Let us consider, as in this thesis work, the case of $\lambda/4$ CPW resonators capacitively coupled to a common microwave feedline. The initial step in the characterization process involves **resonator-readout (RR) spectroscopy** to detect the presence of RR cavity and identify their frequencies. This type of measurement is performed using single-tone spectroscopy (Sec. 2.4). The transmitted measurement data $S_{21}$ enable the extraction of

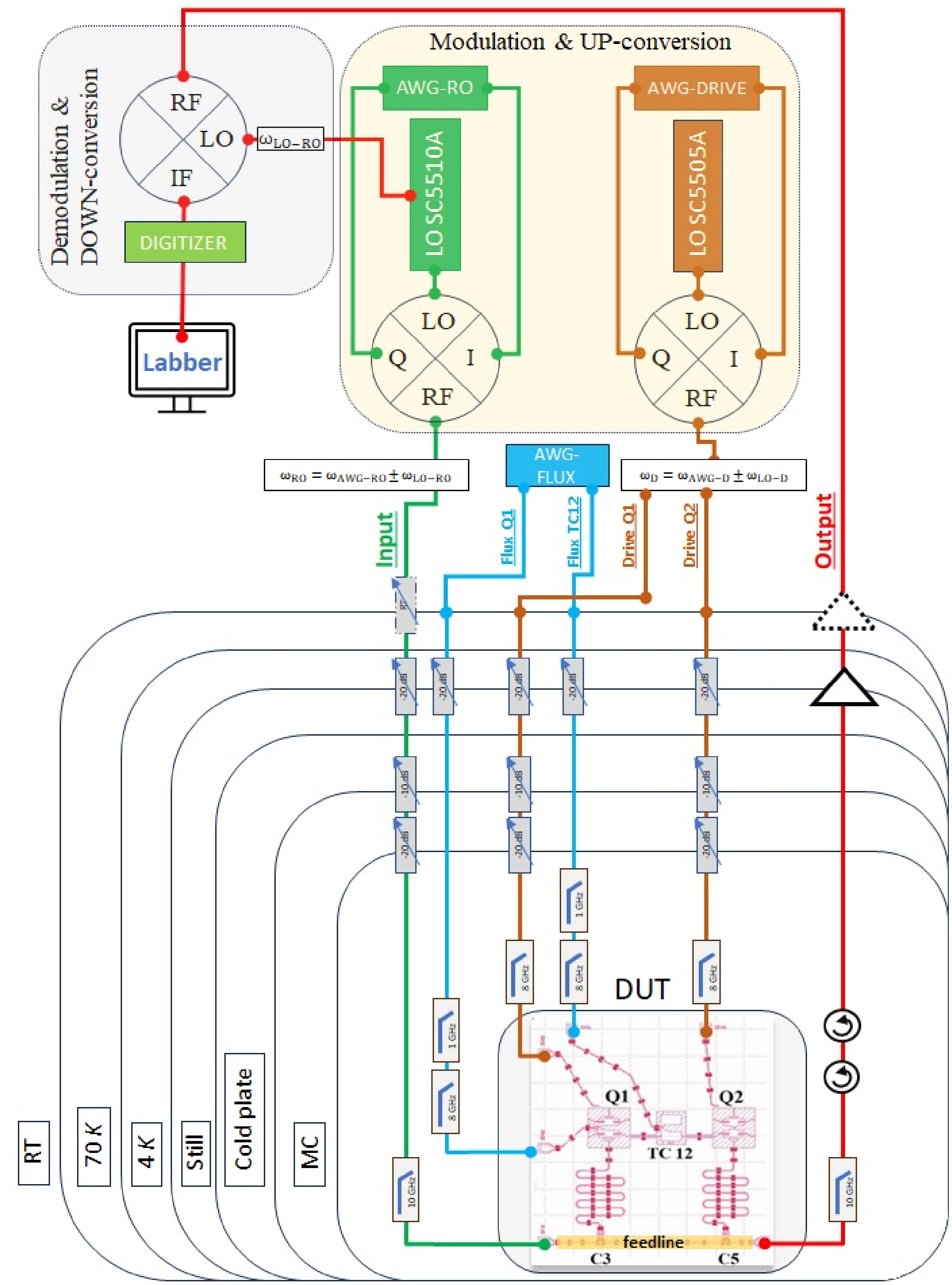


Figure 2.9: Summary diagram of the experimental setup for time-domain measurements. The input signals of the drive (brown) and RO (green) are up-converted, while the output signal of RO (red) is down-converted. To perform single and multi-qubit measurements in the time-domain, modulations in flux are employed by sending pulsed waveforms generated from the AWG through the dedicated flux lines (blue).

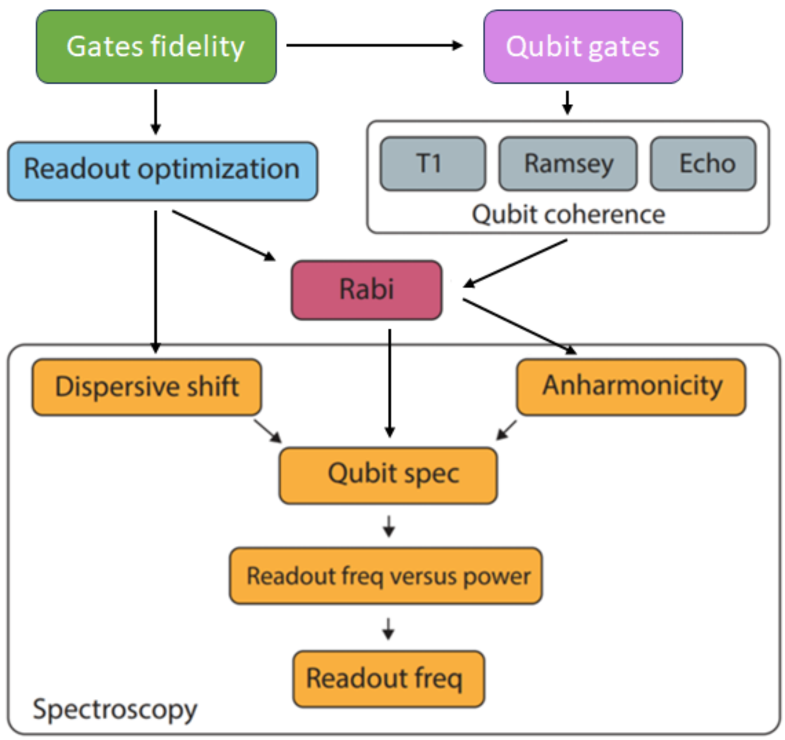


Figure 2.10: Dependency graph for the typical experiments on superconducting qubits. The arrows represent dependency relationships between the different types of measurements, progressing from the readout frequency at the starting point to the gate fidelity at the endpoint. Figure adapted from [69].

information about both the amplitude and phase of the signal. The measured $S_{21}$ of each resonator in response to a readout tone at $\omega$ is described by a Lorentzian line shape, which can be written as [70]:

$$S_{21} = A\left[1 + \alpha\frac{\omega - \omega_r}{\omega_r}\right]\left[1 - \frac{\frac{|\kappa_c|}{\kappa}}{1 + 2i\frac{\omega-\omega_r}{\kappa}}\right]e^{i(\tau_v\omega+\phi_0)}, \tag{2.4}$$

where A represents the transmission amplitude away from resonance and $\omega_r$ is the qubit state-dependent resonance frequency of the cavity introduced in Sec. 1.4.1. The parameter $\alpha$ is indicative of how much the amplitude varies as a function of the detuning from the resonant frequency $\omega_r$, and $\tau_v$ and $\phi_0$ are related to propagation delays to and from the sample. Finally, $\kappa$ is the total linewidth (full width at half maximum) of the resonance. It encompasses both the external coupling rate $\kappa_c$ and the internal loss rate $\kappa_i$, such that $\kappa = \kappa_c + \kappa_i$. Here $\kappa_c$ is related to how strongly the resonator is coupled to the external readout or transmission line. The internal loss rate $\kappa_i$ is determined by the material quality and device layout.

In cQED systems, understanding each of these parameters is crucial for various tasks: from the basic characterization of the resonator to more advanced operations like the readout of qubits. They help describe not just the ideal resonator behavior, but also any deviations from this ideal case due to real-world imperfections and complexities [69].

Typically, initial spectroscopy experiments are conducted in the high-power regime to enhance the *signal-to-noise ratio* (SNR). Operating at high power means that the system is outside the few-photon limit and, consequently, beyond the dispersive regime. In this context, we identify the *bare frequency* of the reading mode, as discussed in Sec. 1.4.1. By performing spectroscopy at varying power levels, shown in Fig.2.11a, we can determine the *dressed frequency* of the resonator, as defined by Eq. 1.47.

The power sweep experiment serves as a prerequisite for following characterizations, (Fig. 2.10). It tells us whether the qubit is dispersively coupled to the resonator. Moreover, this experiment enables the **readout optimization** of the power settings required for all following measurements, ensuring that the signal remains sufficiently strong while avoiding nonlinear distortions or broadening of the resonator response [71].

In the case of flux-tunable qubits, another valuable experiment involves conducting resonator spectroscopy in the low-power regime while varying the current applied to the flux-bias line of the coupled qubit. From Eq. 1.42 and Eq. 1.47 we expect that the resonator, when dispersively coupled to the flux-tunable qubit, will vary its frequency according to:

$$\omega_R\left(\Phi_{ext}\right) = \omega_R + \frac{g^2}{|\omega_q\left(\Phi_{ext}\right) - \omega_R|}. \tag{2.5}$$

This measurement offers dual advantages: it estimates both the dispersive shift and the coupling strength $g$, while identifying the flux point where $\omega_r$ reaches its maximum value, corresponding to the *sweet spot* of the qubit, see Sec. 1.2.3.

The technique for measuring the resonance frequency of the qubit is a protocol based on two-tone continuous wave spectroscopy, also called **qubit spectroscopy**. In this

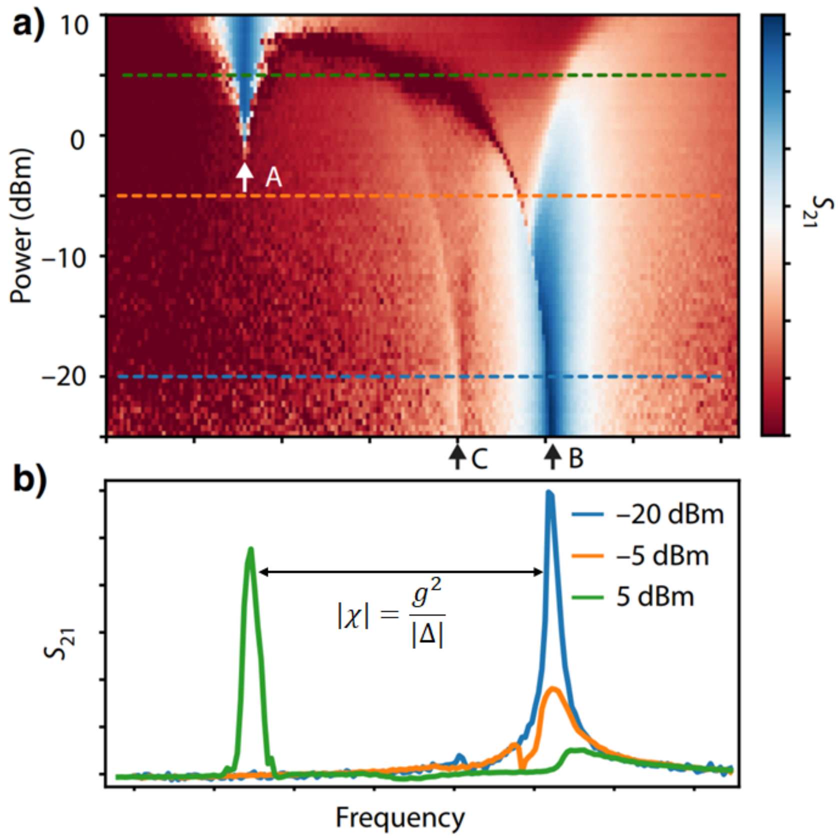


Figure 2.11: Example of a **Power Sweep Spectroscopy Experiment**. In **a)**, the resonator-readout (RR) spectroscopy measurements is shown, and repeated for different power levels of the readout tone signal. At high power levels, a high-power transmission peak (A) becomes apparent. Upon reducing the power, both the qubit and the cavity enter the dispersive regime, as discussed in Section 1.4.1. A low-power peak then emerges at a different frequency due to the *dispersive shift*, $\chi$, which typically occurs in the range of a few megahertz. A third peak (C) illustrates the impact of some residual thermal population. In **b)**, cut plots are displayed at three distinct power levels. These plots reveal the typical behavior of cavity transmission versus frequency under varying power conditions. Figure adapted from [69].

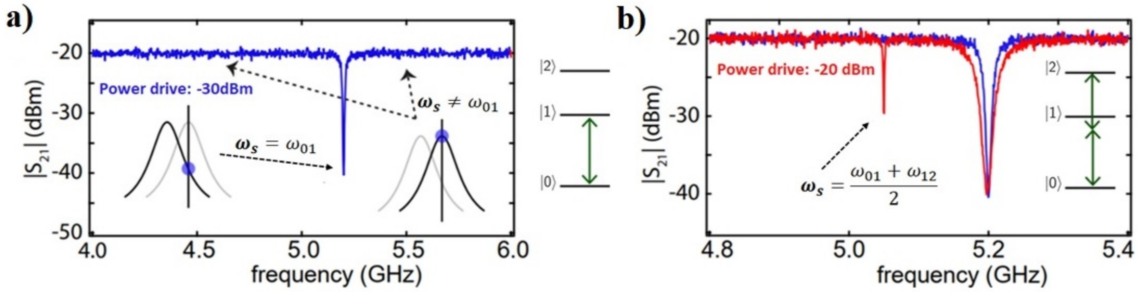


Figure 2.12: In **a)** is shown the **qubit spectroscopy measurement** at low power drive. The background of the output signal under off-resonance conditions, $\omega_s \neq \omega_{01}$, corresponds to the dispersive state of the resonator. However, when the drive tone is on-resonance with the qubit, a notable peak arises, marking the transition frequency $\omega_{01}$ of the qubit. **b)** Increasing the power of the drive also the transition $|0\rangle \to |2\rangle$ occurs. Figures adapted from [4].

methodology a constant microwave tone is applied at dressed frequency $\omega_r$ to resonate with the RR, while a second drive tone $\omega_s$ is employed to probe the state of the qubit. The latter can be either sent through the feedline or the dedicated qubit drive line. As shown in Fig. 2.12a, when the drive tone approximates the qubit's resonance frequency ($\omega_s \approx \omega_q = \omega_{01}$), the frequency of the resonator changes due to the dispersive coupling, see Eq. 1.47 and Fig. 2.12a.

The qubit spectroscopy measurement is highly dependent on the power level of the drive tone applied to the qubit. If the power is too low, the qubit won't be excited, even when the drive frequency is near its resonance, resulting in no observable changes. Conversely, applying excessive power will broaden the resonance line, making the peak indistinguishable from the background noise. Since the strength of the coupling between the qubit and the drive line is not known prior to characterization, a practical approach involves iteratively performing the spectroscopy at various power levels until the resonance is identifiable. We can confirm that it is indeed the qubit mode of interest by verifying the flux dependence of its resonance frequency [69].

Performing a power sweep also reveals a second dip at a slightly lower frequency. This dip corresponds to the process by which two photons of drive excited the qubit from the ground state to the second excited state, $|0\rangle \to |2\rangle$, as depicted in Fig. 2.12b. The location of this second transition indicates the anharmonicity of the transmon, see Eq. 1.18, which can be an important consideration for the design and calibration of subsequent single-qubit operations [69].

### 2.6.2 Time-domain protocols

Once we measure the qubit frequency from spectroscopy, the first experiment in the time domain is to the **Rabi oscillation**, since this experiment doesn't require any pulse calibration. It consists of applying a resonant microwave qubit-drive (QD) pulse to the qubit. In the rotating frame, which rotates at the microwave frequency around the Z axis, such a pulse is equivalent to a static magnetic field lying in the x-y plane, as discussed

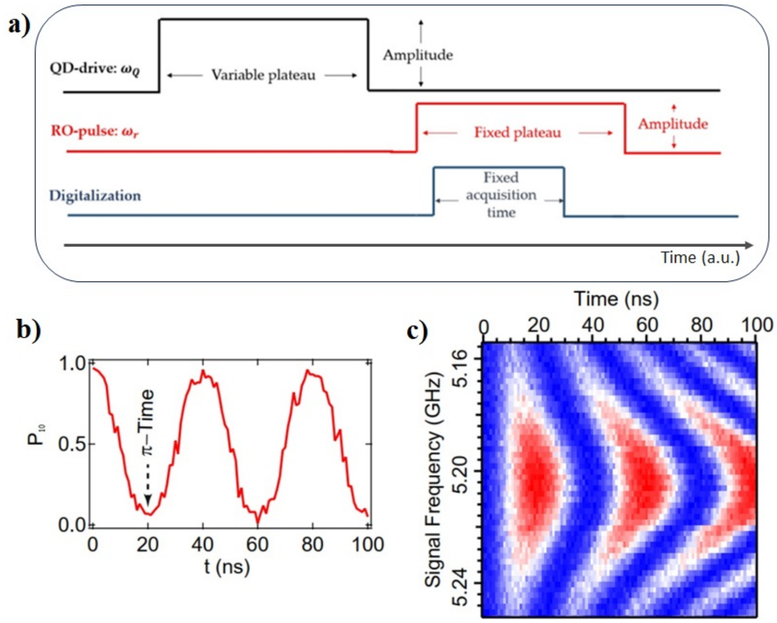


Figure 2.13: **a)** Schematic of the protocol sequence for the Rabi oscillation measurement in the time-domain. **b)** Rabi oscillation experiment, where is depicted the $\pi$ duration to take qubit state from $|1\rangle$ to $|0\rangle$. **c)** Rabi oscillation measurement, repeated for different drive signal frequencies, consisting in a *chevron plot*. Figure adapted from [4].

in Sec. 1.3.1. The probability of being in state $|1\rangle$ oscillates with the pulse duration, producing the Rabi oscillation [72] as depicted in Fig. 2.13a. Thus, it becomes possible to determine the $\pi$-pulse, i.e. the duration of the QD pulse necessary to take the qubit from its fundamental state to the excited state [66]. After each QD pulse, the RO sequence starts and the readout signal is acquired via the digitizer.

As discussed in Sec. 2.5, in the *time-domain measurements* the setup allows the control of the I-Q components of the drive signal (Eq. 1.36). In order to calibrate the $\pi$-pulse, we first need to make sure that the qubit frequency is accurate and oscillations are on-resonance with the qubit [4]. One way to check this is to sweep the drive frequency while performing Rabi oscillation measurements. The resulting 3D color plot is called *chevron plot*, see Fig. 2.13b.

As discussed in Sec.1.2.4, the coupling with the environment produces effects of decoherence and dephasing. After tuning up a $\pi$ pulse using Rabi oscillations, we need to determine the coherence properties of the qubit, namely, the *relaxation time* $T_1$, the *Ramsey time* $T_2^*$, and the *echo dephasing time* $T_2^{echo}$.

The first step is the initialization of the qubit in the ground state. Since the lifetime of the system is typically for this design of the order of tens of microseconds, all we need to do is leave the qubit for some amount of time (about 100 microseconds) to make sure it is in the ground state [4].

To measure the **relaxation time**, the qubit is excited to $|1\rangle$ with a $\pi$-pulse calibrated with the Rabi oscillations measurement. This is then followed by a variable delay time

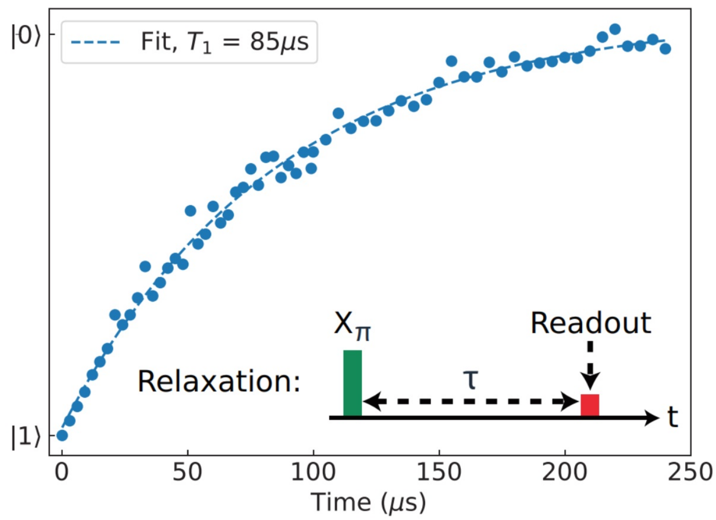


Figure 2.14: Data plot for the energy relaxation measurement from [14]. The qubit is prepared in the excited state using a $\pi$-pulse and measured after a waiting time $\tau$. For each value $\tau$, this procedure is repeated and an exponential decay emerges. Employing Eq. 2.6, data fit yields a characteristic time $T_1$ = 85 $\mu s$.

$\tau$, called *sequence duration*. The RO resonator response is first read immediately as the qubit has rotated in the excited state, and then the measurement is repeated changing the sequence duration. As shown in Fig. 2.14, this results in an exponentially decaying signal, given by:

$$S(t) = Ae^{-t/T_1} + B, \tag{2.6}$$

where S(t) is the readout signal as a function of wait time t, and A and B are scaling and offset factors, respectively [69].

The **Ramsey Decoherence time** $T_2^*$ can be obtained by initializing the qubit in $\frac{1}{\sqrt{2}}(|0\rangle + |1\rangle)$, applying a $\pi/2$ pulse, then we wait a certain delay time before another $\pi/2$ pulse is used to bring the qubit to the excited state. The RO is performed soon after the last $\pi/2$-pulse. The Ramsey experiment will produce a decaying oscillation described by [69]:

$$S(t) = Ae^{-t/T_2^*} \cos(2\pi\delta\omega t + C) + B, \tag{2.7}$$

where A, B, and C are scaling, offset factors, and an additional phase, respectively, and $\delta\omega = \omega_q - \omega_d$ is the detuning between the qubit frequency and the QD frequency. These oscillations reduce to a pure exponential decay if the QD frequency is on resonance with the qubit frequency [66]. When $\delta\omega \neq 0$, we are off-resonance and we expect the system to behave as a damped oscillator [14]. The period of these oscillations corresponds to the detuning $\delta\omega$ and the damping provides an estimate of $T_2^*$ (Fig. 2.15).

In general, a $T_1$ measurement is related to all the loss channels in the system, and provides an indication of the internal quality factors of the device. The Ramsey time contains information on both energy relaxation and pure dephasing ($T_\phi$) in the qubit, i.e., $1/T_2^* = 1/(2T1) + 1/T_\phi$, which quantifies effective qubit decoherence time scales [69].

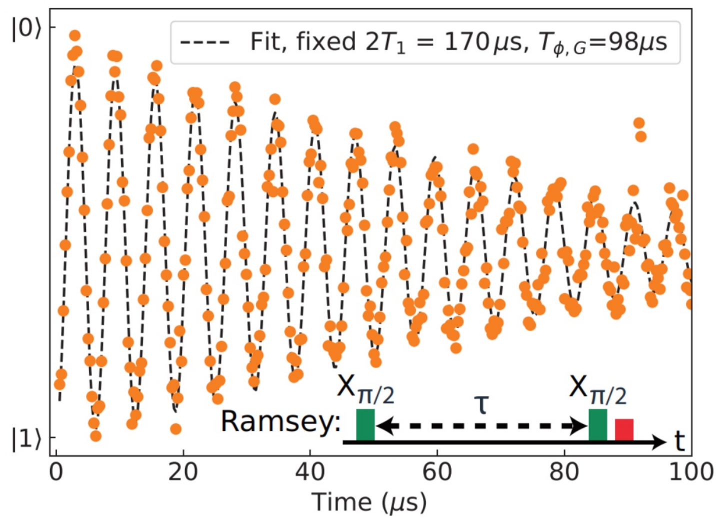


Figure 2.15: *Ramsey measurement.* The qubit is prepared on the equator using an $\frac{\pi}{2}$-pulse, intentionally detuned from the qubit frequency by $\delta\omega$. As a result, the Bloch vector precess around the $z$-axis at the rate of $\delta\omega$ in the rotating frame. After waiting for a time $\tau$, another $\frac{\pi}{2}$-pulse is applied, which brings the Bloch vector back to the $z$-axis. This effectively translates its prior equatorial position to a new position along the $z$-axis. Figure from [14].

The **Hahn-Echo decoherence time** $T_2^{echo}$ can be measured by adding a single $\pi$-pulse in the middle of a Ramsey experiment. The $\pi$-pulse in the middle is also known as *refocusing pulse*, and allows to perform a rotation of $\pi$ around the z-axis of the Bloch sphere, after the qubit preparation in the equatorial plane. This protocol is also called *Hahn echo*. As shown in Fig. 2.16, the resulting dynamics follows an exponential decay given by [69]:

$$S(t) = Ae^{-t/T_2^{ECHO}} + B. \tag{2.8}$$

The refocus pulse allows to cancel low-frequency dephasing effects. Therefore, the coherence time measured with Hahn-Echo protocol is longer that that measured through Ramsey interferometry [14].

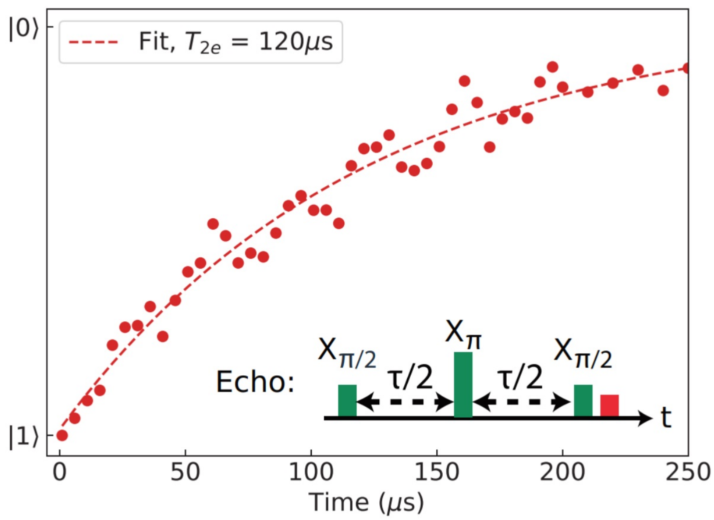


Figure 2.16: *Hahn echo experiment* for measuring transverse relaxation or decoherence: the qubit is initialized and assessed similarly to the Ramsey interferometry test. The key distinction is the inclusion of a single $\pi$ pulse at the midpoint of the free-evolution time $\tau$. The resulting decay pattern is approximately exponential, see Eq. 2.8, characterized by a time $T_2^{echo} = 120\,\mu s$.

# –3–
# Introduction to two-qubit coupling schemes



Qubit coupling is a fundamental aspect of quantum computer architectures [73]. Beyond the readout and control conditions discussed in previous sections, an understanding of coupling mechanisms is essential for the implementation of two-qubit gates. Indeed, a pivotal challenge in the advancement of large-scale quantum computing is the extensible implementation of high-fidelity entangling gates [7]. Over the past two decades, superconducting qubits have undergone substantial developments in gate fidelities and scalability, marking the era of *noisy intermediate-scale quantum* (NISQ) systems [74]. Despite these significant advancements, the two-qubit gate error still remains a major bottleneck for realizing the full potential of NISQ hardware capabilities.

In this chapter, we explore the coupling mechanisms between two superconducting

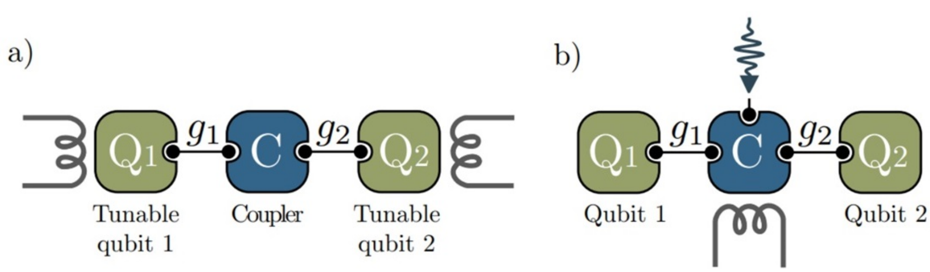


Figure 3.1: Schematics of different coupling techniques. The exchange interaction between adjacent qubits can be realized through auxiliary elements, such as a bus resonator **a)**. The qubits are detuned into or out of resonance to either activate or deactivate the inter-qubit interaction, respectively. **b)** Parametric geometries are implemented by modulating a variable tunable coupler system parameter. Figure from [34]

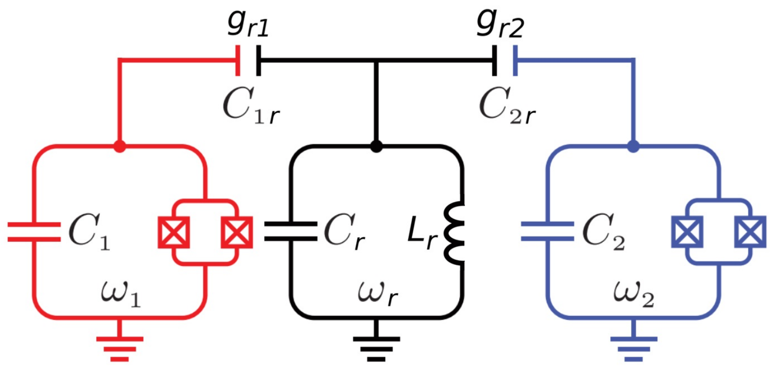


Figure 3.2: Circuit diagram of two split-transmon qubits capacitive coupling via a coupler in the form of a linear resonator.

qubits and their representation in the qubit eigenbasis [14]. Physically, either capacitive or inductive couplings can accomplish this, but in this work, we only pay attention to capacitive couplings. Capacitive coupling with superconducting qubits has been seen to offer advantages in terms of preserving coherence times and is compatible with 3D integration [7, 75].

One of the key challenges in realizing two-qubit gates is the rapid modulation of interactions. While for single-qubit gates this is done by simply turning on and off a microwave drive, two-qubit gates require turning on a coherent qubit-qubit interaction for a fixed time [34]. Achieving high on/off ratios presents a significant challenge in this context [34]. In this thesis, we have studied two designs that facilitate non-direct qubit-qubit coupling through the use of a fixed coupler (see Fig. 3.1a) and a tunable coupler (see Fig. 3.1b).

As follows, we will first dive into the formal representation of the interaction mechanisms in these two circuital designs. After that, we will discuss how it is possible to implement, in both configurations, one of the most common two-qubit gates in superconducting devices: the i-SWAP gate. Finally, we discuss the main advantages and disadvantages of the two configurations.

## 3.1 Two-qubits coupled by a fixed resonator

As discussed in Sec. 1.4.1, generating entanglement between individual quantum systems requires the engineering of an interaction Hamiltonian that links the degrees of freedom within those systems [14]. A resonator can be used to mediate coupling between two or more qubits. An example is provided in Fig. 3.2a, where two *split-transmon* qubits are capacitively coupled to a central resonator. The Hamiltonian for this system is given by [14][34]:

$$H = \sum_{i=1,2} \left( \omega_i b_i^\dagger b_i - \frac{E_{C_i}}{2} b_i^\dagger b_i^\dagger b_i b_i \right) + \omega_r a_r^\dagger a_r + g_{1r} \left( b_1^\dagger a_r + b_1 a_r^\dagger \right) + g_{2r} \left( b_2^\dagger a_r + b_2 a_r^\dagger \right). \quad (3.1)$$

Here we identify two transmon qubits interacting with a resonator mode, each with distinct interaction strengths $g_{1r}$ and $g_{2r}$.

As in the case of the Soprano device (Sec. 2.3), the coupler is a high-frequency resonator bus, and it is reasonable to assume that the resonator mode is only virtually populated [76]. This is achieved by operating in the dispersive regime [14], where both qubits are substantially detuned from the resonator, i.e. $|\Delta_i| = |\omega_i - \omega_r| \gg g_{ir}$, i=1, 2. Under these conditions, it can be demonstrated that an effective qubit-qubit interaction manifests, as detailed in Ref. [34]:

$$H = \sum_{i=1,2} \left( \tilde{\omega}_i b_i^\dagger b_i - \frac{E_{C_i}}{2} b_i^\dagger b_i^\dagger b_i b_i \right) + \tilde{\omega}_r a_r^\dagger a_r + J \left( b_1^\dagger b_2 + b_1 b_2^\dagger \right). \tag{3.2}$$

The first term in the equation represents the transmon Hamiltonian with Lamb-shifted transition frequencies $\tilde{\omega}_i = \omega_i + g_{ir}^2/\Delta_i$. The second term includes the Lamb shift affecting the resonator mode, denoted as $\tilde{\omega}_r = \omega_r + g_{1r}^2/\Delta_1 + g_{2r}^2/\Delta_2$. The third term gives the effective qubit-qubit interaction, commonly referred to as *J-coupling* or *transverse* exchange coupling [34] [76]:

$$J = \frac{g_1 g_2}{2} \left( \frac{1}{\Delta_1} + \frac{1}{\Delta_2} \right). \tag{3.3}$$

When both qubits are resonant with each other, the resonator becomes virtually populated due to its dispersive interaction with the qubits, thereby serving as a quantum bus that mediates interactions between them. In the frequency domain, an *avoided level crossing* with a gap of magnitude $2J = 2g_1 g_2/\Delta$ is observed when the excited *bare* states $|01\rangle$ and $|10\rangle$ are *dressed* due to the effective qubit-qubit interaction, as shown in Fig. 3.3.

## 3.2 Two-qubits coupled by a tunable coupler

One of the crucial challenges in quantum computation lies in constructing a large-scale network of highly coherent, interconnected qubits [77]. As a consequence, research on novel coupling mechanisms has become indispensable for enhancing gate operation fidelity and scalability of quantum computers. Particularly, coupling mechanisms that enable high-coherence qubits with tunable inter-qubit coupling has emerged as a critical architectural challenge. This allows for both coherent local operations and dynamically adjustable qubit interactions [77].

In this section, we introduce an alternative coupling scheme that diverges from the conventional resonator cavity approach. Here, the interaction occurs via a third qubit serving as a coupler. This kind of coupling is implemented in the prototypal Soprano_TunC (Sec. 2.3). The main feature of this design is the ability to modulate the coupler frequency to control the qubit-qubit coupling strength. This approach was initially proposed by Yan et al. in 2018 [7] and is an ideal solution for mitigating always-on qubit-qubit coupling during idle periods between entangling gate operations [9].

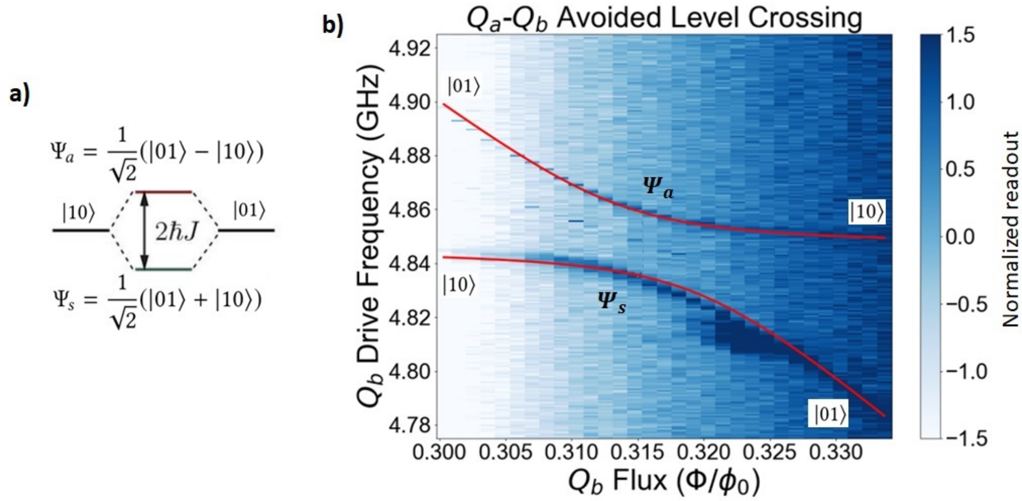


Figure 3.3: **a)** Energy level diagram of the two coupled qubits, featuring both bare states ($|01\rangle$, $|10\rangle$) and dressed states ($\Psi_s = \frac{1}{\sqrt{2}}(|01\rangle + |10\rangle)$), $\Psi_a = \frac{1}{\sqrt{2}}(|01\rangle - |10\rangle)$) arising from interactions. **b)** The spectroscopic measurement of the avoided level crossing as a function of normalized flux $\Phi/\Phi_0$ threading through the loop of the qubit $Q_b$, while the qubit $Q_a$ is maintained at a fixed frequency. The solid red lines represent energy levels derived from the diagonalization of the two-qubit Jaynes-Cummings Hamiltonian. Figure adapted from [55].

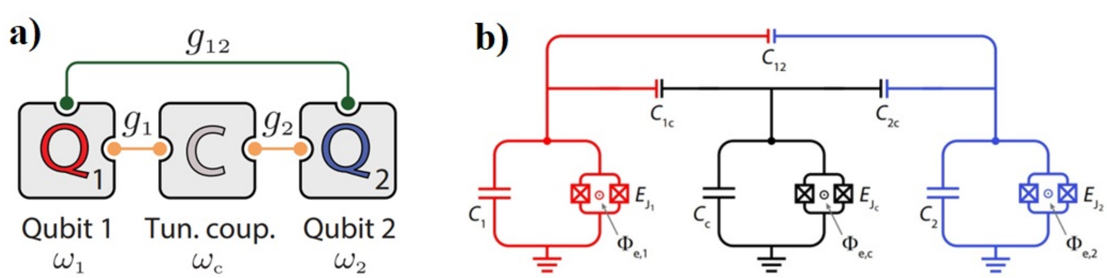


Figure 3.4: **a)** Sketch of a generic three-body system arranged in a chain geometry. Each of the two qubit modes ($\omega_1$ and $\omega_2$) couples to the central mode of the tunable coupler ($\omega_c$) with a coupling strength $g_j$ (j = 1, 2), and they also couple to each other with a coupling strength $g_{12}$. **b)** Circuit schematic featuring two split-transmon qubits, with the tunable coupler between them. Figures adapted from [7].

Conceptually, this system can be viewed as a chain of three modes featuring exchange coupling between nearest neighbors (N.N.) and next-nearest neighbors (N.N.N.), as shown in Fig. 3.4a. The qubits with frequencies $\omega_1$ and $\omega_2$ are coupled to a central tunable coupler with frequency $\omega_c$ with a coupling strength $g_j$ (where $j = 1, 2$), and they also couple to each other with a coupling strength $g_{12}$. Generally, the N.N. coupling is stronger than the N.N.N. coupling, $g_j > g_{12} > 0$, where $j \in \{1, 2\}$.

In terms of circuit implementation, this design may feature two split-transmon qubits capacitively coupled to each other via $C_{12}$, and to a central split-transmon via $C_{1c}$ and $C_{2c}$, as depicted in Fig. 3.4b. Upon canonical quantization and under the assumption of a transmon regime $E_{J_i} \gg E_{C_i}$, the system can be modeled as a set of three coupled Duffing oscillators, as detailed in Ref. [7]:

$$\begin{aligned}\hat{H} = &\sum_{i=1,2,c} \omega_i \hat{b}_i^\dagger \hat{b}_i - \frac{E_{C_i}}{2} \hat{b}_i^\dagger \hat{b}_i^\dagger \hat{b}_i \hat{b}_i \\ &+ \sum_{j=1,2} g_j (\hat{b}_j^\dagger \hat{b}_c + \hat{b}_j \hat{b}_c^\dagger - \hat{b}_j^\dagger \hat{b}_c^\dagger - \hat{b}_j \hat{b}_c) \\ &+ g_{12} (\hat{b}_1^\dagger \hat{b}_2 + \hat{b}_1 \hat{b}_2^\dagger - \hat{b}_1 \hat{b}_2 - \hat{b}_1^\dagger \hat{b}_2^\dagger)\end{aligned} \tag{3.4}$$

The creation and annihilation operators for the corresponding modes are denoted by $\hat{b}_i^\dagger$ and $\hat{b}_i$, respectively. The frequency of each split-transmon, $\omega_i$, is governed by the term reported in the first line of the formula 1.42, as discussed in Sec. 1.3.2. The terms reported in the second and third line of formula 3.4, provide the *qubit-coupler* and *qubit-qubit* interactions, respectively, with their strengths defined as follows:

$$g_j = \frac{1}{2} \frac{C_{jc}}{\sqrt{C_j C_c}} \sqrt{\omega_j \omega_c}, \tag{3.5}$$

$$g_{12} = \frac{1}{2} (1 + \eta) \frac{C_{12}}{\sqrt{C_1 C_2}} \sqrt{\omega_1 \omega_2}, \tag{3.6}$$

and $\eta = \frac{C_{1C} C_{2C}}{C_{12} C_C}$. The exchange interaction between modes is similar to the Jaynes-Cummings interaction discussed in Sec. 1.4. However, counter-rotating terms are retained. These terms gain significance when the coupler frequency substantially exceeds the qubit frequency, entering a *strong dispersive regime* [7].

The Hamiltonian is diagonalized through the application of a second-order Schrieffer-Wolff transformation, as detailed in Refs. [7] and [9]:

$$\tilde{H} = \sum_{i=1,2,c} \tilde{\omega}_i \hat{b}_i^\dagger \hat{b}_i - \frac{E_{C_i}}{2} \hat{b}_i^\dagger \hat{b}_i^\dagger \hat{b}_i \hat{b}_i + \tilde{g} (\hat{b}_1^\dagger \hat{b}_2 - \hat{b}_1 \hat{b}_2^\dagger). \tag{3.7}$$

The dressed eigenfrequencies of the qubits and the coupler are given by:

$$\tilde{\omega}_{1,2} = \omega_{1,2} + \frac{g_{1,2}^2}{\Delta_{1,2}} - \frac{g_{1,2}^2}{\Sigma_{1,2}}, \tag{3.8}$$

$$\tilde{\omega}_c = \omega_c - g_1^2 \left( \frac{1}{\Delta_1} + \frac{1}{\Sigma_1} \right) - g_2^2 \left( \frac{1}{\Delta_2} + \frac{1}{\Sigma_2} \right), \tag{3.9}$$

where we introduce the detuning $\Delta_j = \omega_j - \omega_c$. The term $\Sigma_j = \omega_j + \omega_c$ is associated with the counter-rotating ($CRW$) terms, which become significant in the strong dispersive regime, i.e., when $\omega_c \gg \omega_j$, where $|\Delta_j| \simeq |\Sigma_i|$. The two computational qubits interact through an effective interaction, with strength $\tilde{g}$ [7] [9]:

$$\tilde{g} = \frac{1}{2} \left[ \frac{\omega_c}{2\Delta}\eta - \frac{\omega_c}{2\Sigma}\eta + \eta + 1 \right] \frac{C_{12}}{\sqrt{C_1 C_2}} \sqrt{\omega_1 \omega_2}, \tag{3.10}$$

with $\frac{1}{\Delta} = \frac{1}{2}(\frac{1}{\Delta_1} + \frac{1}{\Delta_2})$ and $\frac{1}{\Sigma} = \frac{1}{2}(\frac{1}{\Sigma_1} + \frac{1}{\Sigma_2})$. Eq. 3.10 identifies four interaction mechanisms respectively [7] (labelling the bare eigenstates of Hamiltonian 3.4 as $|Qubit1, Coupler, Qubit2\rangle$):

1. the virtual exchange interaction via the state $|010\rangle$;
2. the virtual exchange interaction via the state $|111\rangle$;
3. the capacitive coupling via the intermediate capacitance network (direct qubit-qubit coupling, indirect connection);
4. the direct capacitive coupling (direct qubit-qubit coupling, direct capacitive connection).

The first two processes occur via the coupler, representing indirect coupling facilitated by the virtual excitation of the coupler, while the last two do not depend on $\omega_c$, and are respectively related to the indirect capacitive couplings through $C_{1C}$ and $C_{2C}$, and the direct capacitive coupling through $C_{12}$. Typically, the N.N.N. capacitive connection is considerably weaker than the N.N. coupling, i.e. ($C_{12} \ll C_{1c}, C_{2c}$). A distinctive feature of this design is the negative detuning of the qubits from the coupler.

Fig.3.5a illustrates the dependence on $\omega_c$ of this interaction mechanisms, leading to the condition $\frac{\omega_c}{2\Delta} - \frac{\omega_c}{2\Sigma} + 1 \leq 0$. As explored in Sec. 1.3.2, the frequency of the coupler can be continuously tuned. Thus, employing this circuit geometry with superconducting qubits inherently offers a solution for $\omega_c^{off}$, where the effective interaction is canceled, as shown in Fig. 3.5a ([7] [9] [78]).

## 3.3 iSWAP two-qubit gate

Gates that operate on a single qubit, when combined with a two-qubit entangling gate, form the essential gate set required for executing universal quantum computations [14]. In architectures based on transmon-like superconducting qubits, two-qubit gates can be generally divided into two main categories [34]:

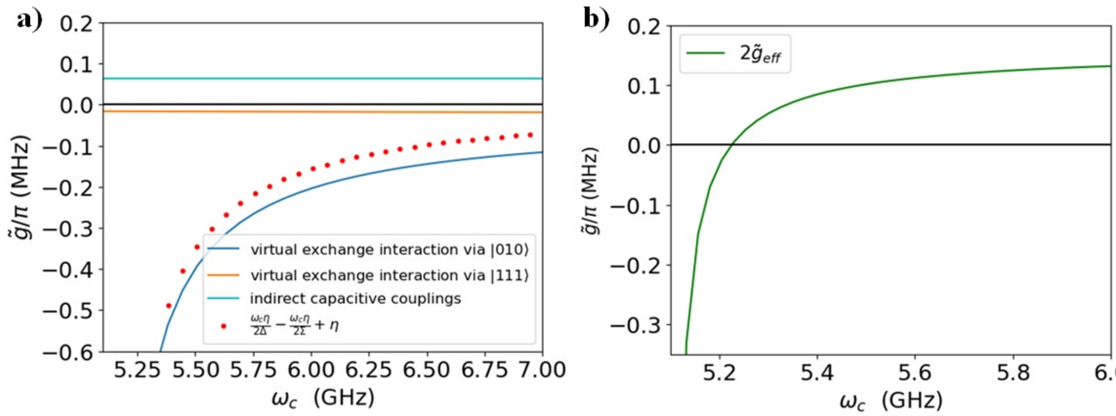


Figure 3.5: In **a)** the dependence on the coupler frequency of the processes of virtual exchange interaction is simulated. In blue the contribution via the state $|010\rangle$, given by $\frac{\omega_c}{2\Delta}\eta$. In orange the contribution via the state $|111\rangle$, given by $-\frac{\omega_c}{2\Sigma}\eta$. The latter contribution is related to the *CRW* terms, and is nearly constant for small detuning. The direct qubit-qubit coupling through indirect connection (green) is independent of $\omega_c$. The dashed line represents the cumulative behavior of the three processes, indicating that the process via $|010\rangle$ becomes significant near the off-condition. In **b)** the $\omega_c$-dependence of the effective interaction strenght $2\tilde{g}$, simulated using Eq. 3.10. The switch-off condition at $2\tilde{g} = 0$ occurs at a specific value of $\omega_c$ [7].

1. the former category involves the use of localized magnetic fields to adjust the qubits' transition frequencies, as shown in Fig. 3.1a.

2. the latter category relies exclusively on microwave control for gate operation [34].

In this section, we focus on the iSWAP two-qubit gate, which belongs to the former category.

### 3.3.1 iSWAP gate with fixed coupler configuration

In previous sections, we explored two different mechanisms for coupling a pair of qubits. Consider the straightforward case of two transmon qubits that are directly capacitively coupled. The Hamiltonian for this system results in two Duffing oscillators coupled through an interaction strength $g$:

$$H = \sum_{i=1,2} \left( \omega_i b_i^\dagger b_i - \frac{E_{C_i}}{2} b_i^\dagger b_i^\dagger b_i b_i \right) + g(b_1 - b_1^\dagger)(b_2 - b_2^\dagger). \tag{3.11}$$

As discussed in Sec. 1.2.3, under the assumptions of sufficient anharmonicity and drive control, higher-level excitations can be neglected [14], allowing us to truncate the Hamiltonian to a two-level system:

$$H = \sum_{i=1,2} \frac{\omega_i}{2} \sigma_{z,i} + g\sigma_{y,1}\sigma_{y,2} = \sum_{i=1,2} \frac{\omega_i}{2} \sigma_{z,i} - g(\sigma^+ - \sigma^-)_1(\sigma^+ - \sigma^-)_2. \tag{3.12}$$

Here we focus on the interaction term of Eq. 3.12 and employ the *RWA*, thereby neglecting the rapidly oscillating components:

$$H_{qq} = g\left(e^{i\delta\omega_{12}t}\sigma^{+}\sigma^{-} + e^{-i\delta\omega_{12}t}\sigma^{-}\sigma^{+}\right), \tag{3.13}$$

where $\delta\omega_{12} = \omega_{q1} - \omega_{q2}$ defines the detuning between the transition frequency of the two qubits, which can be modified employing the qubit frequencies flux-modulation of split-transmons, as discussed in Sec. 1.3.2. When we tune one of the two qubits on resonance with the other, such that $\delta\omega_{12} = 0$, the Hamiltonian becomes [14]:

$$\begin{aligned} H_{qq} &= g\left(\sigma_{+}\sigma_{-} + \sigma_{-}\sigma_{+}\right) && (3.14)\\ &= \frac{g}{2}\left(\sigma_x\sigma_x + \sigma_y\sigma_y\right). && (3.15)\end{aligned}$$

Without delving into the specifics of $g$, we recognize the excitation exchange behavior observed in Eqs. 3.2 and 3.7, which gives rise to the *swap* of energy between the two qubits, required to implement the iSWAP gate [14]. Given Eq. 3.15, this is often referred to as an *XY interaction.* The unitary operator describing the time evolution of an XY (or swap) interaction in a two-qubit system reads as follows [14]:

$$U_{qq}(t) = \exp\left(-i\frac{g}{2}(\sigma_x\sigma_x + \sigma_y\sigma_y)t\right) = \begin{pmatrix} 1 & 0 & 0 & 0\\ 0 & \cos(gt) & -i\sin(gt) & 0\\ 0 & -i\sin(gt) & \cos(gt) & 0\\ 0 & 0 & 0 & 1\end{pmatrix}. \tag{3.16}$$

When we tune the qubits on resonance for a time duration $t' = \frac{\pi}{2g}$, the system reduces to the iSWAP gate, represented by the unitary operator:

$$U_{qq}\left(\frac{\pi}{2g}\right) = \begin{pmatrix} 1 & 0 & 0 & 0\\ 0 & 0 & -i & 0\\ 0 & -i & 0 & 0\\ 0 & 0 & 0 & 1\end{pmatrix} \equiv \text{iSWAP}. \tag{3.17}$$

This gate swaps excitations between the two qubits while introducing a phase of $i = e^{i\pi/2}$ [14].

The initial step in the implementation of the iSWAP gate involves spectroscopic measurement of the avoided level crossing between the states $|01\rangle$ and $|10\rangle$ (as indicated by the red line in Fig. 3.6a). Once identified the flux region around the ALC, we set qubit 1 (QB1) to the state $|1\rangle$, while keeping qubit 2 (QB2) at its sweet spot to minimize flux noise. A flux pulse is then applied to QB1 to align both qubits on resonance for a time $\tau$, as depicted in the pulse sequence inset of Fig. 3.6b. During this time frame, the excitations oscillate between the two qubits, a phenomenon shown in Figs. 3.6b and 3.6c. Specifically Fig. 3.6c shows that as QB1 transitions from $|1\rangle$ to $|0\rangle$, QB2 transition from $|0\rangle$ to $|1\rangle$, in a time $t' = \frac{\pi}{2g}$. Therefore, the SWAP experiment can be considered as a complementary

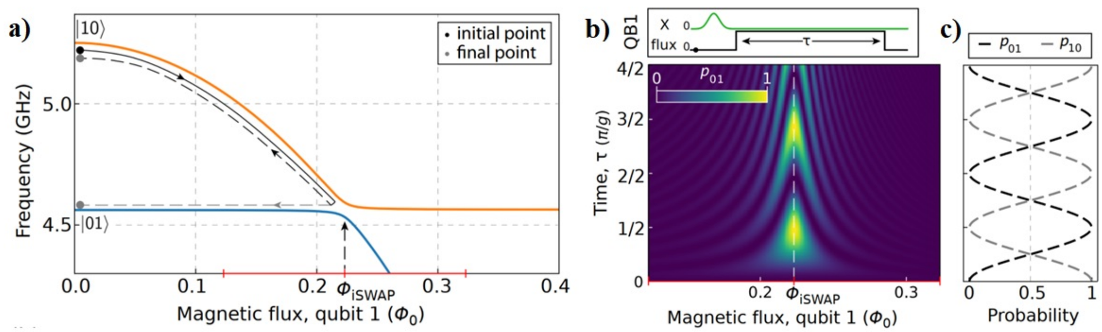


Figure 3.6: **a)** The spectrum of the $|0,1\rangle$ and $|1,0\rangle$ frequency transition of two transmon qubits as a function of the flux applied to qubit 1 (expressed in the two-qubit basis $|QB1, QB2\rangle$). A typical flux trajectory is indicated by black/dashed arrows to show how the iSWAP gate operates. **b)** Colorplot of the probability to be in the state $|10\rangle$ as a function of flux duration $\tau$ and amplitude in terms of $\phi_0$. The pulse pattern corresponds to setting up $|10\rangle$ and the application of a flux pulse in the avoided level crossing region. The maximum oscillation occurs at $\Phi = \Phi_{\text{iSWAP}}$ (white dashed line ). **c)** As more time is spent at the operational point ($\tau$), the probabilities of $|01\rangle$ (black) and $|10\rangle$ (gray) at $\Phi = \Phi_{\text{iSWAP}}$ coherently oscillate. Figure from [14].

tool to estimate the coupling strength $g$, which adds to the analysis of the gap opening in the ALC spectra.

Let us also note that in order to implement an efficient iSWAP gate, it must be sufficiently fast. This requires a strong coupling $g$ between the qubits. A weak coupling would make the gate too slow for practical applications. Therefore, it is of immeasurable importance to identify an analysis protocol able to determine the coupling strength of the devices prior to the implementation of a two-qubit gate.

### 3.3.2 iSWAP gate with tunable coupler configuration

In this section, we describe the implementation of the iSwap gate with tunable couplers. From Eq. 3.7 we observe an effective interaction leading to an exchange of energy between the two qubits.

We employ the notation $|Q1, Coupler, Q2\rangle$ to represent the eigenstates of Eq. 3.4 in the idling configuration, where the *Coupler* is placed at a frequency such that the effective *Q1*-*Q2* coupling is nearly zero. Assuming high detuning of the qubits from the coupler, this state symbolizes the *bare state* of Q1 and Q2, as indicated by dashed lines in Fig. 3.7b. Beyond the off-point condition, the actual interaction between *Q1* and *Q2* is non-zero, resulting in the manifestation of avoided crossings, as depicted by the solid curve in Fig.3.7b.

The implementation of the iSWAP gate is characterized by non-adiabatic transitions between $|100\rangle$ and $|001\rangle$. The regulation of energy exchange through these transitions is achieved by modulating the *Coupler* frequency $\omega_c$, which effectively tunes the coupling strengths $2\tilde{g}_{iSWAP}$ (Eq. 3.10), between the $|100\rangle$ and $|001\rangle$. The energy exchange between these states is quantified by preparing $|100\rangle$ and measuring the state population transferred to $|001\rangle$, varying $\tau$ and $\omega_c$, as shown by the color plot in Fig. 3.7c.

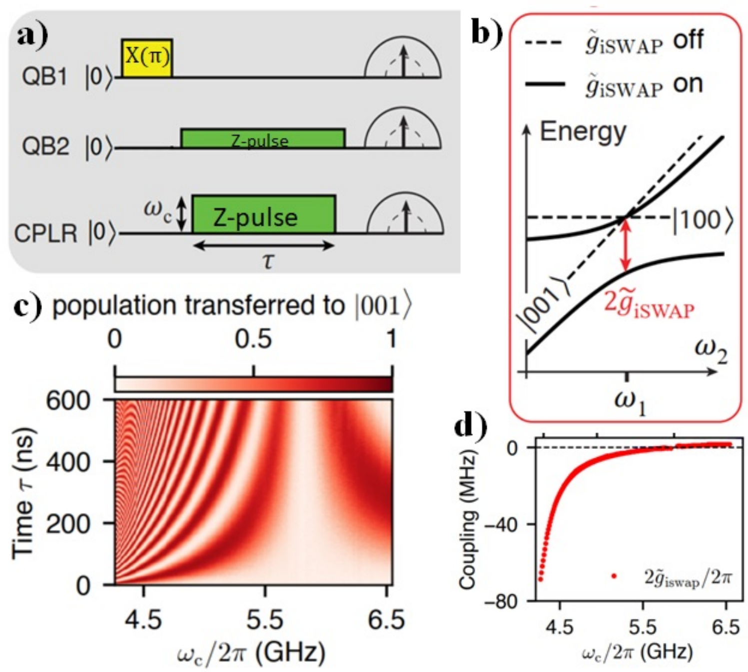


Figure 3.7: **a)** Schematic of the protocol for the iSWAP gate with the tunable coupler. $\tau$ represents the duration of the Z-pulse on the coupler, which switches on the interaction. **b)** Representation of the energy level crossing between *Q1* and *Q2*, in the case of off-interaction (dashed line) and in the case of on-interaction (solid line). **c)** Color plot of the swap between *Q1* and *Q2* as function of the coupler frequency $\omega_c$ and the pulse sequences $\tau$ shown in **a)**. In **d)**, the effective coupling strengths $2\tilde{g}$ as a function of the *Coupler* frequency $\omega_c$ obtained by the fitting of **c)**. Figure adapted from [78].

For the execution of the iSWAP gate, the states $|100\rangle$ and $|001\rangle$ are abruptly brought into resonance at their *bare* energy degeneracy point, with the coupler maintained at the off-point frequency. After that, the interaction is switched on by applying a Z-pulse to the coupler, with a duration that induces half of an oscillation, thus achieving a full swap of the two states. A schematic protocol is reported in Fig. 3.7a.

### 3.3.3 Conclusion and analysis of *ZZ* interaction

A fundamental bottleneck of the iSWAP gate is the presence of longitudinal interactions, also know as *ZZ*-crosstalk. Even when the qubits are dispersively detuned and excitation exchange between them is strongly suppressed [78], longitudinal *ZZ* couplings describe the dispersive shifts of the qubit energies resulting from the hybridization of the qubit wave functions due to the coupling capacitances, and can be quantified as [79]:

$$\zeta = E_{|101\rangle} - E_{|100\rangle} - E_{|001\rangle} + E_{|000\rangle}, \tag{3.18}$$

where $E_{|\alpha,\beta,\gamma\rangle}$ denotes the energy eigenvalue of the state $|\alpha, \beta, \gamma\rangle$ of the Hamiltonian 3.4.

Since *ZZ*-crosstalk induces phase errors [80], substantial efforts have been directed towards mitigating such unwanted interactions. In a fixed bus configuration, *ZZ*-crosstalk can be suppressed by significantly detuning the qubits from each other at the idle point. However, to facilitate the execution of two-qubit gates using this approach, the qubit transition frequencies would need to be tuned over extensive ranges, thereby elevating the risk of coupling to two-level system defects [81].

The tunable coupler allows for the precise control and elimination of unwanted *ZZ* interactions, thereby ensuring the high-fidelity execution of the iSWAP gate [9].

In order to understand this statement, an approximate expression of the *ZZ* coupling is considered, derived using a perturbation expansion of the Hamiltonian 3.4. We here assume that *Q1*, *Q2*, and *Coupler* are dispersively coupled to each other, with $g_{ij}/|\omega_i - \omega_j| \ll 1$ (where i, j = 1, 2, c, and i < j). Hence the static *ZZ* interaction $\zeta$ as a function of the Coupler frequency $\omega_c$, can be approximated up to the fourth order as [9][78][79]:

$$\zeta^{(2)} = g_{12}^2 \left( \frac{1}{\Delta_{12} - \alpha_2} + \frac{1}{\Delta_{21} - \alpha_1} \right), \tag{3.19}$$

$$\zeta^{(3)} = g_{12} g_{1c} g_{2c} \left( \left( \frac{4}{(\Delta_{21} - \alpha_1)\Delta_{2c}} + \frac{4}{(\Delta_{12} - \alpha_2)\Delta_{1c}} \right) + 2 \left( \frac{1}{\Delta_{1c}\Delta_{2c}} \right) + 2 \left( -\frac{1}{\Delta_{21}\Delta_{2c}} - \frac{1}{\Delta_{12}\Delta_{1c}} \right) \right), \tag{3.20}$$

$$\zeta^{(4)} = g_{1c}^2 g_{2c}^2 \left( \left( \frac{1}{\Delta_{1c}} + \frac{1}{\Delta_{2c}} \right)^2 \frac{1}{\Delta_{1c} + \Delta_{2c} - \alpha_c} \right. \tag{3.21}$$

$$- \left( \frac{1}{\Delta_{1c}} \right)^2 \left( \frac{1}{\Delta_{12}} + \frac{1}{\Delta_{2c}} - \frac{2}{\Delta_{12} - \alpha_2} \right) \tag{3.22}$$

$$\left. - \left( \frac{1}{\Delta_{2c}} \right)^2 \left( \frac{1}{\Delta_{21}} + \frac{1}{\Delta_{1c}} - \frac{2}{\Delta_{21} - \alpha_1} \right) \right), \tag{3.23}$$

where $\Delta_{ij} = \omega_i - \omega_j$, $(with\ i, j \in 1, 2, c$, and i < j), $\alpha_{1,2,c}$ is the anharmonicity and $g_{ij}$ are the strengths of the interaction from Eq. 3.4. Here the second-order expansion of the Hamiltonian yields the leading term in $ZZ$ coupling $\zeta^{(2)}$, and the coupler frequency-dependent contribution to $ZZ$ is represented solely by the third- and fourth-order terms $\zeta^{(3,4)}(\omega_c)$:

$$\zeta(\omega_c) \approx \zeta^{(2)} + \zeta^{(3,4)}(\omega_c). \tag{3.24}$$

Hence in a tunable coupler configuration, the control over the coupler frequency enables the suppression of the $ZZ$ interaction, as shown in Fig. 3.8 and thoroughly discussed in Ref. [9]. The second-order zeta coupling, in dark blue, does not depend on the coupler frequency, while the $\zeta^{(3,4)}(\omega_c)$ term induces an overall dependence on the tunable coupler frequency in the zeta interaction.

Conversely, in design where it is not possible to modulate the interaction, the ZZ coupling is intrinsic and always active, as in the two-qubit system coupled by a bus resonator discussed in Sec. 3.1. From the Eq. 3.2 the always-on ZZ interaction reads as [82]:

$$\zeta = J^2 \left( \frac{1}{\Delta_{12} - \alpha_2} + \frac{1}{\Delta_{21} - \alpha_1} \right), \tag{3.25}$$

where $\Delta_{ij} = \omega_i - \omega_j$ ($i, j \in 1, 2$, and i < j) is the detuning of the two qubits, $\alpha_{1,2}$ is the corrisponding anharmonicity and $J$ is the strength of the effective interaction in Eq. 3.2.

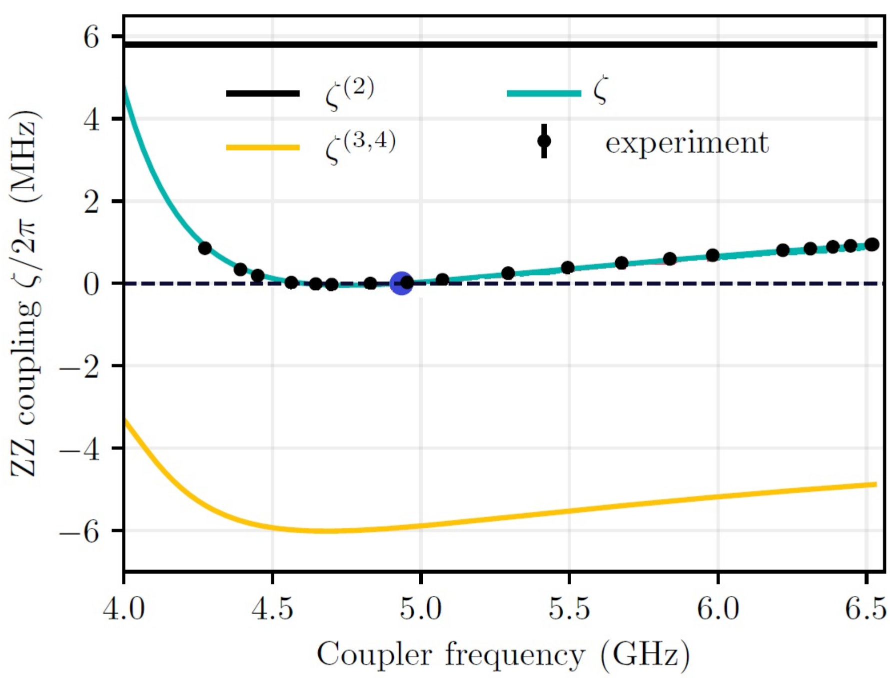


Figure 3.8: The strength of the *ZZ* interaction (cyan) is depicted as a function of the coupler frequency $\omega_c$. The contribution $\zeta^{(2)}$ (black) remains constant, whereas the contribution from the higher-order perturbative terms $\zeta^{(3,4)}$ (yellow) varies with the frequency of the coupler and is crucial for achieving the condition of $\zeta = 0$. The black dots represent experimental data points from Ref. [9].

# –4–
# Experimental results and data analysis



During the last decades, several coupling mechanisms between artificial superconducting quantum systems have been proposed ([78],[9],[79]), and have constantly evolved in order to guarantee better and better performances in scalable superconducting quantum processors ([8],[6]). This has automatically implied an increasing complexity of the devices, thus making fundamental the search for feasible self-consistent approaches for the analysis and the diagnostic of the coupling mechanisms. In this work, we propose to exploit the circuit Quantum Electrodynamics (cQED) to extract information on the coupling strengths in two superconducting multi-qubit transmon devices characterized by different coupling schemes (Sec. 3.1, 3.2). By calculating the energy spectra of coupled transmons beyond the perturbative approach, i.e. by exactly solving the eigenergies of the two-qubits Hamiltonian with the open-source Python package SCqubits (Appendix A.2), I've developed a comparative approach between simulations and experimental data, in order to extract fundamental design parameters of the devices, thus providing a physical picture of the coupling mechanisms in complex artificial two-level systems. Specifically for the case of tunable coupling schemes, this method allows us to explicitly take into account the mutual coupling between the computational qubits and the tunable coupler, and is proposed as a complementary tool for the estimation of the coupling strengths together with state-of-the-art time-domain experiments, like the XY-SWAP interaction experiment (Sec. 3.3.2). In order to validate this approach, the electrodynamics parameters of the devices are required, such as the qubit frequencies and the Josephson energies, as well as their behavior as a function of flux in tunable split-transmons, and the charge energy.

In Sec. 4.1, we report a spectroscopy characterization of readout resonators, and qubits (4.2). For diagnostic purposes, we also report information on the coherence and relaxation times of the devices under analysis (Sec. 4.3). In Sec. 4.4 we discuss the avoided level crossings (ALC) for different pairs in the two devices studied in this work, and we discuss the advantages and limitations of the analysis method proposed. Finally, we report our initial results on the SWAP experiment conducted on the prototype device with tunable coupling scheme (Sec. 4.4.4).

## 4.1 Resonators spectroscopy characterization

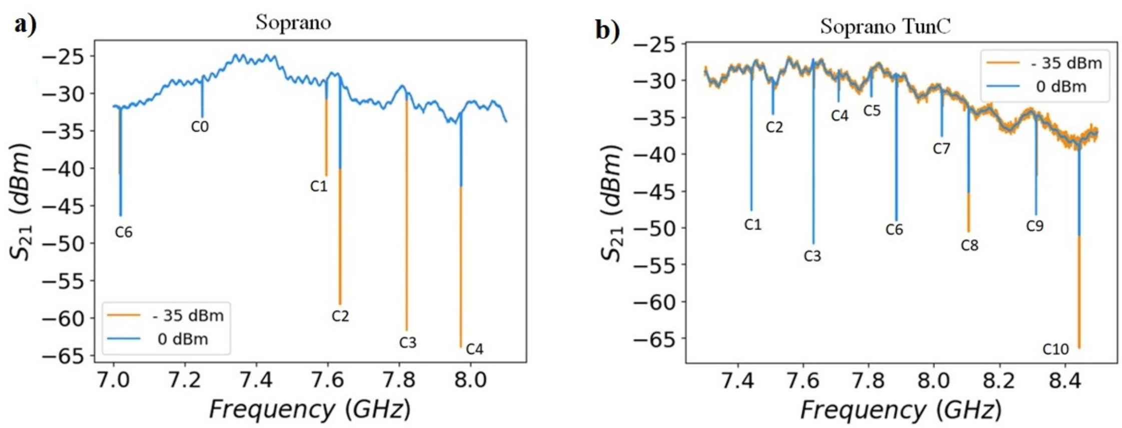


Figure 4.1: **a)** Spectroscopy measurement for the *Soprano* sample in the 7.3 GHz to 8.5 GHz frequency range on the feedline. It enables the qualitative identification of the cavities by comparing the results with design values. Measurements are performed at *0 dBm* and *-35 dBm* levels to acquire initial estimates of the cavities' power behavior. In **b)**, the same protocol is applied to the *Soprano TunC* sample.

In this section, we first present the results of the basic spectroscopy characterization measurements on the *Soprano* and *Soprano TunC* devices. Figure 4.1 shows the feedline spectroscopy measurements for both samples. In panel **a)**, the feedline transmission of the *Soprano* device shows six resonant frequencies in the range 7.1 GHz to 8.1 GHz. As discussed in Sec. 2.3, in this sample there are five readout resonators coupled to each qubit of the five-qubit matrix (C0 to C5), and one readout resonator coupled to the isolated qubit (C6). In panel **b)**, the feedline transmission of the *Soprano TunC* device shows ten resonant frequencies in a similar frequency range of 7.3 GHz to 8.5 GHz, corresponding to each cavity resonator in the device (Fig. 2.5b). Specifically, the first eight cavities correspond to the readout resonators of the 4 qubits pairs, while the last two resonances correspond to the test resonators coupled to the *Tunable Couplers* between *Qubit 3* and *Qubit 4*, and

| Soprano | | | | | | | | | | |
|---|---|---|---|---|---|---|---|---|---|---|
| Cavity | C0 | C1 | C2 | C3 | C4 | C5 | | | | |
| Readout frequency (bare) (GHz) | 7.200 | 7.400 | 7.600 | 7.800 | 8.000 | 7.000 | | | | |
| Readout frequency* (GHz) | 7.248 | 7.596 | 7.634 | 7.821 | 7.972 | | | | | |
| Qubit coupled | Q0 | Q1 | Q2 | Q3 | Q4 | Q5 | | | | |
| **Soprano Tunc** | | | | | | | | | | |
| Cavity | C1 | C2 | C3 | C4 | C5 | C6 | C7 | C8 | C9 | C10 |
| Readout frequency (bare) (GHz) | 7.200 | 7.300 | 7.4 | 7.500 | 7.600 | 7.700 | 7.800 | 7.900 | 8.000 | 8.100 |
| Readout frequency* (bare) (GHz) | 7.440 | 7.510 | 7.630 | 7.710 | 7.810 | 7.890 | 8.020 | 8.110 | 8.310 | 8.445 |
| Qubit coupled | Q1 | Q3 | Q5 | Q7 | Q2 | Q4 | Q6 | Q8 | TC34 | TC78 |

Table 4.2: Comparison between the expected values by design and the actual values(*) for the *Soprano* device (top) and for the *Soprano TunC* device (bottom). For each sample, the labels of readout cavities with the relative labeled qubits. For the *Soprano* we focused on the pairs *Qubit 0* and *Qubit 2* (red). For the *Soprano TunC* device, measurements included the *Qubit 7* and *Qubit 8* pair with its relative coupler TC78 (green), and the *Q5* and *Q6* pair (blue), whose coupling qubit does not have a readout cavity.

between *Qubit 7* and *Qubit 8*. For both the devices a comparison between high and low power through the input feedline (0 dBm and -35 dBm, respectively) is also reported.

As follows, we will focus our attention on the spectroscopic characterization of one pair of the Soprano device, *Qubit 0* and *Qubit 2*, which here plays the role of reference. Then, for statistical purposes, we benchmark the design properties of two pairs of the prototypal *Soprano TunC* device: *Qubit 7* (Q7) and *Qubit 8* (Q8), which are equipped with a readout resonator for the *tunable coupler* of Q7 and Q8 (TC78), and the pair *Qubit 5* (Q5) and *Qubit 6* (Q6), which instead follows a more standard design, with no additional readout resonator on the tunable coupler (TC56).

### 4.1.1 Soprano

**Resonators spectroscopy as a function of power**

As outlined in Sec. 2.6.1, the first single-qubit characterization step involves the measurement of the feedline transmission magnitude $S_{21}$, with a typical 10 MHz span around the expected readout resonator frequencies. A dip in the trace is observed when the readout tone resonates with the cavity, as discussed in Sec. 2.6. The measurement is repeated for different input powers, and the results are presented in a colormap plot, as shown in Fig. 4.3a for the readout resonator coupled to *Qubit 0*. At large powers of the input signal, the bare state is observed (see blue line in Fig. 4.3b), at 0 dBm VNA output. By decreasing the input power, we reach the low-photon regime, observing a positive shift of the cavity

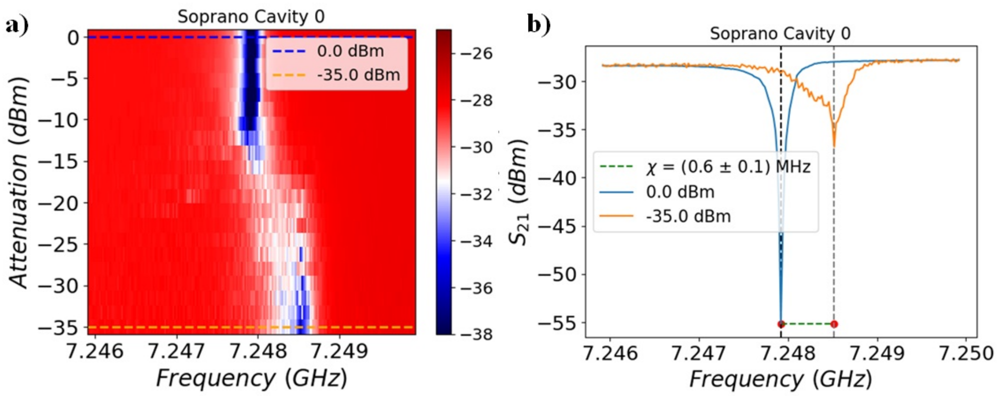


Figure 4.3: **a)** Power sweep colormap for Cavity 0 coupled to qubit 0: the VNA input power in dBm (y-axis) is reported as a function of the VNA tone frequency (x-axis). The color scale reports the readout magnitude of the $S_{21}$ output. **b)** Two plot cuts for comparison, at 0 dBm and - 35 dBm, from which we estimate the low-photon shift $\chi$. As described in the scheme of Fig. 2.8, this measurement setup provides an additional 50 dBm attenuation at the cryogenic stages, which add to the VNA input power.

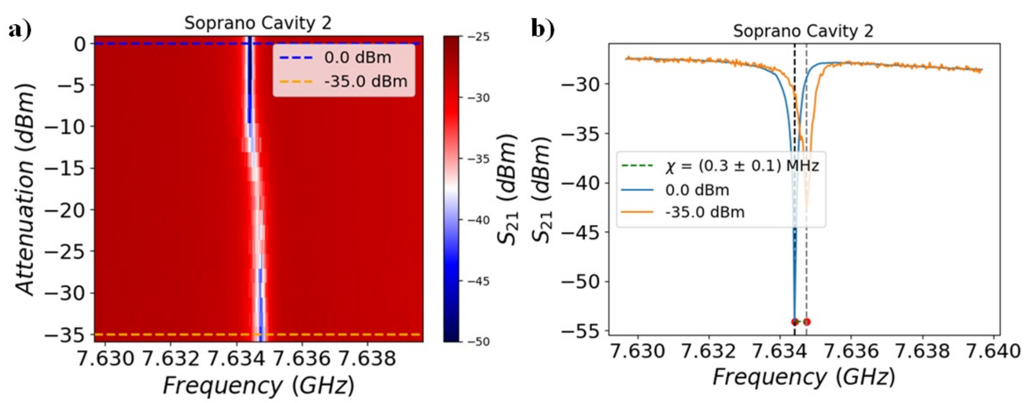


Figure 4.4: **a)** Power sweep colormap for Cavity 2 coupled to qubit 2: the VNA input power in dBm (y-axis) is reported as a function of the VNA tone frequency (x-axis). The color scale reports the readout magnitude of the $S_{21}$ output. **b)** Two plot cuts for comparison, at 0 dBm and - 35 dBm, from which we estimate the low-photon shift $\chi$. As described in the scheme of Fig. 2.8, this measurement setup provides an additional 50 dBm attenuation at the cryogenic stages, which add to the VNA input power.

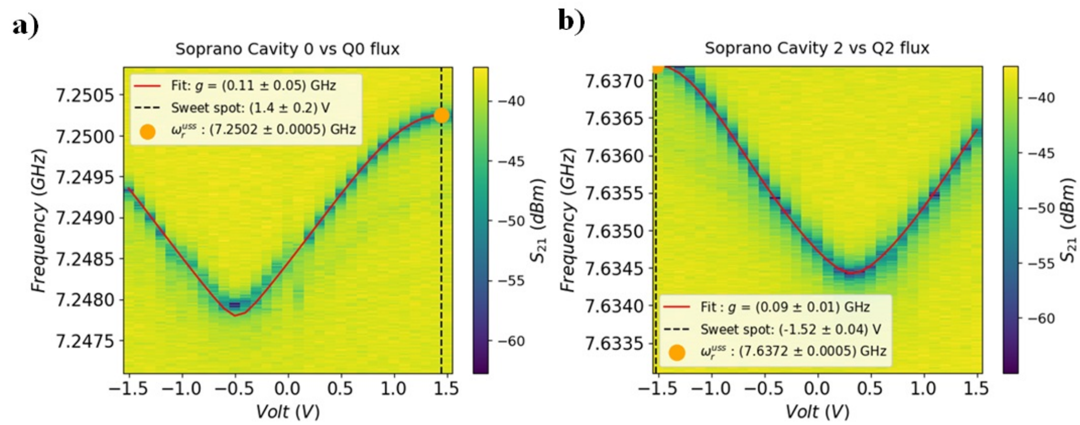


Figure 4.5: **a)** Flux sweep colormap for *Cavity 0* for the readout magnitude of the $S_{21}$ output as a function of both the VNA tone frequency (y-axis) and the voltage bias applied to *qubit 0* via the dedicated flux line. The fit (red curve) is based on Eq. A.1 (see Appendix A.1). The dotted line indicates the estimated value for the upper sweet spot and the maximum modulation value of $\omega_r$ (orange spot) obtained from the fit. **b)** A similar measurement is repeated for *Cavity 2*.

frequency (see the orange curve in Fig. 4.3b)). This provides a measure of the low-photon shift $\chi$. The resonance frequencies in the two states with the relative maximum error are $\omega_r^{bare} = (7.2479 \pm 0.0005)\ \ GHz$ and $\omega_r^{lp} = (7.2485 \pm 0.0005)\ \ GHz$. From these data, we evaluate a low-photon shift $\chi$, and results $(0.6 \pm 0.1)\ \ MHz$, using maximum error propagation.

Similar investigations are performed on *Cavity 2*, which is coupled to *qubit 2*. Figure 4.4a displays the resonator spectroscopy measurement as a function of the VNA input signal power, while in panel 4.4b we show the cross-section at the highest and lowest input power signals. The resonance frequencies for the bare and low-photon regime are $\omega_r^{bare} = (7.6344 \pm 0.0005)\ \ GHz$ and $\omega_r^{lp} = (7.6347 \pm 0.0005)\ \ GHz$, with the relative maximum error. From these data, we obtain a low-photon shift $\chi = (0.3 \pm 0.1)\ \ MHz$.

**Resonators spectroscopy as a function of flux**

In the *Soprano*, *Qubits 0* and *Qubit 2* are both split-transmon (Sec. 2.3). As discussed in Sec. 2.6.1, the readout frequency for the cavity coupled to a split-transmon in the low-photon regime becomes dependent on the flux applied on the qubit (see Eq. 2.5).

In Fig. 4.15a, the flux bias behavior of *cavity 0* coupled to *Qubit 0*, shows half modulation in a voltage range of 3 V across the dedicated flux line for *Qubit 0*. We observe that the maximum modulation does not occur at zero voltage (or zero flux, refer to Appendix A.1), a common occurrence in superconducting circuits due to residual magnetization from flux trapping phenomena [4]. From these measurements, we can identify the flux *sweet spot*, a crucial point for qubit measurements, as discussed in Sec. 1.3.2.

To interpret the observed behavior, we used a *Non-Linear Least Squares* fit, employing Python's SciPy library [83]. We refer to Appendix A.1 for details. The fit yields a *sweet spot* value of $(1.4 \pm 0.2)$ V, and the frequency at the *sweet spot*, $\omega_r^{ss} = (7.2502 \pm 0.0005)\ \ GHz$. This approach allows to fit the coupling strength $g = (110 \pm 50)\ \ MHz$. Errors are determined by

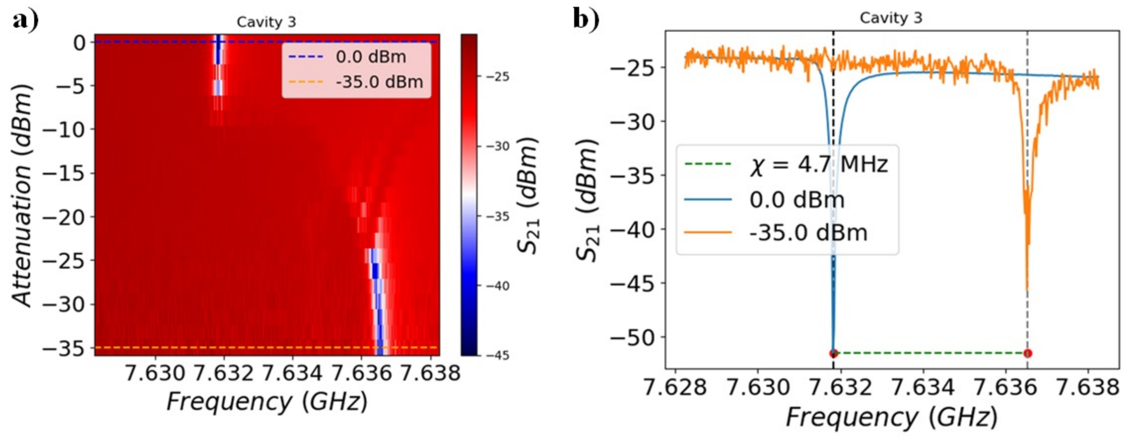


Figure 4.6: **a)** Power sweep colormap for Cavity 3 coupled to Q5: the VNA input power in dBm (y-axis) is reported as a function of the VNA tone frequency (x-axis). The color scale reports the readout magnitude of the $S_{21}$ output. **b)** Two plot cuts for comparison, at 0 dBm and - 35 dBm, from which we estimate the low-photon shift $\chi$. As described in the scheme of Fig. 2.8, this measurement setup provides an additional 50 dBm attenuation at the cryogenic stages, which add to the VNA input power.

Non-Linear Least-Squares Minimization, with the exception of the *sweet spot* frequency, where the maximum error is applied. Corresponding measurements for *Cavity 2* coupled to *Qubit 2* are shown in Fig. 4.5b, yielding a sweet spot value of $(-1.52 \pm 0.04)$ V and a frequency at the *sweet spot*, $\omega_r^{ss}$ of $(7.6372 \pm 0.0005)\ \ GHz$. The coupling strength $g$ is $(90 \pm 10)\ MHz$. Standard error from the fit is used, except for the frequency, where the maximum error is applied.

### 4.1.2 Soprano TunC

**Resonators spectroscopy as a function of power**

Following the same experimental procedure for readout resonator spectroscopy of the Soprano device, we first report in Fig. 4.6a the measure of low-photon shift on Cavity 3, coupled to Q5. In panel b), we show two line-cuts in the high- and low-power regime, which identifies the bare and low-photon states. The resonance frequencies in the two states with the relative maximum error are $\omega_r^{bare} = (7.6318 \pm 0.0005)\ \ GHz$ and $\omega_r^{lp} = (7.6365 \pm 0.0005)\ \ GHz$. From these data, we evaluate a low-photon shift $\chi = (4.7 \pm 0.1)\ \ MHz$, using maximum error propagation.

Similar investigations were performed for *Cavity 7*, which is coupled to Q6. Figure 4.7a displays the resonator spectroscopy measurement, as a function of the VNA input signal power, where *Cavity 7* manifests the usual low-photon shift. The resonance frequencies for the bare and low-photon regimes are $\omega_r^{bare} = (8.0247 \pm 0.0005)\ \ GHz$ and $\omega_r^{lp} = (8.0279 \pm 0.0005)\ \ GHz$, with maximum error. From these data, we obtain a low-photon shift $\chi = (3.2 \pm 0.1)\ \ MHz$, where we use maximum error propagation.

On pair of Q7 and Q8, the same procedure was followed. The low-photon shift on

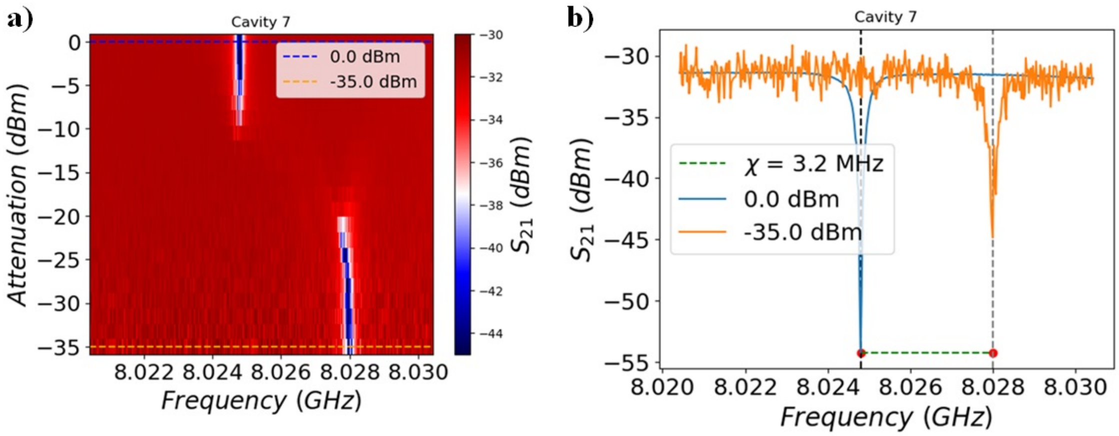


Figure 4.7: **a)** Power sweep colormap for Cavity 7 coupled to Q6: the VNA input power in dBm (y-axis) is reported as a function of the VNA tone frequency (x-axis). The color scale reports the readout magnitude of the $S_{21}$ output. **b)** Two plot cuts for comparison, at 0 dBm and - 35 dBm, from which we estimate the low-photon shift $\chi$. As described in the scheme of Fig. 2.8, this measurement setup provides an additional 50 dBm attenuation at the cryogenic stages, which add to the VNA input power.

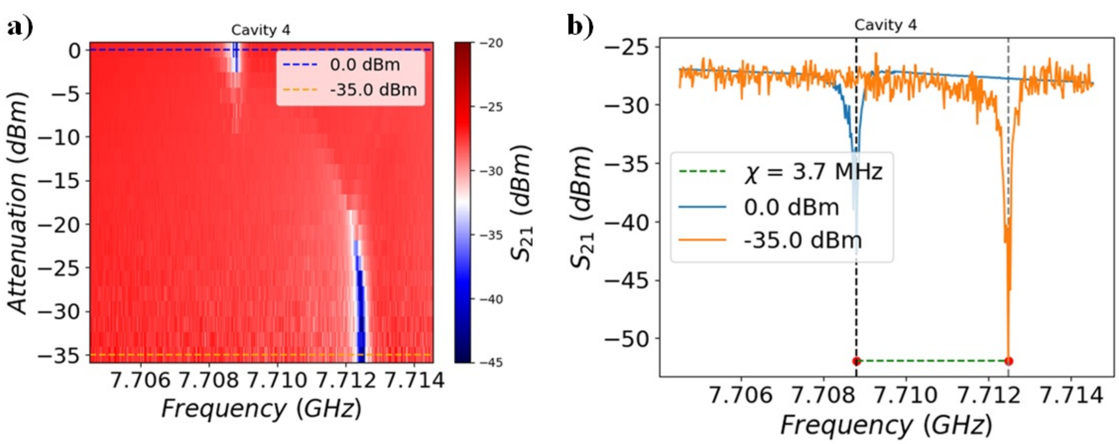


Figure 4.8: **a)** Power sweep colormap for Cavity 4 coupled to Q7: the VNA input power in dBm (y-axis) is reported as a function of the VNA tone frequency (x-axis). The color scale reports the readout magnitude of the $S_{21}$ output. **b)** Two plot cuts for comparison, at 0 dBm and - 35 dBm, from which we estimate the low-photon shift $\chi$. As described in the scheme of Fig. 2.8, this measurement setup provides an additional 50 dBm attenuation at the cryogenic stages, which add to the VNA input power.

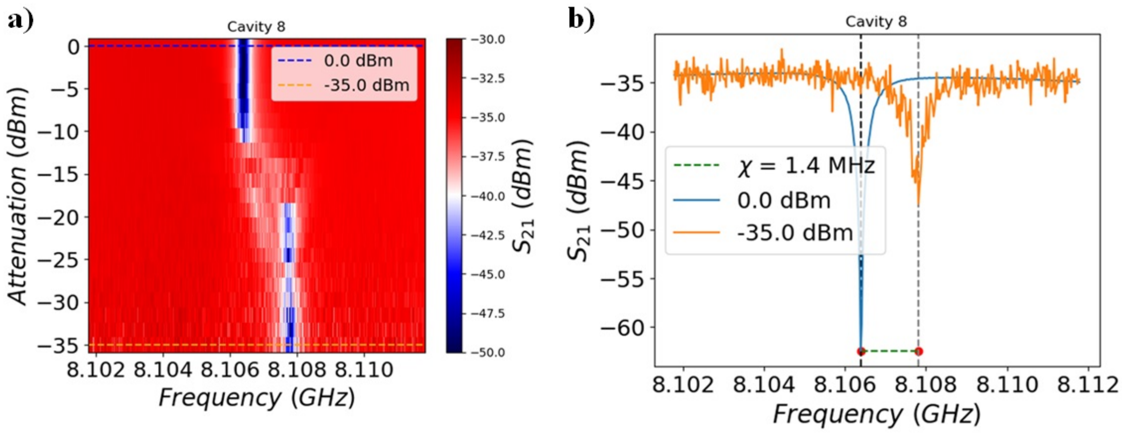


Figure 4.9: **a)** Power sweep colormap for Cavity 8 coupled to Q8: the VNA input power in dBm (y-axis) is reported as a function of the VNA tone frequency (x-axis). The color scale reports the readout magnitude of the $S_{21}$ output. **b)** Two plot cuts for comparison, at 0 dBm and - 35 dBm, from which we estimate the low-photon shift $\chi$. As described in the scheme of Fig. 2.8, this measurement setup provides an additional 50 dBm attenuation at the cryogenic stages, which add to the VNA input power.

*Cavity 4*, which is coupled to Q7 is shown in Figure 4.7. Panel **a)** displays the resonator spectroscopy measurement, as a function of the VNA input signal power, where *Cavity 4* manifests the usual low-photon shift. The resonance frequencies for the bare and low-photon regimes are $\omega_r^{bare} = (7.7088 \pm 0.0005)\ GHz$ and $\omega_r^{lp} = (7.7124 \pm 0.0005)\ GHz$, with the maximum error. From these data, we evaluate a low-photon shift of $\chi = (3.7 \pm 0.1)\ MHz$, where we use a maximum error propagation.

The measurement of low-photon shift on Cavity 3, coupled to Q5, is shown in Fig. 4.6a. In panel b), we show two line-cuts in the high- and low-power regimes, which identifies the bare and low-photon states. The resonance frequencies in the two states with the corresponding maximum errors are $\omega_r^{bare} = (8.1064 \pm 0.0005)\ GHz$ and $\omega_r^{lp} = (8.1078 \pm 0.0005)\ GHz$. From these data, we evaluate a low-photon shift of $\chi = (1.4 \pm 0.1)\ MHz$, where we use maximum error propagation.

The results obtained for cavities C4 and C7 are in line with Eq. 1.48, whereas C3 shows the largest low-photon shift. In the hypothesis of similar coupling factors g, which holds if we consider that the resonators are fabricated within the same conditions, this result is expected, being the detuning $\Delta = \omega_r - \omega_{01}^{Q5}$ smaller than for the other cavities. *Cavity* 8 has a low-photon shift smaller than expected: this behavior is compatible with the fact that the tunable qubit Q8 coupled to *Cavity* 8 has trapped some flux, and therefore the cavity is closer to its lower sweet-spot, as we will see in the next section.

**Resonators spectroscopy as a function of flux**

We now focus our attention on the flux dependence of the resonance frequencies. In the *Soprano TunC*, Q5 and Q8 and their couplers *TC56* and *TC78*, are split-transmon (Sec. 2.3). Only the tunable coupler of *pair 78* is coupled to a readout resonator, enabling us to study the flux dependence on the corresponding C10 (Table 4.2).

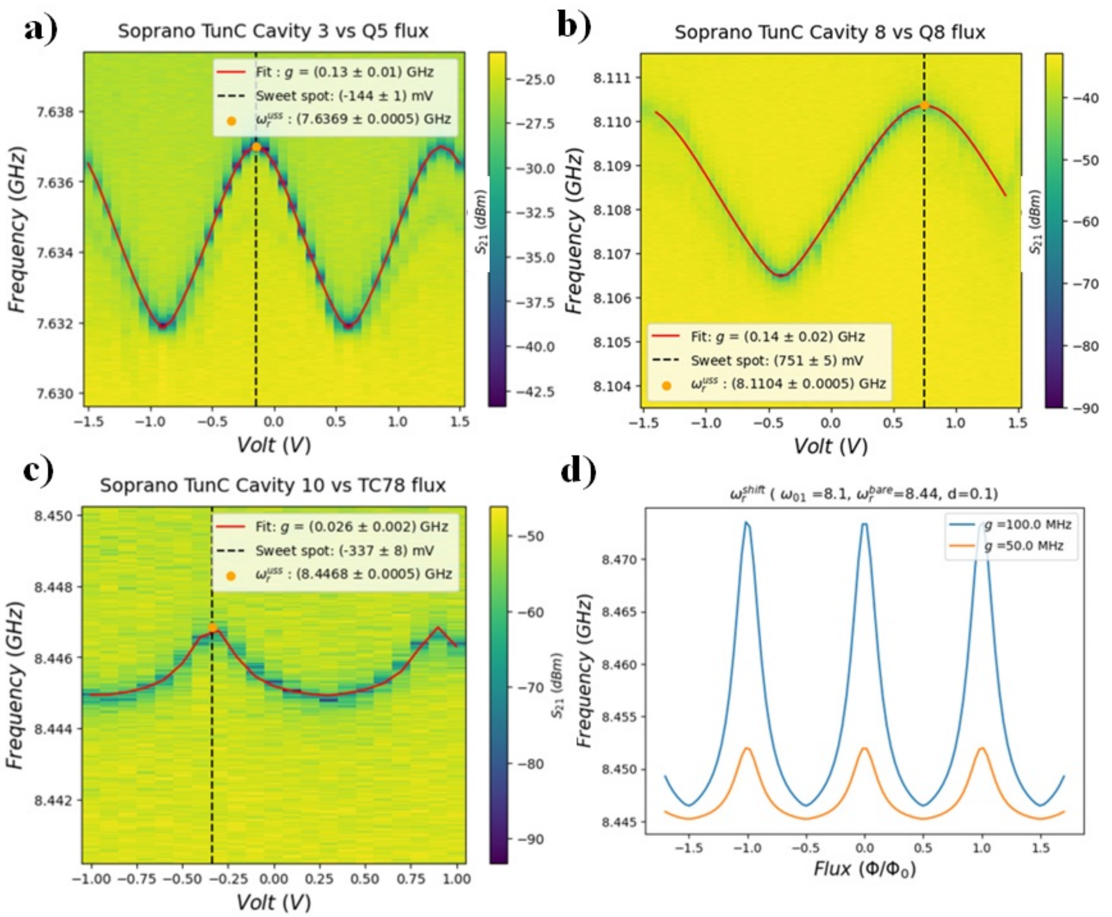


Figure 4.10: **a)** Flux sweep colormap for *Cavity 3* of the readout magnitude of the $S_{21}$ output as a function of both the VNA tone frequency (y-axis) and the voltage bias applied to *Q5* dedicated flux line. The fit (red curve) is based on Eq. A.1 (see Appendix A.1). The dotted line indicates the estimated value for the upper sweet spot and the maximum modulation value of $\omega_r$ (orange spot) obtained from the fit. **b)** A similar measurement is done for *Cavity 8*. **c)** The corresponding measurement for *Cavity 10*, demonstrating observable lower frequency modulation related to the lower value of the coupling strength, $g$. **d)** Plot of Eq.1.41 for $\omega_{01} = 8.1\ GHz$, $\omega_r^{bare} = 8.44\ GHz$, $d = 0.1$, comparing trends for g values of 100 MHz and 50 MHz and association of smaller coupling force with reduced frequency modulation amplitude.

To interpret the observed behavior, we use a *Non-Linear Least Squares* fit, employing *Python's SciPy* library [83]. We refer to Appendix A.1 for details. We start with the flux dependence of *Cavity 3* coupled to Q5, where, in Fig. 4.10b, a complete modulation in the voltage range of 3 V is observed. From the fit we obtain a *sweet spot* value of $(-144 \pm 1)$ mV with the frequency value at the *sweet spot*, $\omega_r^{lp}$, being $(7.6369 \pm 0.0005)\ \ GHz$. The coupling strength $g$ is $(130 \pm 10)\ \ MHz$. Errors are given by Non-Linear Least-Squares Minimization, except for the *sweet spot frequency*, where the maximum error is used. Identical measurements were conducted for *Cavity 8* coupled to *Q8*, and *Cavity 10* coupled to *Tunable Coupler 78*, with the results summarized in Table 4.11.

| ***Cavity label*** | Cavity 3 | Cavity 8 | Cavity 10 |
|---|---|---|---|
| $Design\ \ (GHz)$ | 7.4 | 7.9 | 8.1 |
| $Exp \pm 5 \cdot 10^{-4}$ (GHz) | **7.6370** | **8.1104** | **8.4468** |
| Sweet spot $(mV)$ | $-144 \pm 1$ | $751 \pm 5$ | $-337 \pm 8$ |
| $g\ \ (MHz)$ | $130 \pm 10$ | $140 \pm 20$ | $26 \pm 2$ |
| $Qubit$ | Q5 | Q8 | TC78 |

Table 4.11: Comparative table of the tunable frequencies for the readout cavities for the *Soprano TunC*, with the corresponding tunable qubits labeled. The $\omega_r^{ss}$ values obtained by the fit are highlighted in bold font, as detailed in Appendix A.1. For each cavity, the value of the coupling force $g$ and the voltage at the *sweet spot* are derived from the fit.

When comparing the derived coupling values, the coupling force of *Cavity 10* to the tunable coupler is an order of magnitude smaller than those obtained for *Cavities 8* and *3*. This design choice complies with the requirement to avoid excessive coupling between a non-computational element, like a tunable coupler, and its readout resonator. The reduced coupling value also induces a reduced frequency modulation in flux, as evident from the modulation of *Cavity 10* in Fig.4.10c. This result is in agreement with the trend predicted by Eq. A.1, where a decrease in coupling strength results in a reduced modulation amplitude, as shown in Fig.4.10d. The standard errors of the fit are on the order of the millivolt (mV) unit, while the acquired points exhibit a step of tens of mV. Consequently, a variation up to the order of tens of mV in the fit values compared to the real values is expected. This limitation represents a compromise between capturing the complete flux modulation behavior of resonators coupled with qubits over a large voltage range with adequate resolution and the constraints of experimental measurement times. More accurate measurements of the *sweet spot* points for the qubit can be achieved by acquiring more points in the qubit flux spectroscopy measurements (Sec. 4.2). Additionally, Eq. 2.5 neglects higher-order approximation terms, indicating an intrinsic limitation to our modeling approach.

| Device | Soprano | | Soprano Tunc | | | | |
|---|---|---|---|---|---|---|---|
| Qubit label | Qubit 0 | Qubit 2 | Q5 | Q6 | Q7 | Q8 | TC 78 |
| $\omega_R^{ss}$ $(GHz)$ error | 7.2502 $\pm$0.0005 | 7.6372 $\pm$0.0005 | 7.6369 $\pm$0.0005 | <u>8.0279</u> $\pm$0.0005 | <u>7.7124</u> $\pm$0.0005 | 8.1104 $\pm$0.0005 | 8.4468 $\pm$0.0005 |
| $\chi$ $(MHz)$ error | 0.6 $\pm$0.1 | 0.3 $\pm$0.1 | 4.7 $\pm$0.1 | 3.2 $\pm$0.1 | 3.7 $\pm$0.1 | 1.4 $\pm$0.1 | |
| ***Sweet spot*** (V) error | 1.4 $\pm$0.2 | −1.52 $\pm$0.04 | −0.144 $\pm$0.001 | | | 0.751 $\pm$0.005 | −0.337 $\pm$0.008 |
| ***g*** (MHz) error | 110 $\pm$50 | 90 $\pm$10 | 130 $\pm$10 | | | 140 $\pm$20 | 26 $\pm$2 |

Table 4.12: Summary of values obtained for both the devices *Soprano* and *Soprano Tunc*. For each qubit, it shows the values obtained from the fit (Appendix A.1) for the readout resonator frequency at *sweet spot* ($\omega_{01}^{ss}$), the low-photon shift ($\chi$), with the error given by the maximum error and the propagation on the maximum error, respectively. Additionally, the sweet spot value and the coupling strength ($g$) between the qubits and their associated cavities, along with the standard errors from the fit. For the fixed qubits Q6 and Q7, values from the spectroscopy measurement (underlined) are reported, with the respective maximum errors.

### 4.1.3 Summary of readout electrodynamics parameters

A comparison with the results obtained for the two analyzed devices is in order: first of all, the cavities measured in the Soprano sample reveal a lower low-photon shift (see Table 4.12), potentially related to a larger detuning between readout and qubit frequencies. Indeed, power shift experiments have been performed at zero external flux field, where *qubit 0* and *qubit 2* pairs were far from the sweet-spot (Fig. 4.5). Moreover, the flux modulation periodicity occurs on a wider voltage range for *Soprano TunC*. In these experiments, the flux cryogenic lines were equipped with an attenuation of -20dB, while for the Soprano experiment, the attenuation was of -30 dB. This induces an increase in the resistance of the cryogenic lines. Hence, within the same voltage applied, the flux threading the split-transmons in the *Soprano TunC* is effectively larger than for the Soprano experiment. Reducing the attenuation on the flux lines presents a trade-off: while it increases the flux modulation range, attenuation stages are crucial for isolating the sample from the external environment [14].

Finally, the coupling $g$ between the readout resonators and flux-tunable computational qubits of the prototypal *Soprano TunC* design complies within the errors with the readout-qubit coupling in the benchmark *Soprano* device, while the $g$-factor for the tunable coupler in the *Soprano TunC* is one order of magnitude lower. This complies with the design choice to avoid excessive coupling with non-computational elements on chip.

## 4.2 Qubit spectroscopy

As detailed in Sec. 2.6.1, the two-tone spectroscopy measurement provides information on the qubit frequency and its anharmonicity.

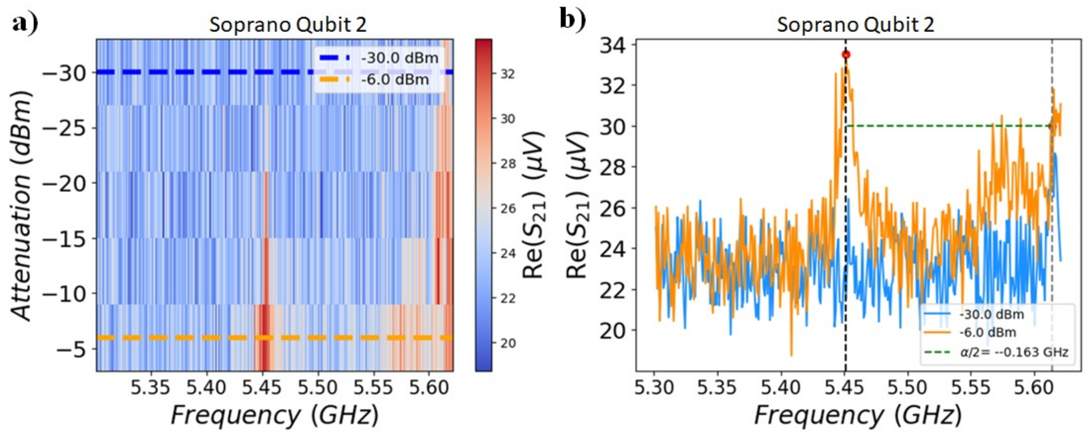


Figure 4.13: *Qubit 2* spectroscopy: in **a)**, the attenuation of the qubit drive signal (y-axis), on the x-axis the qubit drive Q2 frequency, the color scale identifies the real part of the demodulated voltage signal in $\mu V$ of the readout resonator. In **b)** linecuts at -30 dBm (blue) and -6 dBm (orange). The half anharmonicity is also reported (dashed green line).

### 4.2.1 Soprano

**Qubit spectroscopy as a function of power**

In Fig. 4.13a we show the real part of the demodulated readout voltage output as a function of the qubit drive frequency and the qubit drive power applied across the dedicated drive line for *qubit 2*, where *qubit 2* is at $0.25\ \ \Phi/\Phi_0$, the value nearest to the *upper sweet spot* reachable by the experimental set-up.

As shown in Fig.4.13b at low power (-30dBm attenuation on the drive signal), we can distinguish the transition $|0\rangle \rightarrow |1\rangle$ at the highest frequency. By increasing the power (-6 dBm attenuation on the drive line), the transition $|0\rangle \rightarrow |2\rangle$ appears at lower frequencies, given the typical negative anharmonicity in the transmon regime (Sec. 1.2.3), and the peak $|0\rangle \rightarrow |1\rangle$ broadens. This is related to the increasing number of photons in the system, which increases loss mechanisms [84]. The transition $|0\rangle \rightarrow |1\rangle$ occurs at frequency $(5.614 \pm 0.002)\ \ GHz$. We can extrapolate the anharmonicity as $\alpha = (f_{01} - f_{02})/2$ obtaining $\alpha = (-326 \pm 4)\ \ MHz$, with the maximum error.

The same investigation was conducted for *Qubit 0*, and is shown in Fig. 4.14a. The readout magnitude of the $S_{21}$ output is shown as a function of the qubit drive frequency and the qubit drive power applied across the dedicated drive line for *qubit 0*. The qubit frequency $f_{01}$ is $(4.509 \pm 0.002)\ GHz$ and the anharmonicity is $\alpha = (-268 \pm 4) MHz$., where the errors are maximum errors.

**Qubit spectroscopy as a function of flux**

Additionally, in Fig. 4.15 we report *Qubit 0* spectroscopy measurement as a function of an external flux field, in order to highlight the flux dependence of the $|01\rangle$ transition frequency (Sec. 4.1.2). The experimental curves have been fitted using the same approach followed for the readout resonators, as discussed in Appendix A.1. Specifically, we used Eq. A.2 to model the flux modulation of $f_{01}$ frequency. The theoretical fit yields a sweet spot

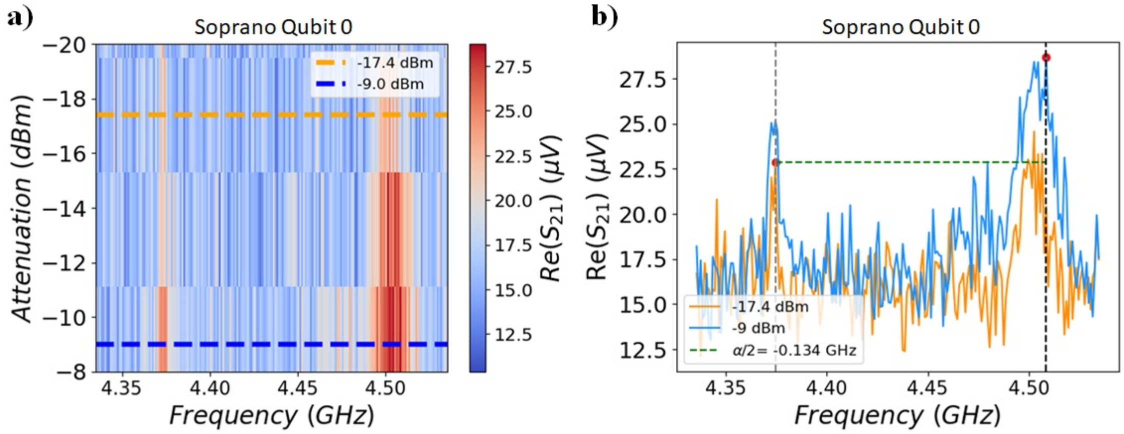


Figure 4.14: *Qubit 0* spectroscopy: in **a)** the attenuation of the qubit drive signal (y-axis), on the x-axis the qubit drive Q0 frequency, the color scale identifies the real part of the demodulated voltage signal in $\mu V$ of the readout resonator. In **b)** linecuts at -17.4 dBm (orange) and -9 dBm (blue). The half anharmonicity is also reported (dashed green line).

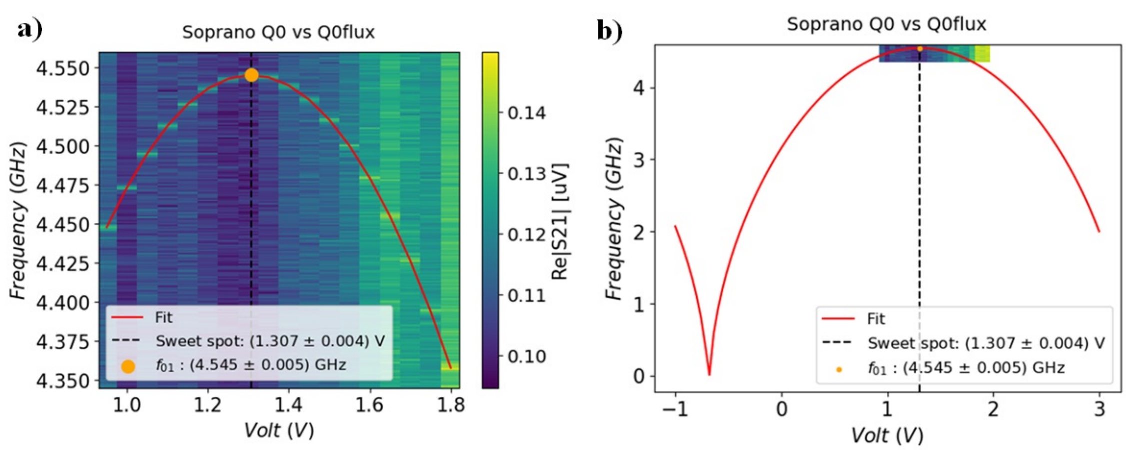


Figure 4.15: Flux spectroscopy of *qubit 0*. **a)** Colorplot with the flux on Q0 in voltage (x-axis), the Q0 drive frequency signal (y-axis), and the color scale of the magnitude of the readout resonator. The fit (red curve) is based on Eq. A.2. The dotted line indicates the estimated value for the upper sweet spot and the maximum modulation value of $\omega_{01}^{uss}$ (orange spot) obtained from the fit. **b)** Extrapolated behavior from the fit, of the qubit frequency $\omega_{01}$ of qubit 0 versus the drive flux in voltage.

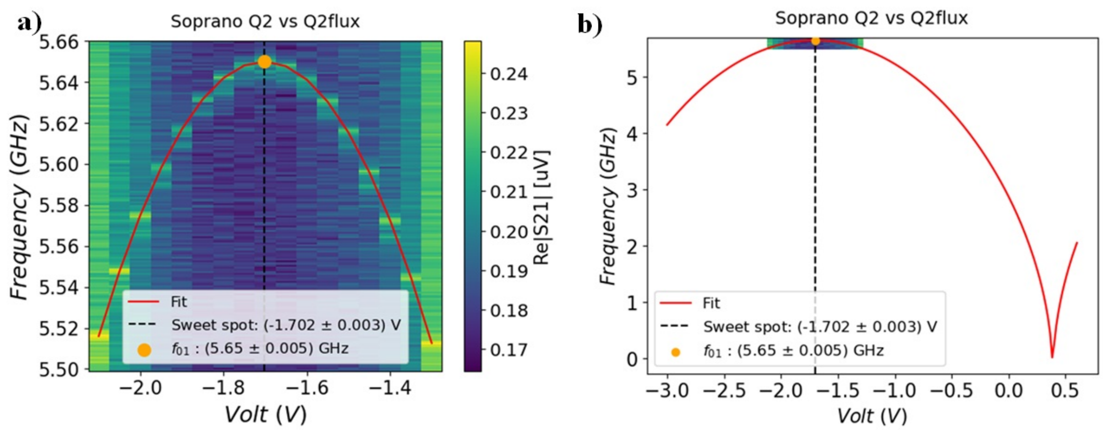


Figure 4.16: Flux spectroscopy of *qubit 2*. **a)** Colorplot with the flux on Q2 in voltage (x-axis), the Q2 drive frequency signal (y-axis), and the color scale of the magnitude of the readout resonator. The fit (red curve) is based on Eq. A.2. The dotted line indicates the estimated value for the sweet spot and the maximum modulation value of $\omega_{01}^{ss}$ (orange spot) obtained from the fit. **b)** Extrapolated behavior from the fit of the qubit frequency $\omega_{01}$ of qubit 2 vs the drive flux in voltage.

value of $(1.307 \pm 0.004V)$ and a frequency at the sweet spot, $\omega_{01}^{ss}$, of $(4.545 \pm 0.005)$ $GHz$. The error on the voltage represents the standard error from the fit, while the maximum error is applied to the qubit frequency. Fig. 4.15b shows the theoretical complete modulation based on the fit data for both resonators and qubit spectroscopy.

A similar investigation was performed for *qubit 2*, as depicted in Fig. 4.16a. The results yield a sweet spot value of $(-1.702 \pm 0.003)$ V and a frequency at the maximum of the modulation, $\omega_{01}^{ss}$, of $(5.650 \pm 0.005)$ GHz. The error on the voltage is the standard error from the fit, and the maximum error is applied to the qubit frequency.

## 4.2.2 Soprano TunC

### Qubit spectroscopy as a function of power

Following the same experimental approach for qubit frequency estimation on the Soprano device, in Fig. 4.17a we show the imaginary part of the demodulated readout voltage output as a function of the qubit drive frequency and the qubit drive power applied across the dedicated drive line for *Q5*, where the *Q5* is at the sweet spot. We can observe both the transition $|0\rangle \longrightarrow |1\rangle$ and $|0\rangle \longrightarrow |2\rangle$. The qubit frequency obtained through qubit spectroscopy is $f_{01} = (5.566 \pm 0.002)$ $GHz$, where the errors are maximum errors. We extrapolate the anharmonicity $\alpha = (-296 \pm 4)$ $MHz$, where the error is a maximum error.

The same investigation was conducted for *Q6*, and is shown in Fig. 4.18a. The readout magnitude of the $S_{21}$ output is shown as a function of the qubit drive frequency and the qubit drive power applied across the dedicated drive line for *Q6*. The qubit frequency $f_{01}$ is $(4.992 \pm 0.002)$ $GHz$ and the anharmonicity is $\alpha = (-325 \pm 4) MHz$., where the errors are the maximum errors.

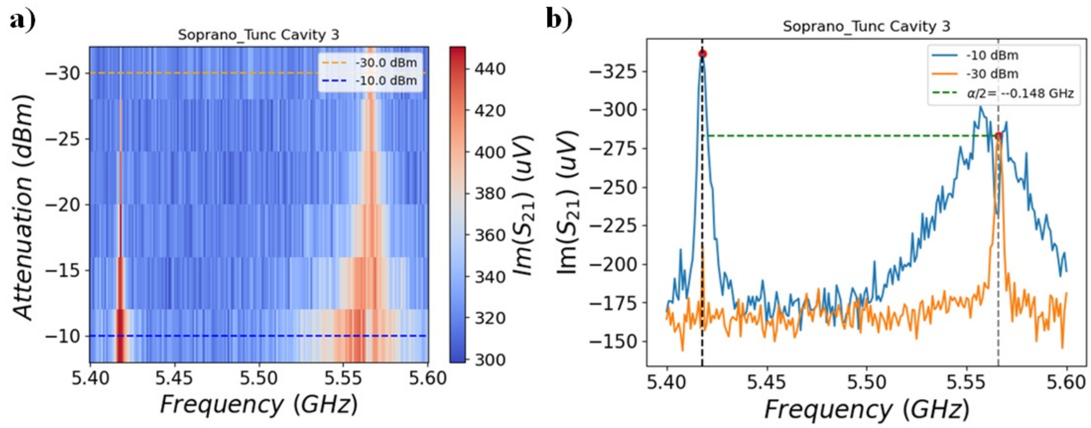


Figure 4.17: *Q5* spectroscopy: in **a)**, the attenuation of the qubit drive signal (y-axis), on the x-axis the qubit drive Q5 frequency, the color scale identifies the imaginary part of the demodulated voltage signal in $\mu V$ of the readout resonator. In **b)** linecuts at -30 dBm (orange) and -10 dBm (blue). The half anharmonicity is also reported (dashed green line).

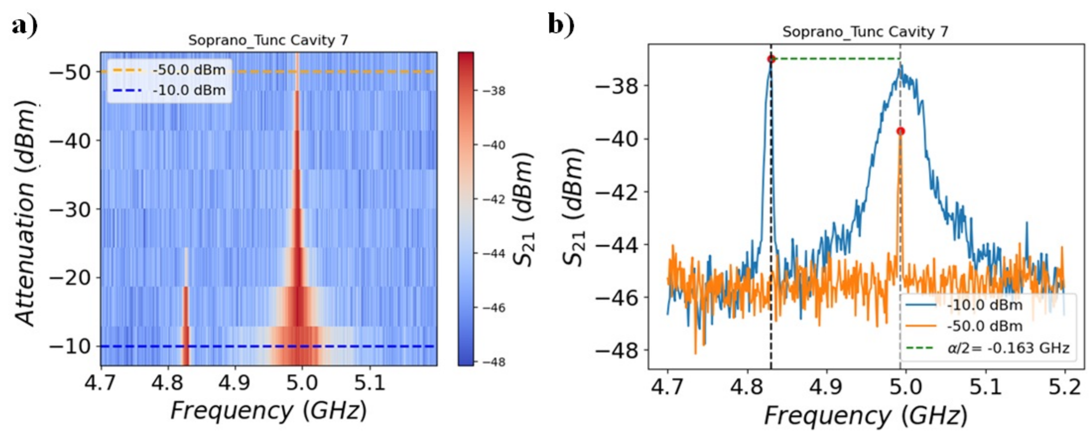


Figure 4.18: *Q6* spectroscopy: in **a)**, the readout magnitude of the $S_{21}$ output as a function of qubit drive frequency and the qubit drive power applied across a dedicated drive line for *Q6*. In **b)** linecuts at -30 dBm (orange) and -10 dBm (blue). The half anharmonicity is also reported (dashed green line).

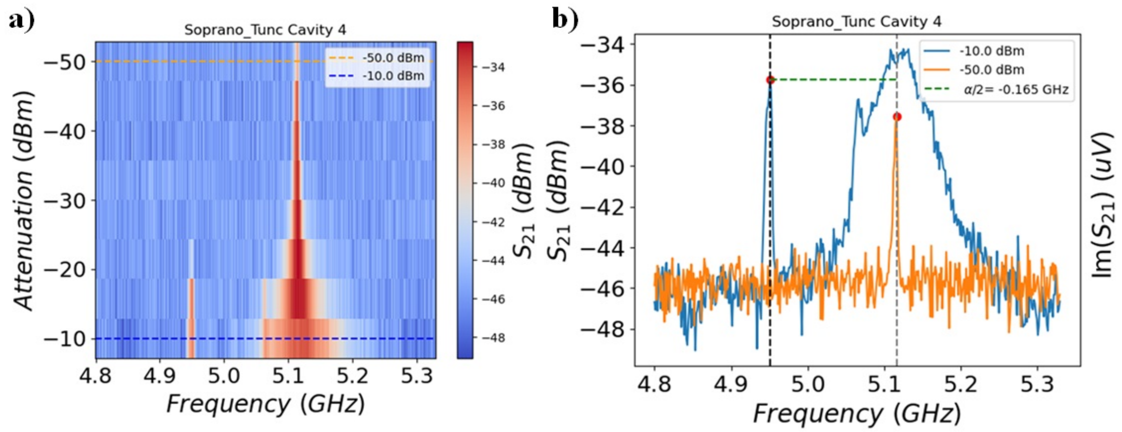


Figure 4.19: *Q7* spectroscopy: in **a)**, the readout magnitude of the $S_{21}$ output as a function of qubit drive frequency and the qubit drive power applied across a dedicated drive line for *Q7*. In **b)** linecuts at -50 dBm (orange) and -10 dBm (blue). The half anharmonicity is also reported (dashed green line).

The color map of qubit spectroscopy for *Q7* is reported in Fig. 4.19a. The qubit frequency $f_{01}$ is $(5.116 \pm 0.002)\ GHz$ and the anharmonicity is $\alpha = (-330 \pm 4)\ MHz$, where the errors are the maximum errors.

Finally, we show the same investigation for *Q8*, at the sweet spot in Fig. 4.20a. The $|0\rangle \rightarrow |1\rangle$ qubit frequency is $(5.298 \pm 0.002)\ \ GHz$, and the anharmonicity is $\alpha = (-306 \pm 4)\ \ MHz$, with maximum errors.

The extrapolated anharmonicities are consistent with each other, in agreement with expectations for qubits fabricated in the same manufacturing process. This consistency also supports the observation of similar power behavior for the pair Q7 and Q8, and pair Q5 and Q6.

**Qubit spectroscopy as a function of flux**

The study in flux of tunable qubits *Q5* and *Q8* is reported in Fig. 4.21 and Fig. 4.22, respectively. The experimental curves were fitted using Eq. A.2 in Appendix A.1. From the theoretical fit we obtain a *sweet spot* value of $(-141 \pm 3)$ mV for Q5 with the frequency value at the sweet spot, $\omega_{01}^{ss}$=(5.566 ± 0.002) GHz, where the error on the voltage is the standard error from the fit, and on the qubit frequency we apply the maximum error. In Fig. 4.21b we show the theoretical complete modulation based on the fit data of both flux modulation of the resonator and the qubit. For *Q8* in Fig. 4.22a, we obtain a sweet spot value of (819 ± 1) mV with the frequency value at the sweet spot $\omega_{01}^{ss}$=(5.329 ± 0.002) GHz, where the error on the voltage is the standard error from the fit, and on the qubit frequency, we apply the maximum error.

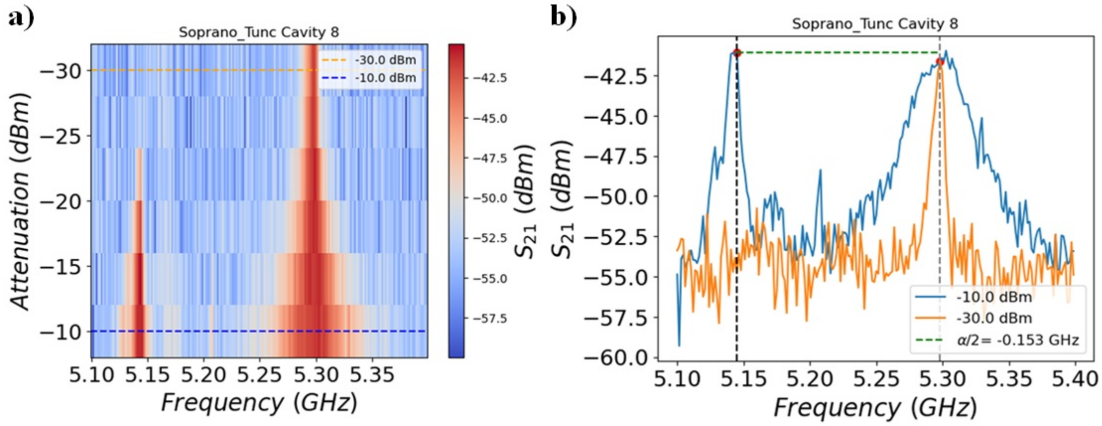


Figure 4.20: *Q8* spectroscopy: in **a)**, the readout magnitude of the $S_{21}$ output as a function of qubit drive frequency and the qubit drive power applied across a dedicated drive line for *Q8*. In **b)** linecuts at -30 dBm (orange) and -10 dBm (blue). The half anharmonicity is also reported (dashed green line).

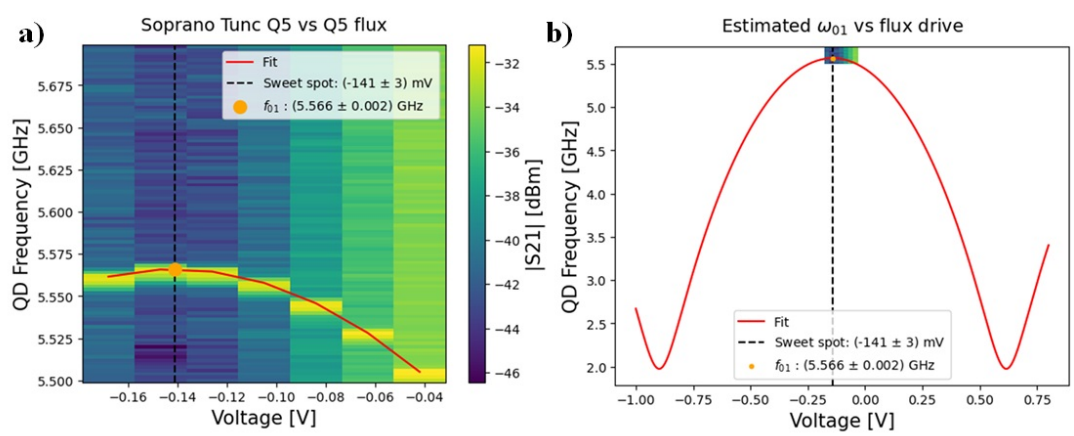


Figure 4.21: Flux spectroscopy of *Q5*. **a)** Colorplot with flux on Q2 in voltage (x-axis), the Q2 drive frequency signal (y-axis), and the color scale the magnitude of the readout resonator. The fit (red curve) is based on Eq. A.2. The dotted line indicates the estimated value for the sweet spot and the maximum modulation value of $\omega_{01}^{ss}$ (orange spot) obtained from the fit. **b)** Extrapolated behavior from the fit, of the qubit frequency $\omega_{01}$ of Q5 vs the drive flux in voltage.

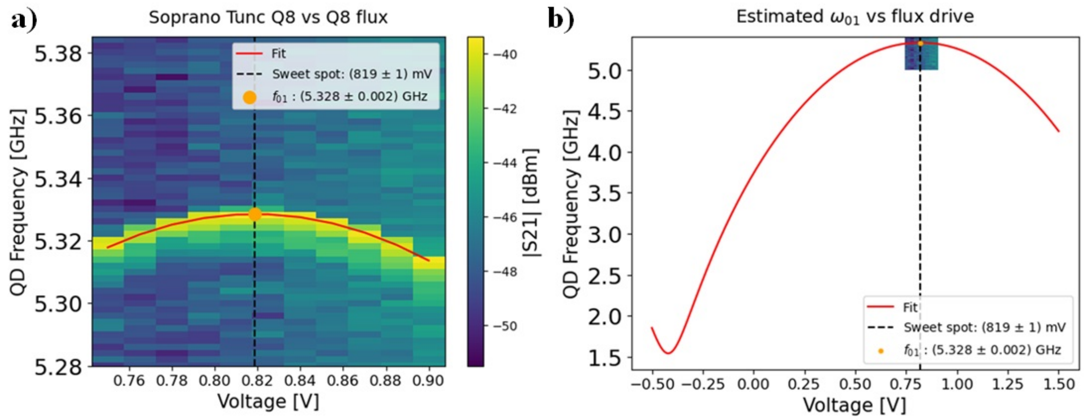


Figure 4.22: Flux spectroscopy of *Q8*. **a)** Colorplot with the flux on Q2 in voltage (x-axis), the Q2 drive frequency signal (y-axis), and the color scale the magnitude of the readout resonator. The fit (red curve) is based on Eq. A.2. The dotted line indicates the estimated value for the sweet spot and the maximum modulation value of $\omega_{01}^{ss}$ (orange spot) obtained from the fit. **b)** Extrapolated behavior from the fit, of the qubit frequency $\omega_{01}$ of Q8 vs the drive flux in voltage.

### 4.2.3 Summary and comparison of qubits electrodynamics parameters

Based on the presented experimental results, we can extract fundamental electrodynamics parameters that have been used for the study and the analysis of two-qubit coupling processes, as well as the fitting of the experimental data for the two devices. In Table 4.23 we compare the characteristics of the two samples obtained by spectroscopy measurements. To calculate the charge energy, we use the approximation $E_C \approx -\alpha$ (Eq. 1.19). The charge energy for the qubits in the two samples analyzed is of the same order of magnitude. Moreover, we calculate $E_J$ from $f_{01}$ by applying Eq. 1.24. From this we are able to calculate the ratio $E_J/E_C$ with a maximum error of ±1, and determine if we are in the low charge noise regime [40]. We observe that all the pairs in the two devices operate within a comparable transmon regime, where the tunable qubits exhibit higher values. This can be justified as, in tunable qubits, $E_J$ will modulate to lower values, and maintaining an adequate $E_J/E_C$ ratio is crucial to protect the qubit against charging noise (Sec. 1.2.3).

## 4.3 Time domain measurements

As outlined in Sec. 2.5 and 2.6.2, time-domain measurements yield extensive insights into the performance of individual and coupled qubits. In this section, we specifically focus on Rabi oscillations, $T_1$ and $T_2$ measurements, with Ramsey interferometry and Hahn echo for both the *Soprano* (Sec. 4.3.1) and the *Soprano TunC* (Sec. 4.3.2) devices. These measurements enable the determination of the $\pi$-pulse, $T_1$, $T_2^*$, and $T_2$. The $\pi$-pulse is pivotal, being it the pulse able to excite the qubit from the ground to the excited state. Therefore, it is a fundamental component for the implementation of the most basic

| Device | Soprano | | Soprano Tunc | | | |
|---|---|---|---|---|---|---|
| Qubit label | Qubit 0 | Qubit 2 | Q5 | Q6 | Q7 | Q8 |
| $f_{01}^{ss}$ (GHz) error | 4.545 $\pm$ 0.005 | 5.650 $\pm$ 0.005 | 5.566 $\pm$0.002 | <u>4.992</u> $\pm$ 0.002 | <u>5.116</u> $\pm$ 0.002 | 5.329 $\pm$0.002 |
| $E_C$ (MHz) error | 268 $\pm$ 4 | 326 $\pm$ 4 | 296 $\pm$ 4 | 325 $\pm$ 4 | 330 $\pm$ 4 | 306 $\pm$ 4 |
| ***Sweet Spot*** (V) error | 1.307 $\pm$ 0.004 | −1.702 $\pm$ 0.003 | −0.141 $\pm$ 0.003 | | | 0.819 $\pm$ 0.001 |
| $E_J$ (GHz) error | 10.80 $\pm$ 0.01 | 13.70 $\pm$ 0.01 | 14.51 $\pm$ 0.01 | 10.87 $\pm$ 0.01 | 11.23 $\pm$ 0.01 | 12.97 $\pm$ 0.01 |
| $E_J/E_C$ error | 40 $\pm$ 1 | 42 $\pm$ 1 | 49 $\pm$ 1 | 33 $\pm$ 1 | 34 $\pm$ 1 | 42 $\pm$ 1 |

Table 4.23: Summary of values obtained for both the devices *Soprano* and *Soprano TunC*. For each qubit, it shows the values obtained from the fit (see Appendix A.1) for the frequency $|0\rangle \rightarrow |1\rangle$ transition at *sweet spot* ($f_{01}^{ss}$) and the value of the sweet spot, with the error given by the maximum error and the standard error from the fit, respectively. For the fixed qubits Q6 and Q7, values from the spectroscopy measurement (underlined) are reported. The charge energy ($E_C$) obtained from the spectroscopy measurements in power, Josephson energies calculated by the Eq. 1.24 and the corresponding ratio $E_J/E_C$ are also reported, with the errors given by the maximum errors.

characterization sequences. The relaxation and coherence times are instead crucial to evaluate the maximum coherence of the qubits [69]. Specifically, the relaxation time is here the main comparison parameter for the two designs. Indeed, on one hand, the coherence time depends on the intrinsic noise sources related to the circuital design (e.g. flux noise). On the other, it is sensitive to room-temperature electronics fluctuations and the quality of the pulses in the characterization sequences [14]. The relaxation time, instead, is mostly influenced by materials into play (e.g. dielectric losses, defects, quasiparticles) and the coupling with readout resonators and flux/control lines on chip (e.g. Purcell effect, spontaneous radiation emission) [34]. The two devices have been fabricated within the same materials and fabrication conditions, as well as with similar readout and lines couplings. Therefore, relaxation times can be compared in order to extract information on the quality of the materials and the design. Coherence times, instead, have been measured in different experimental conditions (different cooldowns), thus preventing a direct comparison.

### 4.3.1 Soprano

**Rabi oscillation**. Following the procedure discussed in Sec. 2.6.2, we study the Rabi oscillation for the pair qubit 0 and qubit 2 of the Soprano device. The Chevron plot in Fig. 4.24 shows that the Rabi oscillation frequency for qubit 2 increases, while the amplitude decreases, when we change the frequency of the qubit drive (QD) pulse. This measurement

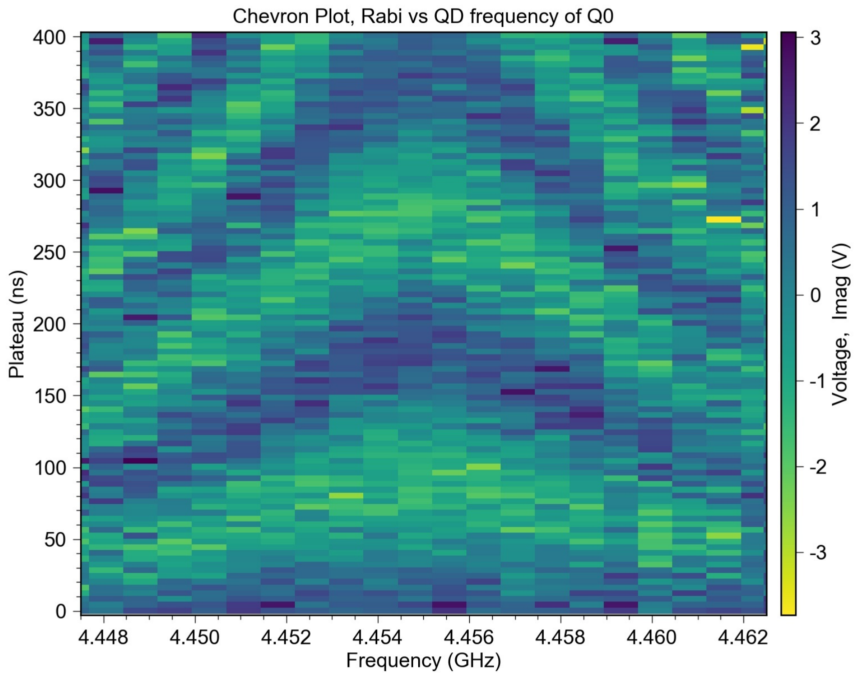


Figure 4.24: Chevron plot for qubit 0: colorplot with the Qubit Drive frequency on the x-axis , and the pulse time on the y-axis. The color scale is the imaginary part of the readout resonator signal. A 107 MHz sideband should be added to the frequency values shown due to up-conversion processes (Sec. 2.5).

allows us to find the frequency of the QD resonant with the qubit as the center of the Chevron plot, and it is (4.562 ± 0.001) GHz. The same investigation was performed for qubit 2 and the frequency resonant with the qubit is (5.593 ± 0.001) GHz. These frequency values are consistent with the $f_{01}$ frequency peaks observed in spectroscopy experiments (Table 4.23).

As discussed in Sec. 2.6.2, once the resonant frequency has been detected, we change the attenuation on the drive to estimate the $\pi$-pulse. In order to perform gates, we want a $\pi$-pulse that is as fast as possible. In Fig. 4.25a is shown the result of the Rabi oscillation measurement for qubit 0, with an attenuation on the drive line of 18 dB. For the estimation of $\pi$-pulse we fit the data with a sine function [4] and the duration of the QD pulse for the transition $|0\rangle \longrightarrow |1\rangle$ is (55 ± 1) *ns*, where the error is the maximum error. We have performed the same measurements for qubit 2, and the results are shown in Fig. 4.25b. An attenuation on the drive line of 15 dB was employed and the $\pi$-pulse duration from the fit result (20 ± 1) *ns*, where the error is the maximum error. We observe that the $\pi$-pulse duration for qubit 2 is shorter than that for qubit 0, a result consistent with expectations, as the Rabi oscillation frequency is known to increase with increased power according to [69]:

$$\Omega_r = \sqrt{A^2 + \delta\omega}, \tag{4.1}$$

where A is the amplitude of the RF signal and $\delta\omega$ is the detuning between the drive and the qubit frequency.

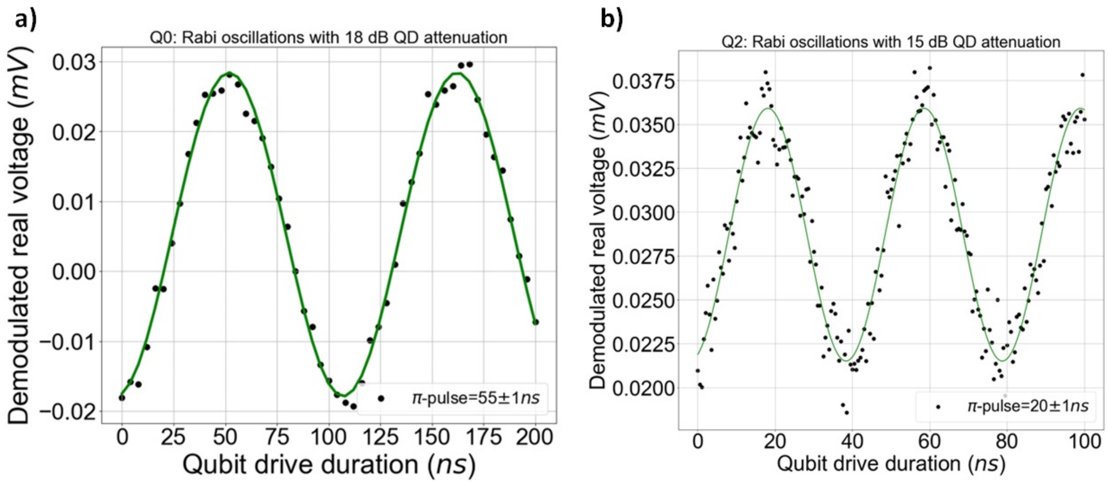


Figure 4.25: $\pi$-pulse fitting, for qubit 0**a)** and qubit 2 **b)**, respectively.

**Relaxation time**. The protocol for $T_1$ measurements, discussed in Sec. 2.6.2, was implemented for qubits 0 and 2. $T_1$ quantifies the relaxation time from the excited state to the ground state (Sec 1.2.4). For qubit 0, we obtain the result in Fig. 4.26a. We fit the data (blue dots in Fig. 4.26a) with Eq. 2.6 and obtain the characteristic decay time $T_1 = (16 \pm 2)$ $\mu s$, where the error is the standard error from the fit.

In Fig. 4.26b is shown the same measurement for qubit 2. From the exponential fit, we are able to extract $T_1 = (7.6 \pm 0.8)$ $\mu s$, where the error is the standard error from the fit. These results are in agreement with $T_1$ times typically found in literature [14].

**Decoherence time**. As discussed in Sec. 2.6.2, the Ramsey protocol allows to estimate the decoherence time $T_2$ and is also sensitive to the detuning $\delta\omega$ between the drive and the qubit frequency, so it can be used to evaluate the frequency of the qubit. According to Eq. 2.7, when the frequency of the drive is on resonance with the qubit frequency, i.e. $\delta\omega = 0$, the expected behavior is an exponential. In order to find the qubit frequency, we perform the Ramsey protocol as a function of the QD frequency. This results in the Ramsey fringes in Fig. 4.27a for qubit 0. In Fig. 4.27b the Ramsey fringes on and off-resonance are shown. In order to determine the frequency of qubit 0 we select the frequency with the longer oscillation period, resulting in $\omega_{Q0} = (4.5618 \pm 0.0001)$ $GHz$, where the error is maximum.

Moreover, as we introduced in the Sec. 2.6.2, the Ramsey interferometry allows to estimate the Ramsey Decoherence time $T_2^*$, which contains information on both energy relaxation and pure dephasing [69]. To include a higher degree of dephasing it is typically performed off-resonance, and the the data is fitted using Eq. 2.7. The off-resonance measurement in Fig. 4.28a gives a $T_2^* = (1.9 \pm 0.2)$ $\mu s$, where the error is the standard error from the fit. The same investigation on qubit 2 is shown in Fig. 4.28b, and gives a $T_2^* = (1.3 \pm 0.2)$ $\mu s$, where the error is the standard error.

**Hahn echo measure**. To obtain $T_2$, in which the effect of dephasing is mitigated, we employ the *Hahn echo* protocol, as introduced in Sec. 2.6.2. This mitigation is achieved

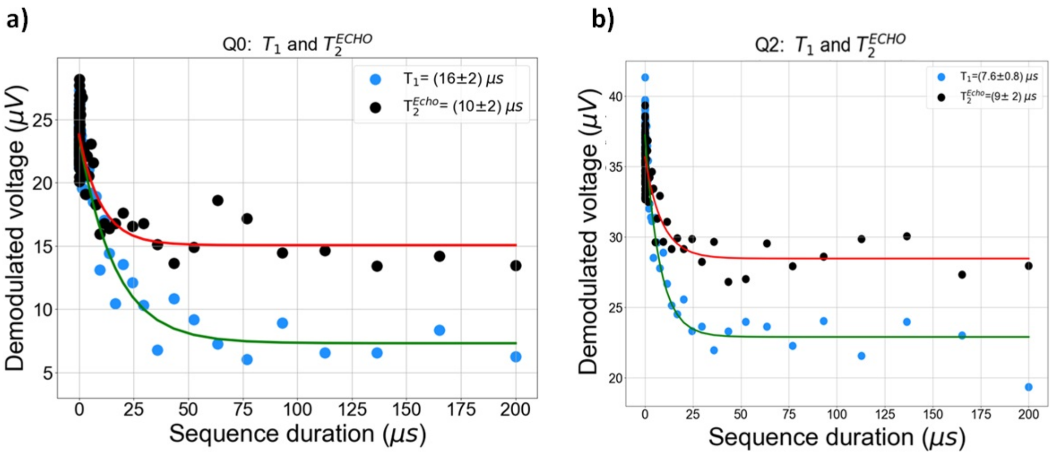


Figure 4.26: $T_1$ measurement for qubit 0 (blue dots in panel-**a**) and qubit 2 (blue dots in panel-**b**): demodulated voltage output as a function of the sequence duration has been fitted with the Eq. 2.6 (green line). Hahn echo measurement for $T_2$ performed both for qubit 0 (black dots in panel-**a**) and qubit 2 (black dots in panel-**b**). We plot the real part of the demodulated output voltage signal as a function of the sequence duration. The red line is the fit given by Eq. 2.8.

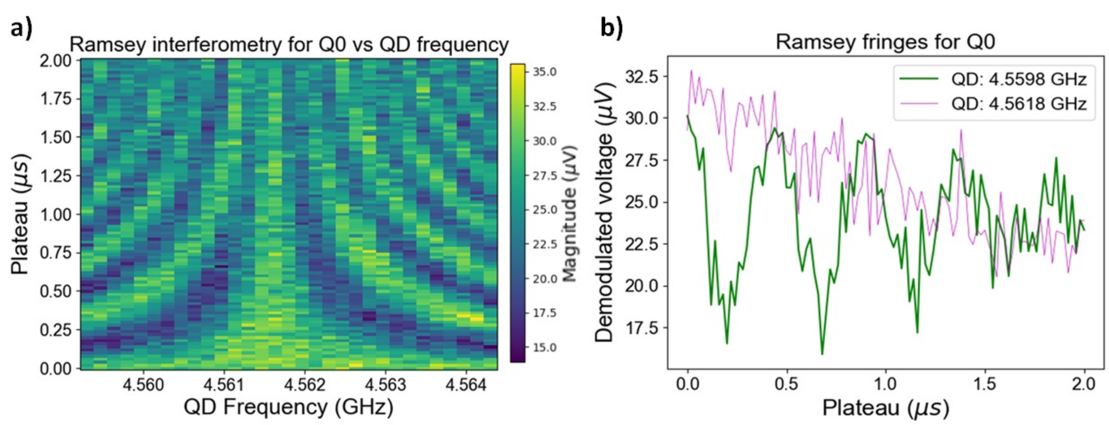


Figure 4.27: In **a)** Ramsey fringes for qubit 0: colorplot with x-axis the pulse duration, y-axis the Qubit Drive frequency and color scale the magnitude of the readout resonator. In **b)** line-cuts of the colorplot for fixed Qubit Drive frequencies on-resonance (pink) and off-resonance (green).

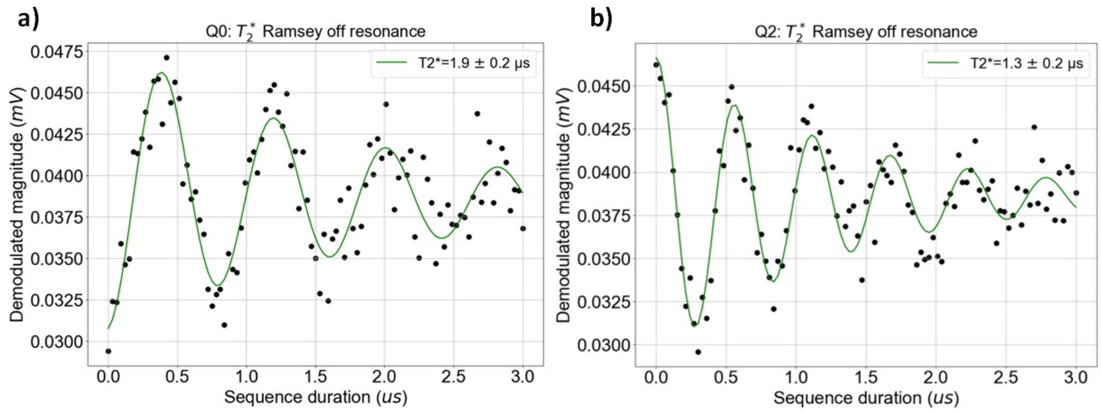


Figure 4.28: Measure of the off-resonance Ramsey oscillation to estimate $T_2^*$ both for qubit 0 (panel-**a**) and qubit 2 (panel-**b**). The data are fitted using Eq. 2.7.

through a refocusing pulse, which counterbalances the dephasing on the equatorial plane.

In Fig. 4.26**a** and **b** the result of Hahn echo measurement (black dots) are shown for qubit 0 and qubit 2 respectively. Employing the protocol detailed in Sec. 2.6.2, we estimate $T_2$ by fitting the data with Eq. 2.8. The acquired $T_2$ value for qubit 0 is $(10 \pm 2)\mu s$, and for qubit 2, it is $(9 \pm 2)\mu s$, with both errors being standard errors.

These values are lower than the ideal limit of zero dephasing, i.e. for a $T_2$ approximately twice $T_1$ [14]. This type of measurement is mainly influenced by the accuracy of the measurement and the experimental setup, while the $T_1$ values are indicative of the design and are in line with the expected values [4]. Nevertheless, $T_2$ times are larger than $T_2^*$ values, thus confirming that the Hahn-Echo protocol has been able to suppress low-frequency dephasing effects.

### 4.3.2 Soprano TunC

Following the same experimental approach seen for the *Soprano* device, we now present the results of time-domain measurements on the *Soprano TunC* device, for the pairs Q5-Q6 and Q7-Q8. In particular, we show the results for Q7, Q5 and Q6. The data are compared with the results obtained for the *Soprano*, and summarized in Table 4.35.

**Rabi oscillation**. In Fig. 4.29a we show the Rabi oscillation for Q7 as a function of the QD frequency. At zero detuning we expect the maximum of the period of the Rabi oscillations [4]. This measurement allows us to find the QD frequency resonant with the qubit frequency, as depicted in Fig. 4.29b, i.e. $(5.117 \pm 0.001)$ GHz.

The same investigation was performed for Q5 and is shown in Fig. 4.30a , where the QD frequency resonant with the qubit is $(5.567 \pm 0.001)$ GHz (Fig. 4.30b). These values are consistent within the errors with the frequency values obtained from spectroscopy experiments (Table 4.23).

As discussed for the *Soprano* device, once the resonant frequency has been detected, the attenuation on the drive has been varied to estimate the $\pi$-pulse. In Fig. 4.31a we set

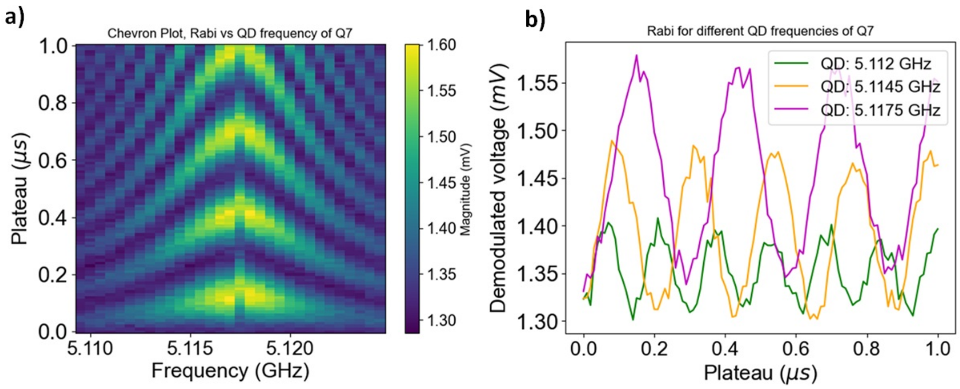


Figure 4.29: In **a)** Chevron plot for Q7, with the Qubit Drive frequency (x-axis), the pulse time (y-axis) and the color scale is the magnitude of the demodulated voltage output. In **b)** behavior of the Rabi oscillation when changing the detuning between the Qubit Drive pulse and the Q7 frequency for selected QD frequencies.

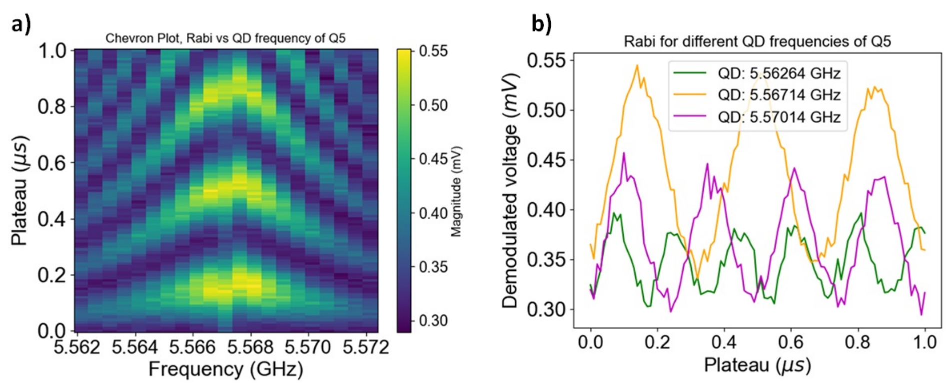


Figure 4.30: In **a)** Chevron plot for Q5, with the Qubit Drive frequency on the x-axis, the pulse time on the y-axis. The color scale is the magnitude of the demodulated voltage output. In **b)** behavior of the Rabi oscillation when changing the detuning between the Qubit Drive pulse and the Q5 frequency for selected QD frequencies.

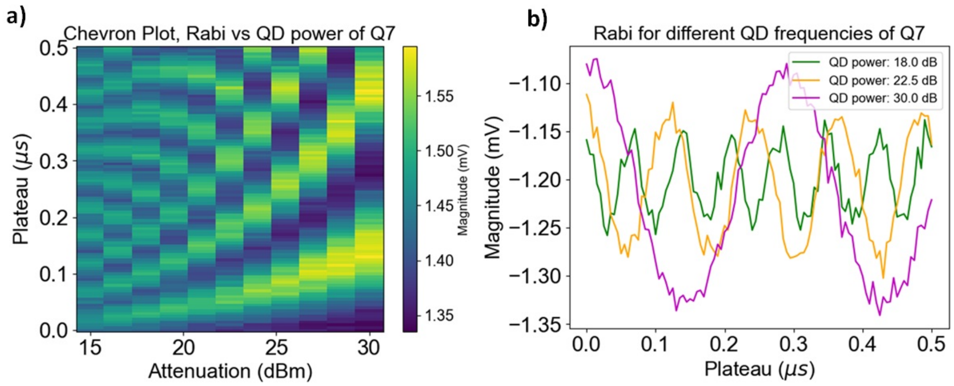


Figure 4.31: Chevron plot for Q7 as a function of the QD power: the x-axis represents the Qubit Drive attenuation, the y-axis the pulse time of the drive signal and the color scale the magnitude of the demodulated voltage output. In **b)** the behavior of Rabi oscillation when changing the attenuation on the Qubit Drive pulse for selected values.

QD frequency to the Chevron plot center in Fig. 4.29a and we vary the attenuation on the QD. In agreement with Eq. 4.1 increasing the QD power leads to faster Rabi oscillations, as shown in Fig. 4.31b. In Fig. 4.32a, we show the result of the Rabi oscillation measurement for Q7, with attenuation on the drive line of 30 dB. As seen for the *Soprano* device, for the estimation of $\pi$-pulse we fit the data with the sine function and result $(143 \pm 1)$ $ns$, where the error is the standard error from the fit. We have performed the same measurements for Q5 and the results are shown in Fig. 4.32b. An attenuation on the drive line of 30 dB gives a $\pi$-pulse duration of $(175 \pm 1)$ $ns$, where the error is the standard error from the fit.

**Relaxation time**. For $T_1$ measurements we implement the same protocol seen for the *Soprano* device. For Q7 we obtain the result in Fig. 4.33a. We fit the data (blue dots in Fig. 4.33a) with Eq. 2.6 and obtain the characteristic decay time $T_1 = (4.7 \pm 0.4)$ $\mu s$, where the error is the standard error from the fit. In Fig. 4.33b is shown the same measurement for Q5. From the exponential fit, we are able to extract $T_1 = (9.9 \pm 0.5)$ $\mu s$, where the error is the standard error from the fit.

**Decoherence time**. As discussed for the *Soprano* device, an important result is the *Ramsey Decoherence time* $T_2^*$ measurement. The result of the off-resonance measurement is shown in Fig. 4.34a for Q5, and from the fit we obtain $T_2^* = (12.6 \pm 0.3)$ $\mu s$, where the error is the standard error from the fit. As one can notice from Fig. 4.34a, the Ramsey off-resonance oscillation shows a positive drift increasing the sequence duration. This must be related to the fact that drive pulses have not been optimized in these preliminary experiments. This is also consistent with the presence of a Gaussian broadening of the $T_2^{ECHO}$ measurement for Q7 in Fig. 4.33a [4]. Therefore, we have not performed any Ramsey experiment on Q7, being necessary to perform an optimization procedure on the control pulses, which is not the main goal of this work.

**Hahn echo measure**. To obtain $T_2$, we employ the *Hahn echo* protocol, as discussed for the *Soprano* device. In Fig. 4.33a is shown the result (black dots) for Q7. Employing the protocol detailed in Sec. 2.6.2, by fitting the data we estimate $T_2 = (2 \pm 1)\mu s$, where the

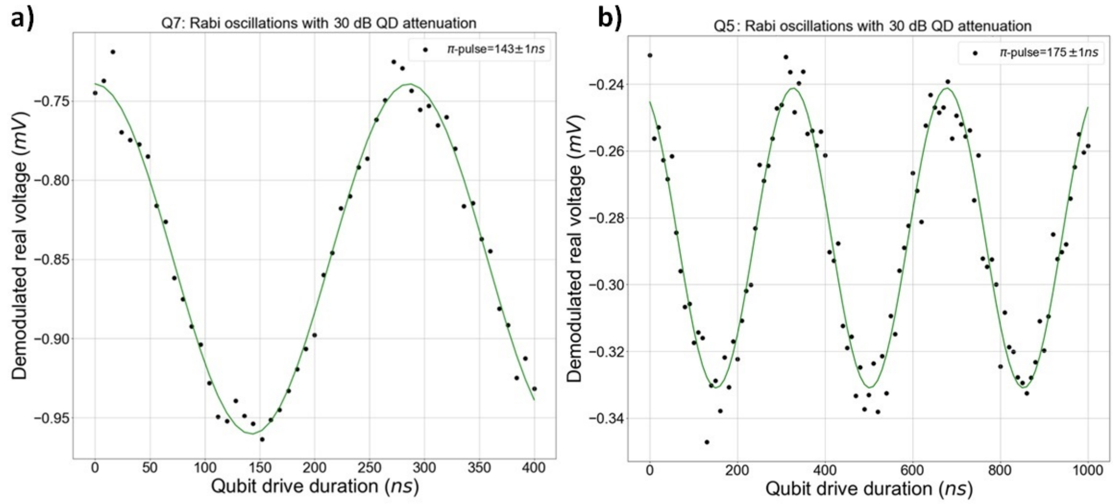


Figure 4.32: Measure of the Rabi oscillation to estimate the $\pi$-pulse using the sine function, for Q7 (panel-**a**) and Q5 (panel-**b**) respectively.

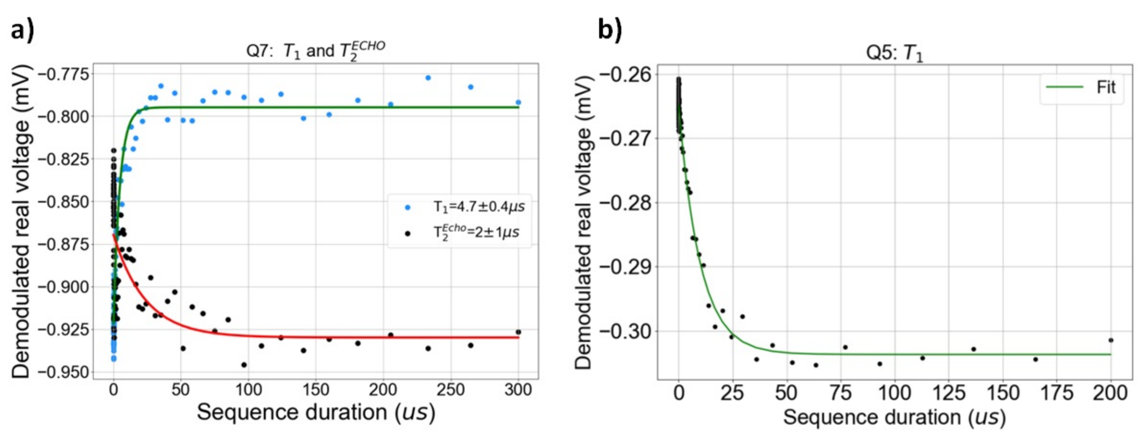


Figure 4.33: In **a)** the $T_1$ and $T_2^{ECHO}$ measurement (blue and black dots, respectively) for Q7. The demodulated voltage output as a function of the sequence duration has been fitted with the Eq. 2.6 (green curve) for T1 estimation, while Hahn echo $T_2$ time has been fitted using Eq. 2.8 (red curve). In **b)** the $T_1$ measurement (black dots) for Q5, fitted with the Eq. 2.6 (green curve).

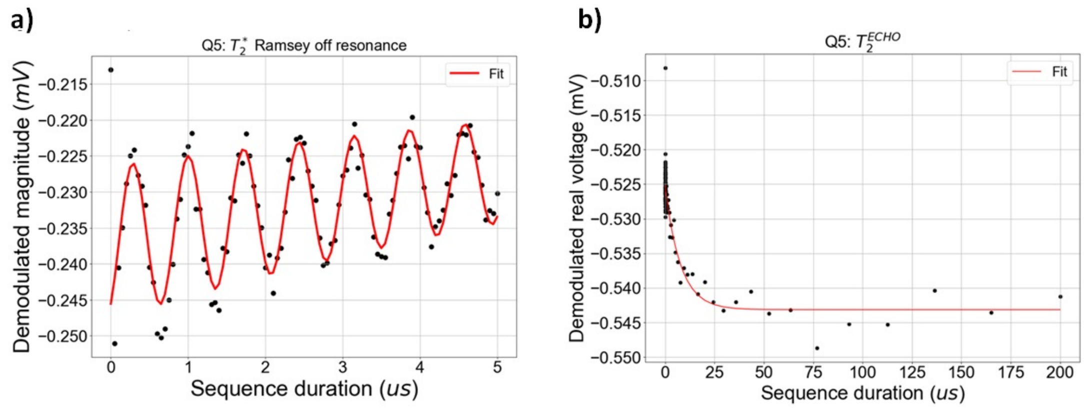


Figure 4.34: In **a)** measure of the off-resonance Ramsey oscillation to estimate $T_2^*$ for Q5. The data was fitted using Eq. 2.7. In **b)** *Hahn echo* measurement for $T_2$ performed Q5. We plot the real part of the demodulated output voltage signal as a function of the sequence duration. The red line is the fit given by Eq. 2.8.

| **Device** | **Soprano** | | **Soprano Tunc** | | |
|---|---|---|---|---|---|
| Qubit label | Qubit 0 | Qubit 2 | Q5 | Q6 | Q7 |
| $T_1$ (µs) | 16 ± 2 | 7.6 ± 0.8 | 9.9 ± 0.5 | 14.6 ± 0.5 | 4.7 ± 0.4 |
| $T_2$ (µs) | 10 ± 2 | 9 ± 2 | 7 ± 1 | 1.6 ± 0.3 | 2 ± 1 |
| $T_2^*$ (µs) | 1.9 ± 0.2 | 1.3 ± 0.2 | 12.6 ± 0.3 | 2.2 ± 0.1 | |
| π-pulse (ns) | (55 ± 1) @18dB | (20 ± 1) @15dB | 175 ± 1 @30dB | 65 ± 1 @24dB | 143± 1 @30dB |

Table 4.35: Summary of values obtained for both the devices *Soprano* and *Soprano TunC*. For each qubit, we report the *Relaxation time* ($T_1$), *Hahn-echo time* ($T_2$), the Ramsey *Decoherence time* ($T_2^*$) and the $\pi$-pulse. For each value of the $\pi$-pulse we report the power to which it was measured.

error is the standard error. The same investigation was conducted for Q5 and is shown in Fig. 4.34b. We obtain a $T_2 = (7 \pm 1)\mu s$, where the error is the standard error.

### 4.3.3 Summary for the relaxation times and design implications

Both designs exhibit values that are comparable and consistent with those available in literature [14][4]. Specifically, the values of $T_2$ and $T_2^*$ are predominantly influenced by the precision of the measurement and the experimental setup, and thus, are not indicative for this comparison. The $T_1$ values, however, are representative of the design quality and are coherent across both designs. The *Soprano* device, characterized by a more stable design, features relaxation times of the order of tens of microseconds. The relaxation time for Q2 is lower than the relaxation time estimated for Q0. This is related to the fact that Q2 has the maximum connectivity on chip, being it connected through high-frequency bus resonators to the other qubits of the matrix (Sec. 2.3). The relaxation times measured for the *Soprano TunC* are also consistent with Qubit 2 relaxation time. Indeed, the presence of an increased number of control and flux lines, as well as readout resonators in this prototypal device cause an increased coupling with the external environment, which in turn induces spontaneous radiation emission and relaxation. At the same time, this affects mostly Q7, rather than Q6. Since they are both fixed-transmon qubits, we can exclude that relaxation is caused by the flux lines. However, Q7 shares with Q8 a tunable coupler with a test readout resonator. Reasonably, the low relaxation time must be related to the spontaneous radiation emission/adsorption through TC78 readout resonator.

## 4.4 Experimental analysis and comparison of different coupling schemes

For the implementation of two-qubit gate operations discussed in Chapter 3, it is necessary to couple at least two qubits by bringing them into resonance. For both the investigated devices, *Soprano* and *Soprano TunC*, this was obtained by tuning in flux the qubit at the highest frequency in the pair, to the lowest one in frequency. At the resonance flux point, the presence of coupling interaction opens a gap in the energy spectrum of the coupled qubits system, i.e. an *avoided level-crossing* occurs, as discussed in Sec 3.1. In this section, we present the results of avoided level crossing (ALC) measurements performed on both devices. In particular, these results have been achieved by simulating the energy spectrum with an approach that aims at reproducing the physics of the system even beyond the commonly used perturbative hypotheses (Refs. [85], [76], [86]). As detailed in the Appendix A.2, this method employs a numerical diagonalization of the Hamiltonian, allowing us to extract detailed information about the interaction strengths within the system.

In order to benchmark the feasibility of this approach, we first study a simpler system, such as the *Soprano*, in which two qubits are coupled through a resonator. Then, we focus on the *Soprano TunC* device, which is a more complex system, consisting of three qubits, with the third central acting as Coupler (Sec. 3.2).

### 4.4.1 Soprano: coupling through high-frequency bus resonators

In Fig. 4.36 the ALC measurement between qubit 0 and qubit 2 is shown. We perform a spectroscopy on qubit 0 while sweeping the flux on qubit 2 and we observe the spectrum of the dressed eigenstates $|01\rangle$ and $|10\rangle$ at $(0.278 \pm 0.001)$ flux quanta of the qubit 2 flux. Qubit 0 is kept at the flux $0.086\ \Phi/\Phi_0$ and a drive attenuation of 26 dBm on the drive tone was used. The reason is that, in order to perform the spectroscopy measurement on qubit 0, we must make the $|0\rangle \rightarrow |1\rangle$ transition occur, by sending an appropriate QD pulse.

From this measurement, we can extract the flux on qubit 2 that will allow to put on resonance qubit 0 and qubit 2, and therefore implement two-qubit gates, like the iSWAP described in Sec. 3.3. Further, in order to extract the strength of the coupling between qubit 0 and qubit 2, we use two different approaches and then compare the results.

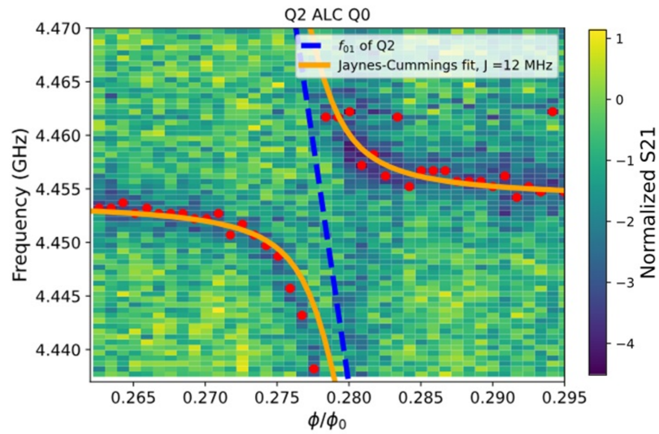


Figure 4.36: Avoided level crossing for Qubits 0 and 2: on the x-axis the applied flux on qubit 2 in flux quanta, on the y-axis the qubit frequency of qubit 0 and the color scale is the normalized magnitude in a.u. of the readout resonator. The orange curves represent the dressed states $|01\rangle$ and $|10\rangle$ of the two-qubit system. They are obtained by fitting the avoided level crossing with Eq. 4.2. In dashed blue the $f_{01}$ for the bare state of qubit 2.

In the former, we used an established model in the literature that refers to Hamiltonian 3.2 obtained in the dispersive regime [76][86]. As reported in the reference [76], its diagonalization leads to:

$$f_{01}(\omega_1, \omega_2, J) = \frac{(\omega_1 + \omega_2) \pm \sqrt{(\omega_1 - \omega_2)^2 + 4J^2}}{2}, \tag{4.2}$$

where J is is the strength of the effective interaction in Eq. 3.2.

In Fig. 4.36, the best-fit result on the experimental data indicates an interaction strength of $J = (12 \pm 2)\ MHz$, where the errors are maximum errors. Since the *Soprano* device follows a standard design as discussed in Sec. 2.3, this value aligns with the reference value of 10 MHz found in the literature [87], making them compatible within the margin of error.

We employ an innovative model that refers to Hamiltonian 3.1 to extract complete information on the actual qubit resonator interactions, out of the dispersive regime hypothesis. In order to simulate the complete Hamiltonian, we employ the Python package for superconducting qubits *scQubits* [88], based on the characteristic parameters obtained from the spectroscopy measurements summarized in Table 4.23 (refer to Appendix A.2 for details).

As we discussed in Sec. 3.2 for the *Soprano* device, qubit 0 and qubit 2 interact with a resonator mode, each with distinct interaction strengths $g_{1r}$ and $g_{2r}$. In Fig. 4.37a it is shown the fit of the experimental curve with the simulated curve. The values of the strength interaction are $g_{1r} = (407 \pm 5) MHz$ for the *qubit 2* and $g_{2r} = (514 \pm 5) MHz$ for the *qubit 0*, respectively, with the resonator mode, where the error is the maximum error on the best fit. From Eq. 3.3, we obtain a value of the effective strength interaction of $J = (10 \pm 2)\ MHz$, where the error is the maximum error. The values we derived for

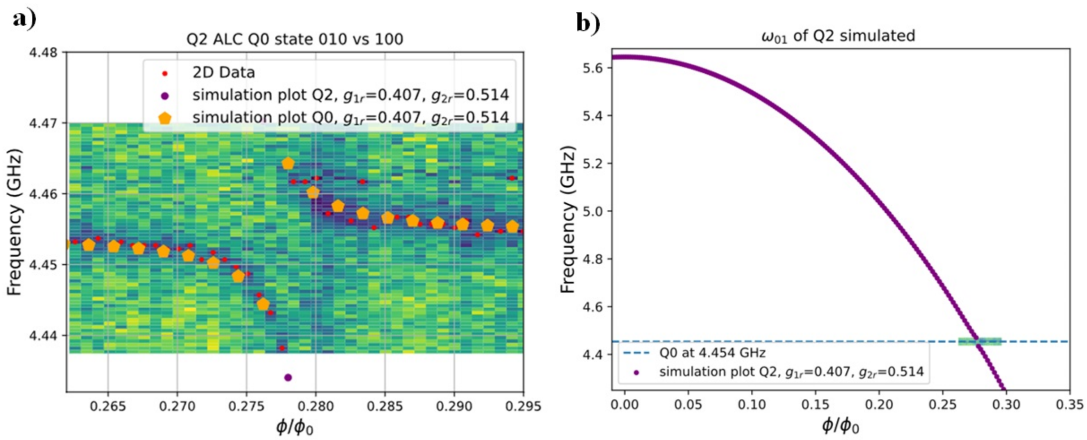


Figure 4.37: In **a)** avoided level crossing for *Qubits* 0 and 2: on the x-axis the applied flux on *Qubit* 2 in flux quanta, on the y-axis the Qubit frequency of *Qubit* 2 and the color scale is the normalized magnitude in a.u. of the readout resonator. The orange dots are the simulation plot for the state $|010\rangle$ (qubit 0) and in purple the state $|100\rangle$ (qubit 2). Here the notation $|Q2, Q0, Resonator\rangle$ is employed (see Appendix A.2) for details. In **b)** the plot of the state $|100\rangle$ (qubit 2) on a larger flux range.

the effective interaction, both from the conventional analytical perturbative model and from the direct evaluation of the interaction strengths of the complete Hamiltonian, are consistent within their error. This agreement highlights our ability to extract values for the interaction terms of the non-perturbative Hamiltonian, further supporting the validity of the model we've introduced.

### 4.4.2 Soprano TunC: tunable coupling scheme

In order to implement multi-qubit gate operations with tunable couplers such as the *Soprano TunC* device described in Sec. 2.3, a spectroscopy study of the ALC measurements is essential to understand the coupling behavior and flux ranges of modulation for the Coupler. Similar to the *Soprano* device, we perform the spectroscopy on *Q7* with a drive attenuation of 40 dBm, while sweeping the flux on *Coupler* 78, keeping the *Q8* far detuned at 0.0406 $\Phi/\Phi_0$ and we observe the ALC occurring at $(0.360 \pm 1)$ flux quanta of the *Coupler 78* flux, see Fig. 4.38a.

In order to extract the strength of the coupling between qubit-Coupler ($g_{i,r}$) and qubit-qubit ($g_{12}$) we employ a model that refers to the Hamiltonian 3.4. The simulation is based on the characteristic parameters summarized in Table 4.23, and employ the Python package for superconducting qubits *scQubits* [88] (refer to Appendix A.2 for details).

In Fig. 4.38a it is shown the fit of the experimental curve with the simulated curve. The values of the strength interaction are $g_{1c} = (42 \pm 2)$ *MHz* for the *Q7-Coupler*, $g_{2r} = (28 \pm 2)$ *MHz* for the *Q8-Coupler*, and $g_{12} = (15 \pm 2)$ *MHz* for the *Q7-Q8*, where the error is the maximum error.

The same investigation was conducted for the *Q8* with a drive attenuation of 40 dBm while sweeping the flux on *Coupler* 78 and keeping the *Q8* at 0.0406 $\Phi/\Phi_0$. In Fig.

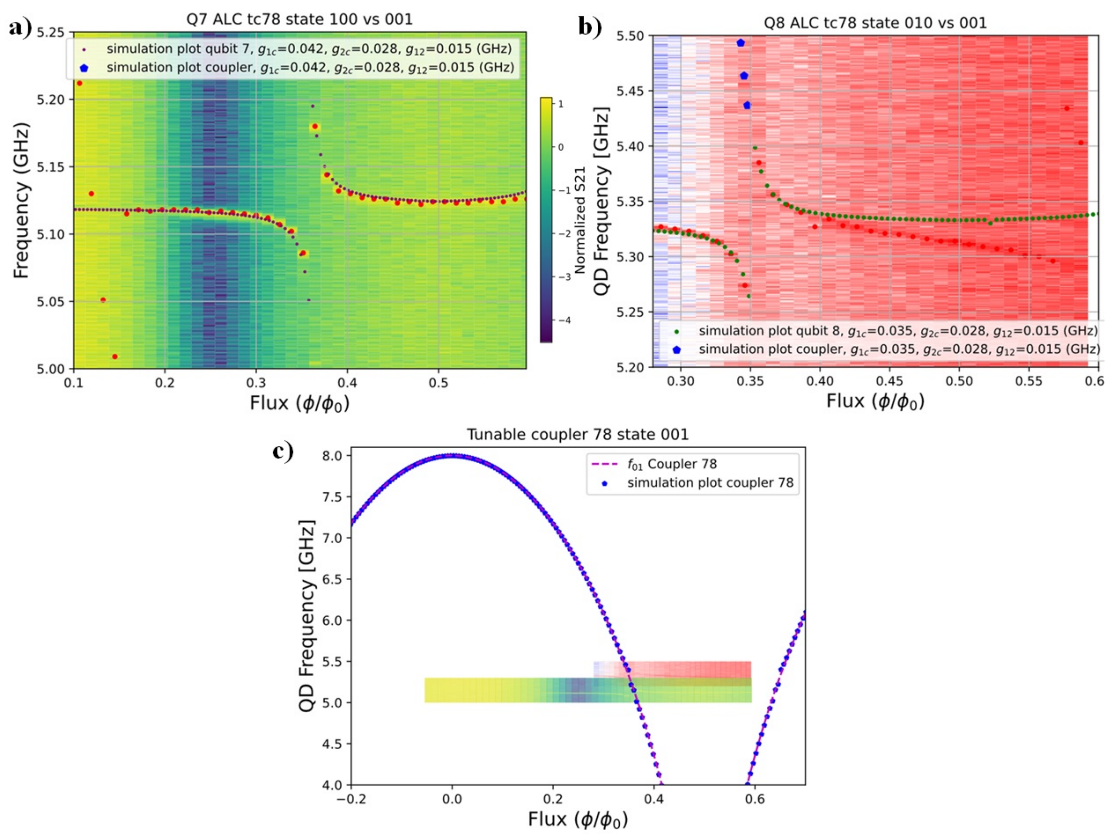


Figure 4.38: In **a)** avoided level crossing for *Q7* and *Coupler 78*: on the x-axis the applied flux on *Coupler 78* in flux quanta, on the y-axis the *Q7* frequency and the color scale is the normalized magnitude in a.u. of the readout resonator. The purple dots are the simulation of the state $|100\rangle$ (Q7) and in blue the state $|001\rangle$ (Coupler 78). Here the notation $|Q7, Q8, Coupler78\rangle$ is employed (see Appendix A.2 for details). In **b)** avoided level crossing for *Q8* and *Coupler 78*: on the x-axis the applied flux on *Coupler 78* in flux quanta, on the y-axis the *Q8* frequency and the color scale is the normalized magnitude in a.u. of the readout resonator. The green dots are the simulation plot for the state $|010\rangle$ (Q8) and in blue the state $|001\rangle$ (Coupler 78). In **c)** the plot of the state $|001\rangle$ (Coupler 78) on a larger flux range. We see that the coupler first crosses at a higher frequency the Q8 and at a lower frequency Q7. The color plots in panels **a)** and **b)** are also shown in the figure as a reference.

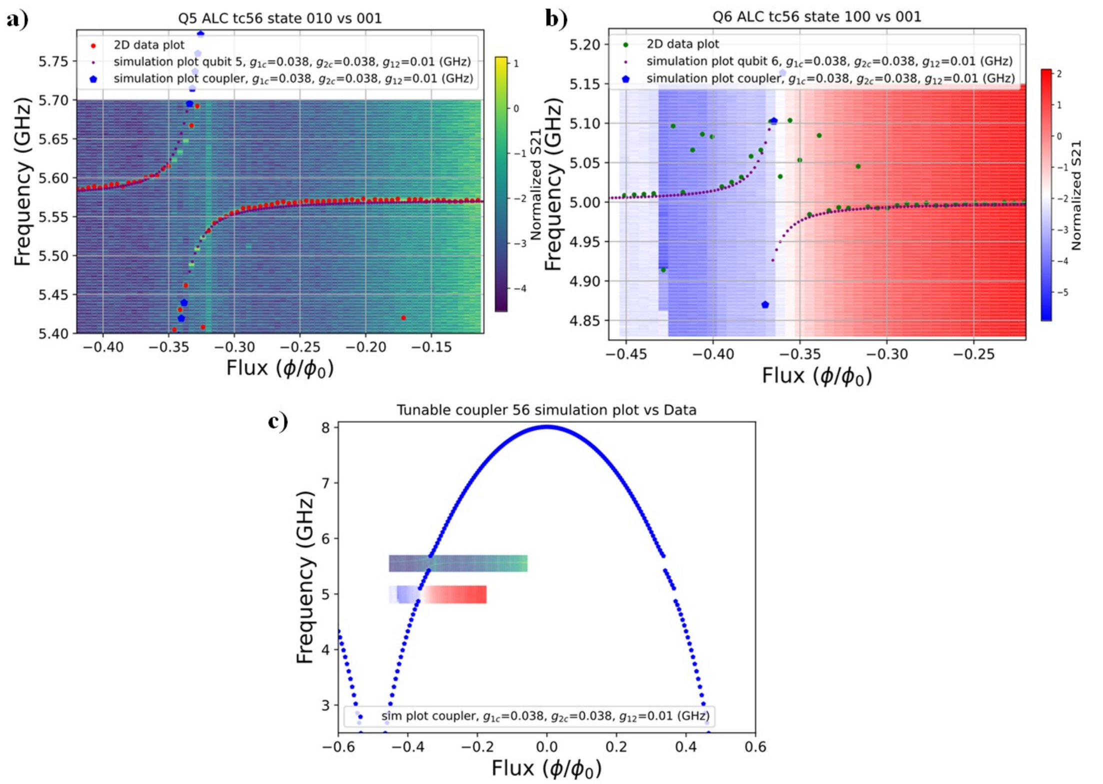


Figure 4.39: In **a)** avoided level crossing for *Qubits* 5 and *Coupler 56*: on the x-axis the applied flux on *Coupler 56* in flux quanta, on the y-axis the *Q5* frequency and the color scale is the normalized magnitude in a.u. of the readout resonator. The purple dots are the simulation plot for the state $|010\rangle$ (Q5) and in blue the state $|001\rangle$ (Coupler 56). Here the notation $|Q6, Q5, Coupler56\rangle$ is employed (see Appendix A.2 for details). In **b)** avoided level crossing for *Qubits* 6 and *Coupler 56*: on the x-axis the applied flux on *Coupler 56* in flux quanta, on the y-axis the *Q6* frequency and the color scale is the normalized magnitude in a.u. of the readout resonator. The green dots are the simulation plot for the state $|100\rangle$ (Q6) and in blue the state $|001\rangle$ (Coupler 56). In **c)** the plot of the state $|001\rangle$ (Coupler 56) on a larger flux range. We see that the coupler first crosses at higher frequency the Q5 and at lower frequency Q6. The color plots in panels **a)** and **b)** are also shown in the figure as a reference.

4.38b we observe the ALC occurring at $(0.350 \pm 0.001)$ flux quanta of the *Coupler 78* flux. The values of the strength interaction are $g_{1c} = (35 \pm 2)$ *MHz* for the *Q7-Coupler*, $g_{2r} = (28 \pm 2)$ *MHz* for the *Q8-Coupler*, and $g_{12} = (15 \pm 2)$ *MHz* for the *Q7-Q8*, where the error is the maximum error. The frequency of Q8 shows a clear dependence on the coupler flux, i.e. it tends to linearly decrease in the range 0.4-0.6 $\Phi/\Phi_0$. This suggests possible crosstalk between the flux lines of Q8 and TC78. This effect is not included in the simulation, which explains the deviation between experiments and the simulation in Fig. 4.38b.

Following the same experimental approach, we focus also on the pair Q5 and Q6. We perform the spectroscopy on *Q5* with a drive attenuation of 30 dBm while sweeping the flux on *Coupler* 56 and keeping the *Q5* at the upper sweet spot, and we observe the ALC occurring at $(0.340 \pm 0.001)$ flux quanta of the *Coupler 56* flux, see Fig. 4.39a. The values of

| | Pair 56 | | Pair 78 | |
|---|---|---|---|---|
| | ALC Q5-TC56 | ALC Q6-TC56 | ALC Q7-TC78 | ALC Q8-TC78 |
| $g_{1c}$ (MHz) | 38 | 38 | 42 | 35 |
| $g_{2c}$ (MHz) | 38 | 38 | 28 | 28 |
| $g_{12}$ (MHz) | 10 | 10 | 15 | 15 |

Table 4.40: Comparison table for the interaction strength values ($g_{1c}$ , $g_{2c}$ , $g_{12}$) obtained from the fit. For each pair, the table shows the values obtained from the individual measurements of Avoided Level Crossings (ALC) with the coupler. The error on the values is ± 0.2 MHz and is the maximum error.

the strength interaction are $g_{1c} = (38 \pm 2)MHz$ for the *Q6-Coupler*, $g_{2r} = (98 \pm 2)MHz$ for the *Q5-Coupler*, and $g_{12} = (10 \pm 2)MHz$ for the *Q5-Q6*, where the error is the maximum error.

The same investigation was conducted for *Q6* and is shown in Fig. 4.39b. We observe that the ALC occurrs at $(0.375 \pm 0.001)$ flux quanta of the *Coupler 56* flux. From the fit, the strength interaction are $g_{1c} = (38 \pm 2)MHz$ for the *Q6-Coupler*, $g_{2r} = (98 \pm 2)MHz$ for the *Q5-Coupler*, and $g_{12} = (10 \pm 2)MHz$ for the *Q5-Q6*, where the error is the maximum error. The obtained values are compiled in Table 4.40 for comparative purposes.

The measurements of ALC for Q7-TC78 and ALC for Q8-TC78 reveal a 20% discrepancy in the values of $g_{1c}$, corroborating previous observations made regarding flux crosstalk between Q8 and TC78. From the strength interaction values obtained from the fit, we can estimate the capacitances of the equivalent circuit, as described in Sec. 3.2 (see Fig. 3.4b). From Eqs. 3.5 and 3.6 we get:

$$C_{ic} = 2g_{ic}\sqrt{C_i C_c}\frac{1}{\sqrt{\omega_i \omega_c}}\,, \quad (i = 1, 2) \tag{4.3}$$

$$C_{12} = 2\sqrt{\frac{C_1 C_2}{\omega_1 \omega_2}}g_{12} - \frac{C_{1c}C_{2c}}{C_c}. \tag{4.4}$$

The values obtained are reported in Table 4.41a with an error of 0.2 fF given as propagation of the maximum errors. For the pair Q7-Q8, $g_{1c}$ is given by the average of the values in Table 4.40. The capacitance values extracted from the measurements are in remarkable agreement with the values commonly reported in literature [7], both being of the same order of magnitude.

From this result, we estimate the effective coupling strength $\widetilde{g}$ for both pair Q5 and Q6, and Q7 and Q8. In Fig. 4.41a is shown the behavior of $\widetilde{g}$ (see Sec. 3.2), for the pair Q5-Q6. We employ Eq. 3.10 using the capacitance values found from the fit, assuming Q5 on resonance with Q6. A modulation amplitude for the effective interaction of about 15 MHz results, together with an expected off-point value of $\omega_c^{off} = 5.15\ GHz$. The same analysis was performed for the pair Q7 Q8 using the capacitance values in Table 4.41a and, assuming Q8 on resonance on Q7, we obtain a modulation amplitude for the effective interaction about 25 MHz and the off-point value $\omega_c^{off} = 5.18\ GHz$.

The values obtained from the fit of the ALC measurements between qubits and couplers for both pairs are comparable and align with the order of magnitude found in existing

**a)**

| | $C_{1C}$ | $C_{2C}$ | $C_{12}$ | $C_1$ | $C_2$ | $C_C$ |
|---|---|---|---|---|---|---|
| ***Pair* 56** (fF) | 1.1 | 1.1 | 0.2 | 59.6 | 65.4 | 96.8 |
| ***Pair* 78** (fF) | 1.1 | 0.8 | 0.3 | 58.7 | 64.5 | 96.8 |

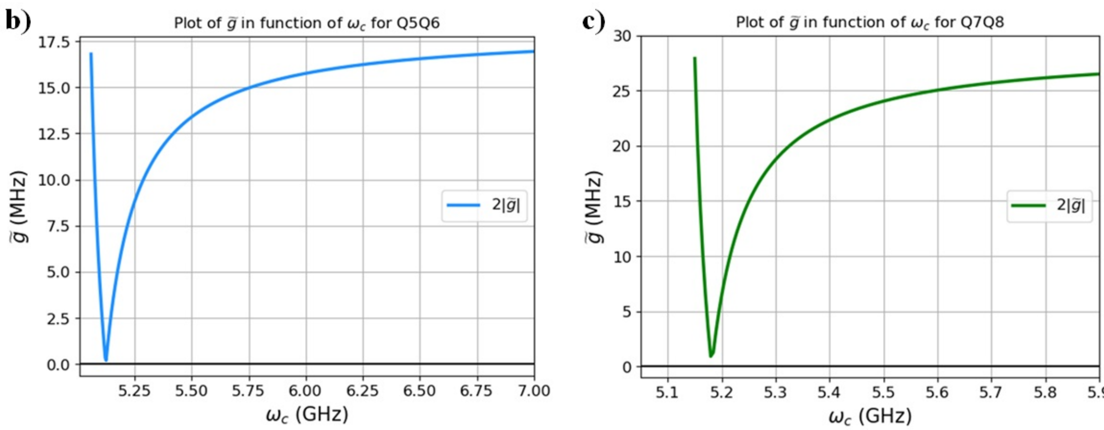


Figure 4.41: In **a)** comparison table for capacitance values. The capacitances of the individual qubits ($C_1$ , $C_2$ , $C_c$) were obtained from the charge energy, following the expression $E_C = e^2/2C$, where $e$ is the electron charge. The capacitances of the circuit ($C_{1c}, C_{2c}, C_{12}$) are obtained from the fit. The error on the values is ± 0.2 fF and is given by propagation from the maximum error. In panel **b)** simulation plot comparison of the effective interaction $\widetilde{g}$ from Eq. 3.10, with the capacitance values in **c)**, for the pair Q5-Q6 assuming Q5 on resonance with Q6 and for the pair Q7-Q8 assuming Q8 on resonance with Q7 (panel **c)**).

literature [9]. In particular, we have obtained for both the pairs that the condition of N.N.N. capacitive connection is weaker than the N.N. coupling, i.e. ($C_{12} \ll C_{1c}, C_{2c}$) [7] (Sec. 3.2).

The effective interaction strength values are comparable with those obtained from the literature (see Ref. [78][79]). However, the literature values for the detuning between $\omega_c^{off}$ and the qubit frequencies are around 1 GHz [7], which is an order of magnitude larger than the detuning estimated from the capacitance in Table 4.41a.

It is crucial to note that the spectroscopy measurements are affected by an intrinsic error. This is due to the necessary trade-off in the power of the drive signal: if it's too weak, the spectroscopic lines are typically poorly resolved, and if it's too strong, the spectroscopy peaks tend to broaden. This trade-off consequently increases the maximum error on the frequency estimation [69].

Simulating the expected behavior offers a clear advantage. Extracting information on the interaction terms of a three-qubit system and circuit values highlights the need to optimize this trade-off for more precise fit estimations. This optimization can be achieved by fine-tuning the input signal attenuation and enhancing the output amplification, even leveraging amplification stages at cryogenic temperatures. Additionally, for experimentalists, having a simulated expected trend during data acquisition serves as a beneficial guide, enhancing the measurement process.

### 4.4.3 Preliminary study of the off-point through ALC experiments

In order to observe the off-point, an ALC spectroscopy measurement was performed on Q7 and Q8 by varying the flux on the Coupler. Specifically, we perform a spectroscopy measurement on *Q7* with a drive attenuation of 35 dBm, while sweeping the flux on *Q8*, in order to set it on resonance with Q7. The measurement was repeated by varying the flux on the Coupler from 0.305 $\Phi/\Phi_0$ to 0.338 $\Phi/\Phi_0$. In this flux range, we performed fit simulation on ALC data for four flux points 0.306, 0.319, 0.329 and 0.334 ($\Phi/\Phi_0$), shown respectively in Fig.4.42a-b-c-d. We here observe that the ALC gap progressively reduces, finally closing at 0.320 flux quanta on the Coupler, where the bare state of Q7 is the only distinguishable peak (Fig. 4.43 b). By varying the flux on the Coupler, the gap finally reopens as shown in Fig. 4.42c. These measurements have been fitted, and the coupling strength values obtained are reported in Table 4.43.

From the results of the fit, obtained for the interaction strength values, we can estimate the behavior of the effective coupling strenght $\widetilde{g}$. Rewriting the Eq. 3.10 in terms of $g_{1c}$, $g_{2c}$ and $g_{12}$ we get:

$$\widetilde{g} \approx \frac{g_1 g_2}{2}\left(\frac{1}{\omega_1-\omega_c}+\frac{1}{\omega_2-\omega_c}-\frac{1}{\omega_1+\omega_c}-\frac{1}{\omega_2+\omega_c}\right)+g_{12}. \tag{4.5}$$

The behavior of $\widetilde{g}$ from the data fit is compared in Fig. 4.44a with the amplitude of the gap measured in the spectroscopy data of Fig.4.42, shown in Table 4.44b. This measure provides a rough but indicative estimate of the actual effective interaction between Q7 and Q8. From this comparison, we get an estimation of the off-point value around 5.8

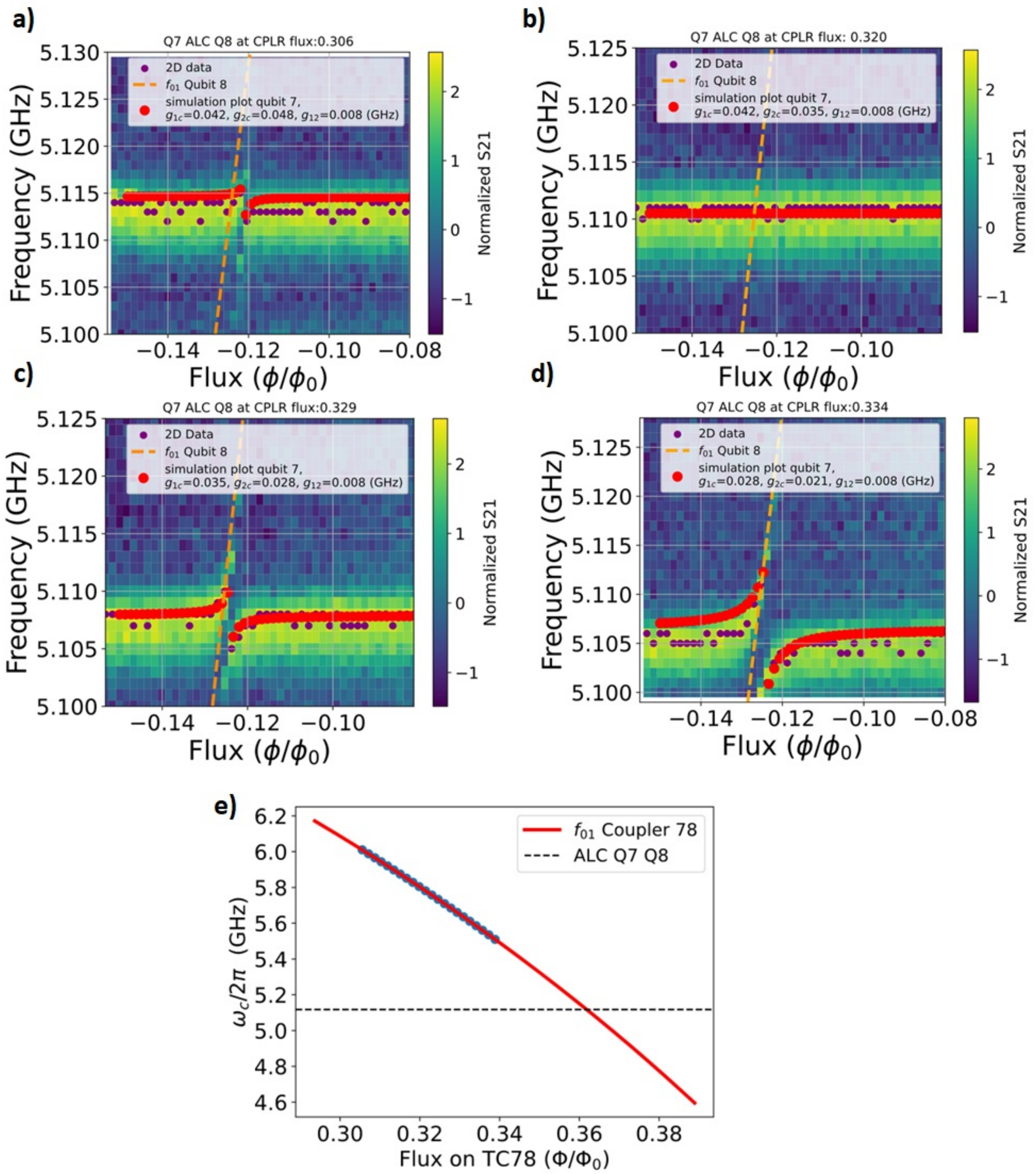


Figure 4.42: Spectroscopy on *Q7* with a drive attenuation of 35 dBm while sweeping the flux on *Q8*. The measurement was repeated by varying the flux on the Coupler from 0.305 $\Phi/\Phi_0$ to 0.338 $\Phi/\Phi_0$. On this range we performed fit simulation on ALC data for four points 0.306, 0.319, 0.329 and 0.334 ($\Phi/\Phi_0$), shown respectively in Fig.4.42**a**-**b**-**c**-**d**. In **e)** the $f_{01}$ of coupler 78 is plotted as a function of flux. The measurement points of the ALC (blue) are shown for comparison with the $f_{01}$ of Q7 at the ALC with Q8 (black line).

| Coupler 78 flux $(\pm 0.001\ \Phi_0)$ | 0.305 | 0.312 | 0.329 | 0.334 |
|---|---|---|---|---|
| Coupler 78 $f_{01}$ (± 2) MHz | 6.007 | 5.801 | 5.656 | 5.582 |
| $g_{1c}$ (± 5 MHz) | 0.041 | 0.035 | 0.035 | 0.028 |
| $g_{2c}$ (± 5 MHz) | 0.048 | 0.041 | 0.028 | 0.021 |
| $g_{12}$ (± 5 MHz) | 0.008 | 0.008 | 0.008 | 0.008 |

Table 4.43: Comparison table for coupling strength values obtained from the data fit. For each flux value applied on the Coupler 78 the $f_{01}$ frequency of the Coupler is shown together with the values of $g_{1c}$, $g_{2c}$ and $g_{12}$ obtained, where the errors are maximum errors.

**a)**

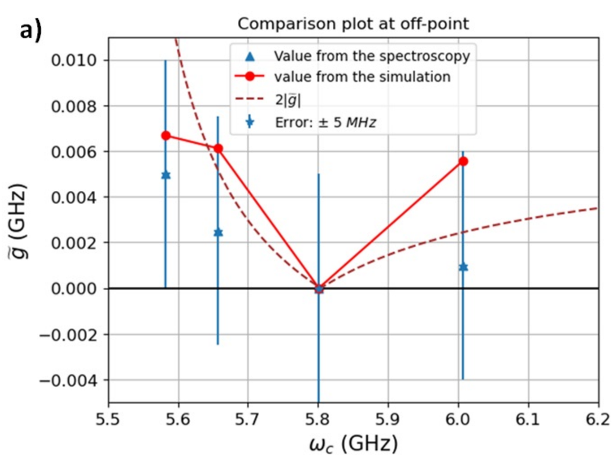


**b)**

| | $\tilde{g}$ *effective interaction* | |
|---|---|---|
| **Coupler $f_{01}$** (±0.002) GHz | Simulation (±0.005) GHz | Spectrosc. (±0.005) GHz |
| 6.007 | 0,005 | 0.001 |
| 5.801 | 0 | 0 |
| 5.656 | 0.006 | 0.003 |
| 5.581 | 0.007 | 0.005 |

Figure 4.44: In **a)** the effective interaction $\tilde{g}$ obtained for the frequency on the coupler 78 by the fit of the ALC measurements between Q7 and Q8. These values are compared with those obtained by direct measurement of the gap opening in spectroscopy measurements (blue dots). Error bars for the latter are of the order of 5 MHz. As a reference, the effective interaction strength $\tilde{g}$ is plotted (brown dashed line), obtained employing the Eq. 3.10 for $\omega_c^{off}$ at 5.8 GHz. In **b)** the comparison table shows the effective interaction values obtained from the data fit together with the amplitude of the gap measured in the spectroscopy data of Fig.4.42. For each value, the related frequency $f_{01}$ of the Coupler is shown. The errors are maximum errors.

GHz.

As already observed in the qubit-coupler direct ALC, this value is affected by an intrinsic error due to spectroscopy measurements. In addition, Q7 frequency at the ALC with Q8 negatively shifts as a function of the Coupler 78 frequency in Fig. 4.42. In particular, the maximum shift measured with respect to the Q7 unperturbed frequency is $(11 \pm 2)$ MHz at $(0.334 \pm 0.001)$ flux quanta on the Coupler 78. Among the possible motivations behind this effect, the variable detuning between Q7 and Q8 frequency related to flux crosstalk between the flux lines of Q8 and TC78 is the most reasonable. Therefore, the coupler frequency close to the off-point automatically approaches Q7 computational frequency. The similarity between the coupler off-point frequency and Q7 frequency suggests a design limitation for the Q7-Q8 pair [7].

Nevertheless, the effective interaction strength between two qubits in Fig. 4.42, reduces close to the off-point, and we can see a revival above the off-point, as expected. Here, we report a comparison between the effective coupling strength estimated from the ALC fitting around the off-point (red points), and the ones estimated from the ALC gap amplitude (blue points). The dashed brown line is a guide for the eye and represents the behavior of the effective interaction strength from the theory [7][79].

### 4.4.4 Study of the off-point through SWAP experiment

Typically, in order to measure the off-point in tunable coupling designs the most common procedure proposed is the measurement in time-domain, of the SWAP of energy between two qubits discussed in Sec. 3.3.2. This experiment has been performed on the pair Q5-Q6, reported in Fig. 4.45a.

In this experiment, we drive the Q5 with the calibrated $\pi - pulse$ and an attenuation of 21 dBm, in order to prepare the state $|10\rangle$. Simultaneously we read the energy swap through the demodulated imaginary signal of the Q6 readout resonator. The measurement was repeated by varying the amplitude of the flux on the Coupler from -375 mV to 0.375 mV, and its duration up to 300ns. The *Numerical Fourier transform* (FFT) is shown in Fig. 4.45b, where the frequency on the y-axis is a measure of the effective interaction strength, as shown in Ref. [89], see Fig. 4.45c.

The effective interaction strength as a function of the Coupler 56 flux amplitude decreases from $(36 \pm 1)$ MHz at $(-375 \pm 10)$ mV to $(6 \pm 1)$ MHz at $(-200 \pm 10)$ mV, where the errors are maximum errors. As a comparison, in Fig. 4.45$c$ and $d$ we show the SWAP results and the interaction strength obtained from the same experiment reported in Ref. [89]. The most important difference between the two datasets is the absence of a complete off-interaction condition.

#### Summary and concluding remarks

From the off-point measurements conducted on pairs 78 and 56, using two distinct experimental approaches, the effective qubit-qubit interaction depends on the coupler frequency, i.e. it reduces until a specific coupler frequency, and then increases again, aligning with the model described in Sec. 3.2. However, as noted in the SWAP experiment for the pair 56, the interaction at the off-point never reaches zero. Considering that the two pairs have been designed to be equivalent in terms of their electrodynamics parameters, we should expect that the same happens for the pair Q7-Q8 (see the summary of the electrodynamics parameters in Table 4.23 and the capacitances obtained from the fit of the ALC for the two pairs in Table 4.41a). Indeed, the off-point estimation for Q7-Q8 was based on ALC spectroscopy measurements as a function of the coupler frequency, modulated through flux-biasing across the dedicated flux-line. Typical spectroscopy measurements are affected by the half-width at half-maximum of the transition peaks, which is of the order of few MHz. It is reasonable to assume that such an error provides a limit for the off-point condition estimation [69].

Moreover, the crosstalk between the Q8 flux lines and TC78 and low frequency detuning between the coupler and the qubits, imposes constraints on the precision of the derived values. The design is indeed the primary bottleneck for these measurements, since the sample includes drive lines for 8 qubits, 4 flux lines and 10 readout resonators on the same chip. This inherently introduces crowding effects, which in turn cause crosstalk [34].

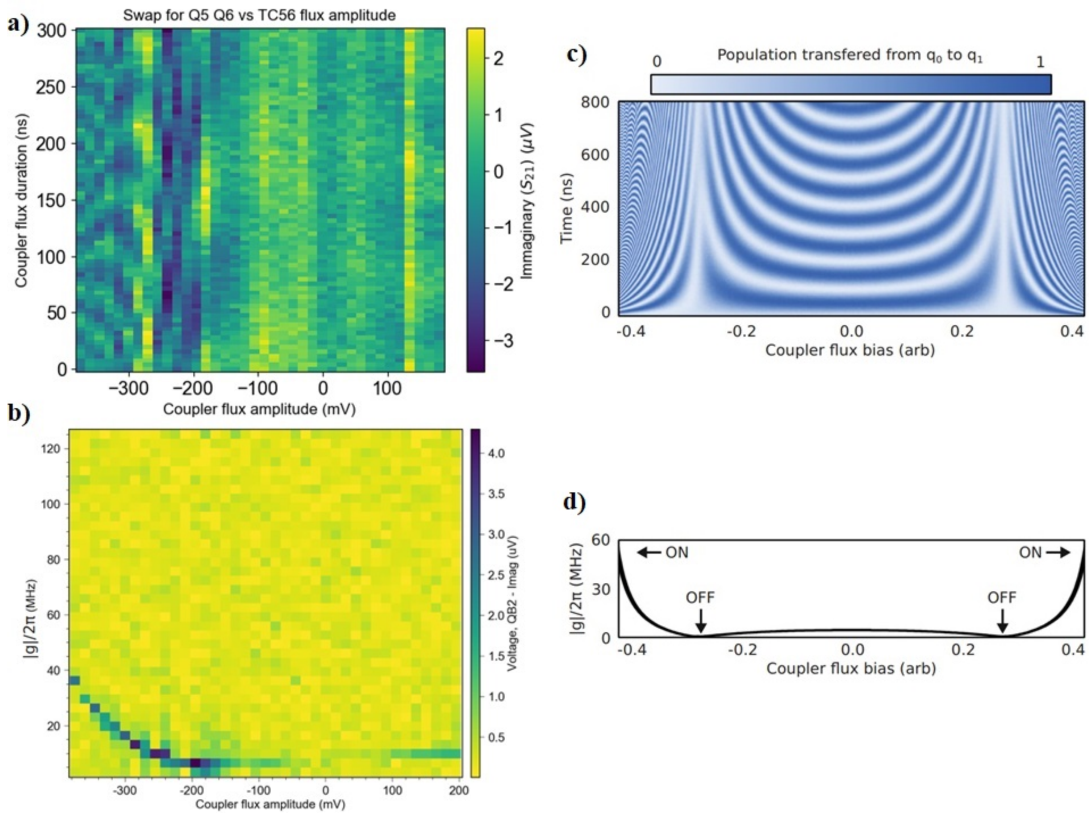


Figure 4.45: SWAP exchange of energy between Q5 and Q6: in **a)**, on the x-axis the amplitude flux applied on the Coupler 56 (in mV), on the y-axis the duration of the flux pulse and the color scale is the demodulated imaginary voltage of the readout resonators of Q6. The swap oscillation are faster in the region above -300 mV of Coupler flux amplitude, then up to 100 mV the swap rate decreases and remains constant. This behavior is more clearly observable in **b)** where the *Numerical Fourier transform* (FFT) is employed. The frequency on the y-axis is the value of the effective strength interaction [78], as defined in Sec. 3.3. In **c)** a demonstration of the tunable coupling between two qubits, adapted from [89], where the energy swap measurement between the two qubits is explored over the entire flux modulation of the coupler. In **d)** the effective interaction force modulation indicates the on-off ratio for the two-qubit swap operation. Figure adapted from [89].

# Conclusions

In this thesis, I have performed a detailed characterization of two different designs for superconducting qubit coupling, exploring their functionalities to comprehend advantages and disadvantages in the field of scalable quantum computing. Specifically, I worked on two samples characterized by two coupling schemes: one uses fixed coupling strength between two superconducting transmon qubits by means of a high-frequency bus resonator; the other uses a tunable coupling strength by means of a mediator flux-tunable qubit, or tunable coupler. This work is part of a collaboration between the two leading companies *Seeqc* and *Quantware*, and the *University of Naples Federico II*.

The characterization of individual qubits for each device began with the use of both continuous wave and time-domain protocols. These protocols estimated readout resonators and qubit frequencies, the charging energy of the qubits, and their relaxation and coherence times through Ramsey and Hahn-Echo protocols. By comparing the electrodynamics parameters of the devices with existing literature, the devices were validated in the context of isolated qubits. Yet, in the prototype design incorporating the coupler, experimental values for coherence and relaxation times were significantly influenced by an increased number of control and flux lines, and readout resonators, inducing spontaneous radiation emission, therefore enhancing the relaxation decay rate.

From this comparative analysis, it became evident that the prototype design stands as an ideal candidate for further research and development. I have particularly contributed to data analysis of the experimental avoided level crossings in the energy spectra occurring typically in coupled two-level systems, by implementing an innovative non-perturbative method to study the coupling forces, validated on the standard design with a fixed coupler, proving its efficacy and reliability.

The exploration of the prototypal tunable coupling design has thus proven the feasibility of the technique, allowing to extract pivotal information, such as the condition of next-nearest neighbors (N.N.N.) capacitive connection being weaker than the nearest neighbors (N.N.) coupling, i.e., $C_{12} \ll C_{1c}, C_{2c}$ [7]. Avoided level crossing experiments were conducted by modulating the coupler frequency through flux-tuning. This analysis technique was used to discern the dependence of the two-qubit interaction strength on the coupler frequency, in order to measure the so-known off-point, i.e. the coupler frequency at which the interaction between the two qubits effectively switches off. These findings were compared with a more standard time-domain technique in literature, i.e. the SWAP experiment. The results obtained from the off-point and SWAP tests show that the effective interaction strength at the off-point never reached zero. This can be ascribed to a lower detuning between the coupler and the qubits in the off-point condition, compared with the values reported in the literature [7][79]. This limitation serves as a catalyst for refining the design and the data analysis technique, a task that is inherently challenging, given the complexity of a system involving three coupled qubits.

In conclusion, through innovative analysis approaches, we have highlighted the potential and challenges of different qubit coupling designs. The insights and challenges encountered are stepping stones towards the realization of more robust and efficient quantum computing architectures, fostering optimism and determination for continual exploration and enhancement in the field.

# –A–
# Appendix

## A.1 Curve-fit for flux tunable cavity readout modulation

In order to use Eq. 2.5 to fit the experimental results of readout frequency modulation as a function of an external flux, we employ a *Non-Linear Least Squares* fit using *Python's SciPy* library [83]. The fit was performed using a composite function that incorporates several physical parameters. Specifically, from the Eq. 2.5, the fitting function $\omega_r(x)$ is defined as:

$$\omega_r(x, d, g, \omega_{01}^{ss}, E_c, \omega_r^{\mathrm{bare}}, \delta) = \omega_r^{\mathrm{bare}} + \frac{g^2}{\left| f_{01}(\omega_{01}^{ss}, E_c, d, x) - \omega_r^{\mathrm{bare}} \right|} + \delta, \tag{A.1}$$

where $f_{01}(\omega_{01}^{ss}, E_c, d, x)$ represents the qubit frequency as a function of the flux $x$, see 1.42 . Here $\omega_r^{\mathrm{bare}}$ is the *bare* cavity frequency, $g$ is the coupling strength, and $\delta$ is an additional correction, see Eq. 1.49. The function $f_{01}$ is further defined as:

$$f_{01}(\omega_{01}^{ss}, E_c, d, x) = \left(\omega_{01}^{ss} + E_c/\hbar\right) \sqrt{\left|\cos(x \cdot \pi)\sqrt{1 + d^2 \tan^2(x \cdot \pi)}\right|} - E_c/\hbar. \tag{A.2}$$

The fit requires physical initial parameters estimates and bounded constraints to ensure physical validity. We use the design values for $\omega_{01}^{ss}$ and $E_C$, which are then corrected once they become available from the following experiments.

To generate the theoretical curve for comparison with the experimental data we establish the linear correspondence between flux and voltage. Therefore, the relation between the voltage applied and the flux satisfies: $\Phi = \frac{LV}{R}$, where $L$ is the inductance of the DC-SQUID in the qubit. Using a specialized wrapper function, we establish a relationship between voltage and the flux, that enables us to normalize the *x_data* (in voltage) to the flux ($\phi/\phi_0$ ). The wrapper function is defined as follows:

```
def wrapper_function(V, d, gi, o_bare, correction, V_max, V_min):
    normalized_flux = -0.5 * (V - V_max) / (V_min - V_max)
    return o_r(x, d, gi, o_uss, Ec, o_bare, correction).
```

Here $V$ represents the voltage data points. The normalized flux $\phi/\phi_0 = x$ is then used in the main fitting function to model the observed behavior and extract the optimized parameters, including $V_{\text{max}}$ and $V_{\text{min}}$, with their corresponding standard errors.

## A.2 Python Code for Quantum Simulations

In this appendix, we provide a description of the Python code used to perform the quantum simulations presented in this thesis. The code is written in Python and uses the `scQubits` library [88] for defining quantum objects and performing simulations, and `qutip` [90] for quantum object manipulation and tensor calculations.

### A.2.1 Two-qubits coupled by resonator bus

In Sec. 3.1 we have seen that the system of two transmon qubits capacitively coupled to a resonator is described by Hamiltonian 3.1. Each term can be implemented using the `scqubits` library in Python. The tunable transmon qubit's Hamiltonian follows from Eq. 1.21 and is represented in the number basis:

$$H_0 = 4E_{\text{C}}(\hat{n} - n_g)^2 - \frac{E_{\text{J}}}{2}(|n\rangle\langle n+1| + \text{h.c.}),$$

where $E_{\text{J}}$ is the Josephson energy, $E_{\text{C}}$ is the charging energy, $\hat{n}$ is the number operator, and $n_g$ is the offset charge.

```
    qubitA = scq.TunableTransmon(
    EJmax=EJ,
    EC=EC,
    d=0,
    flux=0,
    ng=0.0,
    ncut=30,
    truncated_dim=3,
    id_str="tmon_tune"
).
```

The system is initialized with parameters ‘EJ‘ and ‘EC‘ that we can estimate from spectroscopy measurements, as described in Sec.2.6.1. To compute the energy spectrum of the Transmon qubit, the code employs sparse diagonalization techniques [88].

The term $\omega_r a_r^\dagger a_r$ in Eq. 3.1, describes the energy of the resonator. This is implemented using the ‘Oscillator‘ class in *scQubits*:

```
    resonator = scq.Oscillator(
    E_osc=\omega_r,
    truncated_dim=3
).
```

In order to simulate the interaction between two qubits and a resonator, the interaction is implemented using the `scq.HilbertSpace` class from the `scqubits` library. First we initialize the Hilbert space as follows:

```
hilbertspace = scq.HilbertSpace([tmon_tune, tmon, resonator]).
```

Here, `tmon_tune` represents the Transmon qubit that we aim to study under flux variations, while `tmon` denotes the reference Transmon qubit that will remain fixed, mirroring the typical experimental approach. In the operatorial formalism, the interaction term can be represented as:

$$H_{\text{int}} = g_{ir} \left( b_i^\dagger a_r + b_i a_r^\dagger \right),$$

where:

- $b_i^\dagger$ and $b_i$ are the creation and annihilation operators for the qubit, respectively.
- $a_r^\dagger$ and $a_r$ are the creation and annihilation operators for the resonator, respectively.
- $g_{ir}$ is the coupling strength between the qubit and the resonator.

We proceed to define the coupling strengths between the qubits and the resonator in the code:

```
    g1 = g1r  # coupling strength between qubit 1 and resonator
    g2 = g2r  # coupling strength between qubit 2 and resonator
```

The interaction between (`tmon_tune`) and Resonator reads as:

```
hilbertspace.add_interaction(
    g_strength=g1,
    op1=tmon_tune.n_operator,
    op2=resonator.creation_operator,
    add_hc=True,
    id_str="tmon_tune-resonator"
),
```

here `n_operator` represents the number operator for the qubit, and `creation_operator` represents the creation operator for the resonator. The `add_hc=True` parameter ensures that the Hermitian conjugate of the interaction is also added to the Hilbert space. Interaction between tmon and Resonator reads as:

```
hilbertspace.add_interaction(
    g_strength=g2,
    op1=tmon.n_operator,
    op2=resonator.creation_operator,
    add_hc=True,
    id_str="tmon-resonator"
).
```

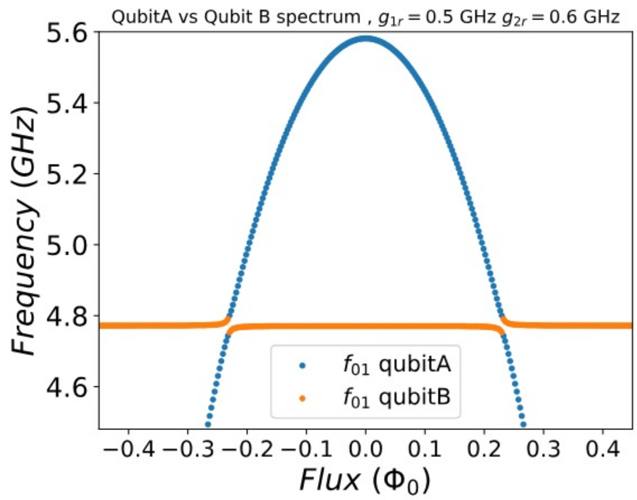


Figure A.1: $f_{01}$ spectrum in function of the flux applied on qubitA, for qubitA at 5.6 GHz and qubitB at 4.8 GHz, interacting via a high-frequency bus at 25 GHz. In the simulation, $g_{1r}$ is 0.5 GHz, and $g_{2r}$ is 0.6 GHz.

Similarly, g2 represents the coupling strength between `tmon` and the `resonator`.

This setup allows us to simulate the dynamics and study the properties of a system where two qubits, one tuned in flux and one kept fixed, interact with a resonator. The flexibility of the `scqubits` library enables the exploration of various parameters and configurations to gain insights into the behavior of such coupled qubit-resonator systems. In Fig. A.1 is shown an example of the simulation for: $f_{01}$ spectrum for qubitA at 5.6 GHz and qubitB at 4.8 GHz, in function of the flux applied on qubitA. The two qubits interact via a high-frequency bus at 25 GHz.

### A.2.2 Two qubits coupled by a third tunable qubit

In the Sec. 3.2 we have seen that the system of two transmon qubits capacitively coupled via a third qubit is described by the Hamiltonian 3.4. The interaction is implemented using the `scq.HilbertSpace` class similarly to the two qubits coupled by the resonator. We initialize the Hilbert space, including the two qubits and the coupler, as follows:

```
hilbertspace = scq.HilbertSpace([qubit1, qubit2, coupler])
```

In the Hamiltonian, the terms:

$$\sum_{j=1,2} g_j(\hat{b}_j^\dagger \hat{b}_c + \hat{b}_j \hat{b}_c^\dagger - \hat{b}_j^\dagger \hat{b}_c^\dagger - \hat{b}_j \hat{b}_c)$$

represent the interaction between qubit $j$ and the coupler qubit $c$, where $g_j$ is the coupling strength. Interaction between Qubit1 and Coupler reads as:

```
hilbertspace.add_interaction(
    g_strength=G1c,
```

```
    op1=qubit1.n_operator,
    op2=coupler.n_operator,
    add_hc=True,
    id_str="qubit1-coupler"
).
```

`G1c` represents the coupling strength between `qubit1` and the `coupler`, and `n_operator` represents the number operator for the respective qubit or coupler. The `add_hc=True` parameter ensures that the Hermitian conjugate of the interaction is also added to the Hilbert space. Interaction between Qubit2 and Coupler reads as:

```
hilbertspace.add_interaction(
    g_strength=G2c,
    op1=qubit2.n_operator,
    op2=coupler.n_operator,
    add_hc=True,
    id_str="qubit2-coupler"
),
```

similarly, `G2c` represents the coupling strength between `qubit2` and the `coupler`.

The term

$$g_{12}(\hat{b}_1^\dagger \hat{b}_2 + \hat{b}_1 \hat{b}_2^\dagger - \hat{b}_1 \hat{b}_2 - \hat{b}_1^\dagger \hat{b}_2^\dagger)$$

describes the direct interaction between the two main qubits, with $g_{12}$ being the coupling strength. This interaction is implemented in Python as:

```
hilbertspace.add_interaction(
    g_strength=G12,
    op1=qubit1.n_operator,
    op2=qubit2.n_operator,
    add_hc=True,
    id_str="qubit1-qubit2"
).
```

Where the *n_operator* represents the number operator for the respective qubit, and the '$add\_hc = True$' parameter ensures that the Hermitian conjugate of the interaction is also added, capturing both the creation and annihilation processes.

Through this implementation, we can simulate the dynamics of two qubits capacitively coupled via a third qubit, offering insights into the behavior of such systems and their potential applications in quantum computing.

In Fig. A.2 is shown an example of the simulation for: $f_{01}$ spectrum for qubitA at 5.1 GHz and qubitB at 4.0 GHz, and the Tunable Coupler at 8 GHz, as a function of the flux applied on the tunable coupler.

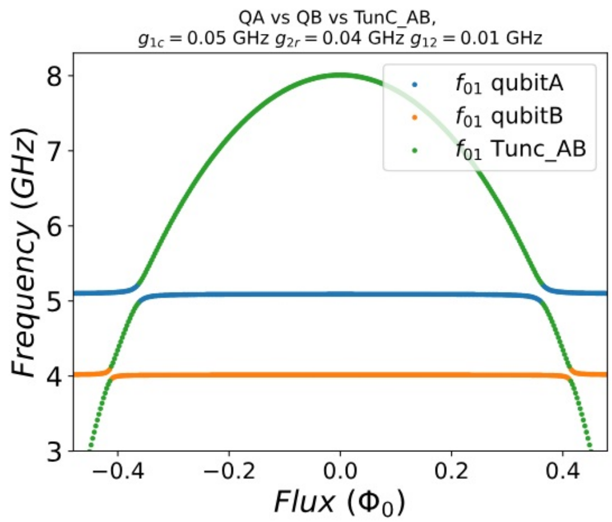


Figure A.2: $f_{01}$ spectrum for qubitA at 5.1GHz and qubitB at 4.0 GHz, and the Tunable Coupler at 8 GHz, in function of the flux applied on the tunable coupler. In the simulation, $g_{1c}$ is 0.05 GHz, $g_{2c}$ is 0.04 GHz and $g_{12}$ is 0.01 GHz.

# Bibliography


[1] Richard P. Feynman. “Simulating Physics with Computers”. In: *InternationalJournal of TheoreticalPhysics, VoL 21, 6/7, 1982* ().

[2] Y. Kim, A. Eddins, and S. Anand et al. “Evidence for the utility of quantum computing before fault tolerance”. In: *Nature 618, 500–505* (2023).

[3] Dmitry A. Fedorov, Matthew J. Otten, Stephen K. Gray, and Yuri Alexeev. “iAb initio/i molecular dynamics on quantum computers”. In: *The Journal of Chemical Physics* 154.16 (2021). DOI: `10.1063/5.0046930`. URL: `https://doi.org/10.1063%2F5.0046930`.

[4] Mahdi Naghiloo. *Introduction to Experimental Quantum Measurement with Superconducting Qubits*. 2019. arXiv: `1904.09291 [quant-ph]`.

[5] J. Verjauw et al. “Path toward manufacturable superconducting qubits with relaxation times exceeding 0.1 ms”. In: *npj Quantum Information* 8.1 (2022). DOI: `10.1038/s41534-022-00600-9`. URL: `https://doi.org/10.1038%2Fs41534-022-00600-9`.

[6] X. Li et al. “Tunable Coupler for Realizing a Controlled-Phase Gate with Dynamically Decoupled Regime in a Superconducting Circuit”. In: *Physical Review Applied* 14.2 (Aug. 2020). DOI: `10.1103/physrevapplied.14.024070`. URL: `https://doi.org/10.1103%2Fphysrevapplied.14.024070`.

[7] Fei Yan et al. “Tunable Coupling Scheme for Implementing High-Fidelity Two-Qubit Gates”. In: *Physical Review Applied* 10.5 (2018). DOI: `10.1103/physrevapplied.10.054062`. URL: `https://doi.org/10.1103%2Fphysrevapplied.10.054062`.

[8] Frank Arute et al. “Quantum supremacy using a programmable superconducting processor”. In: *Nature* 574.7779 (2019), pp. 505–510.

[9] Eyob A. Sete et al. “Floating Tunable Coupler for Scalable Quantum Computing Architectures”. In: *Physical Review Applied* 15.6 (2021). DOI: `10.1103/physrevapplied.15.064063`. URL: `https://doi.org/10.1103%2Fphysrevapplied.15.064063`.

[10] SEEQC. *Digital Quantum Computing | Chip Foundry & Fabrication*. URL: `https://seeqc.com/`.

[11] *QuantWare*. `https://www.quantware.eu/`.

[12] Università degli Studi di Napoli Federico II. URL: http://www.unina.it/en_GB/home.

[13] Anton Frisk Kockum and Franco Nori. "Quantum Bits with Josephson Junctions". In: *Fundamentals and Frontiers of the Josephson Effect.* Springer International Publishing, 2019, pp. 703–741. DOI: 10.1007/978-3-030-20726-7_17. URL: https://doi.org/10.1007%2F978-3-030-20726-7_17.

[14] Philip Krantz et al. "A Quantum Engineer's Guide to Superconducting Qubits". In: *Applied Physics Reviews 6, 021318* (2019).

[15] Michel Le Bellac. *A Short Introduction to Quantum Information and Quantum Computation.* Cambridge University Press, 2006.

[16] David P. DiVincenzo. "The Physical Implementation of Quantum Computation". In: *Fortschritte der Physik* 48.9-11 (2000), pp. 771–783. DOI: 10.1002/1521-3978(200009)48:9/11<771::aid-prop771>3.0.co;2-e. URL: https://doi.org/10.1002%2F1521-3978%28200009%2948%3A9%2F11%3C771%3A%3Aaid-prop771%3E3.0.co%3B2-e.

[17] M. Kjaergaard et al. "Superconducting qubits: Current state of play". In: *Annual Review of Condensed Matter Physics* 11 (2020), pp. 369–395.

[18] He-Liang Huang, Dachao Wu, Daojin Fan, and Xiaobo Zhu. "Superconducting Quantum Computing: A Review". In: *Science China Information Sciences* 63.8 (2020). DOI: 10.1007/s11432-020-2881-9.

[19] Y. Nakamura, Yu. A. Pashkin, and J. S. Tsai. "Coherent control of macroscopic quantum states in a single-Cooper-pair box". In: *Nature* 398.6730 (1999), pp. 786–788. DOI: 10.1038/19718. URL: https://doi.org/10.1038%2F19718.

[20] Y. Kim, A. Eddins, S. Anand, et al. "Evidence for the utility of quantum computing before fault tolerance". In: *Nature* 618 (2023), pp. 500–505. DOI: 10.1038/s41586-023-06096-3. URL: https://doi.org/10.1038/s41586-023-06096-3.

[21] H. K. Onnes. "The resistance of pure mercury at helium temperatures". In: *Commun. Phys. Lab. Univ. Leiden 12, p. 120* (1911).

[22] Dirk van Delft and Peter Kes. "The Discovery of Superconductivity". In: *Physics Today. 63 (9): 38–43.* (2010).

[23] W. Meissner and R. Ochsenfeld. "Ein neuer Effekt bei Eintritt der Supraleitfähigkeit". In: *Naturwissenschaften, Vol 21, p. 787, 1933* ().

[24] M. Tinkham. "Introduction to Superconductivity". In: *2nd ed. Dover Books,* (1996).

[25] Chenlu Wang et al. "Towards practical quantum computers: transmon qubit with a lifetime approaching 0.5 milliseconds". In: *npj Quantum Information* 8.1 (2022). DOI: 10.1038/s41534-021-00510-2. URL: https://doi.org/10.1038%2Fs41534-021-00510-2.

[26] William D. Oliver and Paul B. Welander. "Materials in superconducting quantum bits". In: *MRS Bulletin* 38.10 (2013). DOI: 10.1557/mrs.2013.229.

[27] J. Bardeen, L. N. Cooper, and J. R. Schrieffer. "Microscopic Theory of Superconductivity". In: *Physical Review 106, pp. 162–164* (1957).

[28] L. Frunzio et al. "Fabrication and Characterization of Superconducting Circuit QED Devices for Quantum Computation". In: *IEEE Transactions on Appiled Superconductivity* 15.2 (2005), pp. 860–863. DOI: `10.1109/tasc.2005.850084`. URL: `https://doi.org/10.1109%2Ftasc.2005.850084`.

[29] Antonio Barone and Gianfranco Paternò. "Physics and applications of Josephson effect". In: *Wiley-VCH* (1982).

[30] A. M. Zagoskin. "Quantum Engineering". In: *Cambridge University Press* (2011).

[31] L. P. Gor'kov. "Microscopic derivation of the Ginzburg Landau equations in the theory of Superconductivity". In: *Sov. Phys. JETP 36* (1959).

[32] T. Heikkilä. *The Physics of Nanoelectronics: Transport and Fluctuation Phenomena at Low Temperatures.* Oxford Master Series in Physics. Oxford University Press, 2013.

[33] B. D. Josephson. "Possible new effects in superconductive tunnelling". In: *Physics Letters 1 ,p.251* (1962).

[34] A. Blais, Arne L. Grimsmo, S. M. Girvin, and Andreas Wallraff. "Circuit Quantum Electrodynamics". In: *Rev. Mod. Phys. 93, 25005* (2021).

[35] M. H. Devoret. "Quantum fluctuations in electrical circuits". In: *Les Houches 72 Session LXIII, edited by S. Reynaud, E. Giacobino, and J. Zinn-Justin (Elsevier), pp. 351-386.* (1997).

[36] U. Vool and M. Devoret. "Introduction to quantum electromagnetic circuits". In: *International Journal of Circuit Theory and Applications, vol. 45, no. 7, pp. 897–934* (2017).

[37] Xiu Gu et al. "Microwave photonics with superconducting quantum circuits". In: *Physics Reports, Vol 718–719, 1–102, 2017* ().

[38] A. J. Leggett. "in Essays in theoretical physics. In honour of Dirk ter Haar." In: *W. E. Parry (Pergamon, Oxford), pp. 95-127* (1984).

[39] J Clarke et al. "Quantum mechanics of a macroscopic variable: the phase difference of a josephson junction". In: *SCIENCE, Vol 239, Issue 4843, pp. 992-997, DOI: 10.1126/science.239.4843.992* (1988).

[40] Jens Koch et al. "Charge-insensitive qubit design derived from the Cooper pair box". In: *Physical Review A* 76.4 (2007). DOI: `10.1103/physreva.76.042319`. URL: `https://doi.org/10.1103%2Fphysreva.76.042319`.

[41] J. A. Schreier et al. "Suppressing charge noise decoherence in superconducting charge qubits". In: *Physical Review B* 77.18 (2008). DOI: `10.1103/physrevb.77.180502`. URL: `https://doi.org/10.1103%2Fphysrevb.77.180502`.

[42] Editor: Francesco Tafuri. *Fundamentals and Frontiers of the Josephson Effect.* Springer Series in Materials Science (SSMATERIALS, volume 286), 2019.

[43] G. Wendin and V. S. Shumeiko. *Superconducting Quantum Circuits, Qubits and Computing*. 2005. arXiv: `cond-mat/0508729 [cond-mat.supr-con]`.

[44] Giulio Campanaro. "3D-integrated Modular Superconducting Circuits with Coaxial Qubits". Doctoral Dissertation. Somerville College: University of Oxford, 2022.

[45] G. Ithier et al. "Decoherence in a superconducting quantum bit circuit". In: *Physical Review B* 72.13 (2005). DOI: `10.1103/physrevb.72.134519`. URL: `https://doi.org/10.1103%2Fphysrevb.72.134519`.

[46] Daniel Thomas Sank. "Fast, Accurate State Measurement in Superconducting Qubits". Doctoral Dissertation. University of California, Santa Barbara, 2014.

[47] Lev S. Bishop. *Circuit Quantum Electrodynamics*. Preprint. 2010. arXiv: `1007.3520 [cond-mat.mes-hall]`. URL: `https://arxiv.org/abs/1007.3520`.

[48] David C. McKay et al. "Efficient $Z$ Gates for Quantum Computing". In: *Physical Review A* 96.2 (Aug. 2017). DOI: `10.1103/physreva.96.022330`. URL: `https://doi.org/10.1103%2Fphysreva.96.022330`.

[49] Erik Lucero et al. "Reduced phase error through optimized control of a superconducting qubit". In: *Physical Review A* 82.4 (2010). DOI: `10.1103/physreva.82.042339`. URL: `https://doi.org/10.1103%2Fphysreva.82.042339`.

[50] M. Orszag. *Quantum Optics*. Springer, 1999.

[51] Graham Batey and Gustav Teleberg. *Principles of Dilution Refrigeration*. Oxford Instruments NanoScience, 2023. URL: `https://nanoscience.oxinst.com/assets/uploads/NanoScience/Brochures/Principles%20of%20dilution%20refrigeration_Sept15.pdf`.

[52] Steven W. Van Sciver. *Helium Cryogenics (2nd edition)*. Springer, 2012. ISBN: 978-1-4419-9979-5.

[53] Low Noise Factory. *Datasheet for LNF-ISC4_8A and LNF-CIC4_8A*. URL: `https://lownoisefactory.com/wp-content/uploads/2022/03/lnf-isc4_8a-and-cic4_8a-1.pdf`.

[54] Morten Kjaergaard et al. "Superconducting Qubits: Current State of Play". In: *Annual Review of Condensed Matter Physics* 11.1 (2020), pp. 369–395. DOI: `10.1146/annurev-conmatphys-031119-050605`. URL: `https://doi.org/10.1146%2Fannurev-conmatphys-031119-050605`.

[55] Halima Giovanna Ahmad et al. "Investigating the Individual Performances of Coupled Superconducting Transmon Qubits". In: *Condensed Matter* 8.1 (2023). DOI: `10.3390/condmat8010029`.

[56] Jingjing Zhang. "Propagation Characteristics of Coplanar Waveguides at Subterahertz Frequencies". Doctoral Dissertation. University of Rochester, 2007.

[57] Rohde & Schwarz. *R&S®ZVL Vector Network Analyzer Specifications*. 2019. URL: https://scdn.rohde-schwarz.com/ur/pws/dl_downloads/dl_common_library/dl_brochures_and_datasheets/pdf_1/ZVL_dat-sw_en_5213-8150-22_v1200.pdf.

[58] Keysight. *Datasheet for M3202A PXIe Arbitrary Waveform Generator*. URL: https://www.keysight.com/us/en/assets/7018-05392/data-sheets/5992-1798.pdf.

[59] Signal Core. *Datasheet for 6 GHz Dual Channel Signal Generators (Signal Sources)*. URL: https://www.signalcore.com/6ghz_dual-channel_signal-source.html.

[60] Signal Core. *Datasheet for 20 GHz Signal Generators(Signal Sources)*. URL: https://www.signalcore.com/20ghz_signal-source.html.

[61] Keysight. *Datasheet for M3102A PXIe Digitizers*. URL: https://www.keysight.com/us/en/assets/7018-05399/data-sheets/5992-1805.pdf.

[62] *Labber User Manual*. URL: https://www.keysight.com/us/en/assets/9018-18184/user-manuals/9018-18184.pdf.

[63] Microsoft Corporation and Københavns Universitet. *QCoDeS Documentation*. 2023. URL: https://qcodes.github.io/Qcodes/index.html.

[64] Markus Jerger. "Experiments on Superconducting qubits coupled to Resonators". In: *Doctoral thesis, Karlsruher Institut für Technologie (KIT)* (2013).

[65] David Niepce. "Superinductance and Fluctuating Two-Level Systems: Loss and Noise in Disordered and Non-disordered Superconducting Quantum Devices". Doctoral Dissertation. Göteborg, Sweden: Chalmers University of Technology, 2020.

[66] Halima Giovanna. "Physics of the Josephson Effect in Junctions with Ferromagnetic Barriers towards Quantum Circuits and RF Applications". PhD thesis. Università di Napoli "Federico II", 2021.

[67] *QCoDeS Documentation*. https://qcodes.github.io/Qcodes/start/index.html.

[68] S. W. Jolin et al. "Calibration of mixer amplitude and phase imbalance in superconducting circuits". In: *Review of Scientific Instruments* 91.12 (2020), p. 124707. DOI: 10.1063/5.0025836.

[69] Yvonne Y. Gao, M. Adriaan Rol, Steven Touzard, and Chen Wang. "Practical Guide for Building Superconducting Quantum Devices". In: *PRX Quantum* 2.4 ().

[70] A. Bruno et al. "Reducing intrinsic loss in superconducting resonators by surface treatment and deep etching of silicon substrates". In: *Applied Physics Letters* 106.18 (2015). DOI: 10.1063/1.4919761. URL: https://doi.org/10.1063%2F1.4919761.

[71] D. I. Schuster et al. “Resolving photon number states in a superconducting circuit”. In: *Nature* 445 (2007), pp. 515–518.

[72] Grégoire Ithier. “Manipulation, Readout and Analysis of the Decoherence of a Superconducting Quantum Bit”. English. NNT: ff. fftel-00130589f. PhD Thesis. Université Pierre et Marie Curie - Paris VI, 2005.

[73] Frank K. Wilhelm John Clarke. “Tunable Josephson Junction Based Superconducting Qubits”. In: *Nature* 453 (2008). DOI: 10.1038/nature07128.

[74] John Preskill. “Quantum Computing in the NISQ era and beyond”. In: *Quantum* 2 (2018), p. 79. DOI: 10.22331/q-2018-08-06-79. URL: https://doi.org/10.22331%2Fq-2018-08-06-79.

[75] D. Rosenberg et al. “3D integrated superconducting qubits”. In: *npj Quantum Information* 3.1 (2017). DOI: 10.1038/s41534-017-0044-0. URL: https://doi.org/10.1038%2Fs41534-017-0044-0.

[76] S. Filipp et al. “Multimode mediated qubit-qubit coupling and dark-state symmetries in circuit quantum electrodynamics”. In: *Physical Review A* 83.6 (2011). DOI: 10.1103/physreva.83.063827. URL: https://doi.org/10.1103%2Fphysreva.83.063827.

[77] Yu Chen et al. “Qubit Architecture with High Coherence and Fast Tunable Coupling”. In: *Physical Review Letters* 113.22 (2014). DOI: 10.1103/physrevlett.113.220502. URL: https://doi.org/10.1103%2Fphysrevlett.113.220502.

[78] Youngkyu Sung et al. “Realization of High-Fidelity CZ and $ZZ$-Free iSWAP Gates with a Tunable Coupler”. In: *Physical Review X* 11.2 (2021). DOI: 10.1103/physrevx.11.021058. URL: https://doi.org/10.1103%2Fphysrevx.11.021058.

[79] Lukas Heunisch, Christopher Eichler, and Michael J. Hartmann. *Tunable coupler to fully decouple superconducting qubits.* 2023. arXiv: 2306.17007 [quant-ph].

[80] Amir H. Karamlou et al. “Analyzing the performance of variational quantum factoring on a superconducting quantum processor”. In: *npj Quantum Information* 7.1 (2021). DOI: 10.1038/s41534-021-00478-z. URL: https://doi.org/10.1038%2Fs41534-021-00478-z.

[81] Clemens Müller, Jared H Cole, and Jürgen Lisenfeld. “Towards understanding two-level-systems in amorphous solids: insights from quantum circuits”. In: *Reports on Progress in Physics* 82.12 (2019), p. 124501. DOI: 10.1088/1361-6633/ab3a7e. URL: https://doi.org/10.1088%2F1361-6633%2Fab3a7e.

[82] Firat Solgun and Srikanth Srinivasan. “Direct Calculation of $ZZ$ Interaction Rates in Multimode Circuit Quantum Electrodynamics”. In: *Physical Review Applied* 18.4 (2022). DOI: 10.1103/physrevapplied.18.044025. URL: https://doi.org/10.1103%2Fphysrevapplied.18.044025.

[83] SciPy Developers. *scipy.optimize.curve$_f$it*. 2022. URL: https://docs.scipy.org/doc/scipy/reference/generated/scipy.optimize.curve_fit.html.

[84] HaiJie Li et al. "Experimental demonstrations of high-Q superconducting coplanar waveguide resonators". In: *Chinese Science Bulletin* 58.20 (2013), pp. 2413–2417. DOI: 10.1007/s11434-013-5882-3. URL: https://doi.org/10.1007%2Fs11434-013-5882-3.

[85] M. H. Devoret and J. M. Martinis. "Implementing qubits with superconducting integrated circuits". In: *Quantum Information Processing 3, 163–203* (2004).

[86] J. M. Fink et al. "Climbing the Jaynes–Cummings ladder and observing its nonlinearity in a cavity QED system". In: *Nature* 454.7202 (2008), pp. 315–318. DOI: 10.1038/nature07112. URL: https://doi.org/10.1038%2Fnature07112.

[87] J. Majer et al. "Coupling superconducting qubits via a cavity bus". In: *Nature* 449.7161 (2007), pp. 443–447. DOI: 10.1038/nature06184. URL: https://doi.org/10.1038%2Fnature06184.

[88] Peter Groszkowski and Jens Koch. "Scqubits: a Python package for superconducting qubits". In: *Quantum 5, 583* (2021).

[89] B. Foxen et al. "Demonstrating a Continuous Set of Two-qubit Gates for Near-term Quantum Algorithms". In: *Physical Review Letters* 125.12 (2020). DOI: 10.1103/physrevlett.125.120504. URL: https://doi.org/10.1103%2Fphysrevlett.125.120504.

[90] P.D. Nation et al. "QuTiP: Quantum Toolbox in Python". Release 4.7.0., (2022).